

Научном већу Института за физику Београд

Београд, 5. јул 2013.

Предмет:

Молба за покретање поступка за стицање звања истраживач сарадник

С обзиром да испуњавам критеријуме прописане од стране Министарства просвете, науке и технолошког развоја за стицање звања истраживач сарадник, молим Научно веће Института за физику Београд да покрене поступак за мој избор у наведено звање.

У прилогу достављам:

1. Мишљење руководиоца пројекта
2. Кратку биографију
3. Списак објављених радова и њихове копије
4. Потврду о упису на докторске студије

Са поштовањем,

Никола Продановић

Научном већу Института за физику Београд

Београд, 5. јул 2013.

Предмет:

Мишљење руководиоца пројекта за избор Николе Продановића у звање истраживач сарадник

Колега Никола Продановић је тренутно студент завршне године докторских студија на Универзитету у Лидсу. Са њим је постигнут оквирни договор да се по завршетку израде тезе у октобру 2013. године запосли на Институту за физику и ангажује на пројекту основних истраживања Министарства за просвету, науку и технолошки развој ОН171017 под називом “Моделирање и нумеричке симулације сложених вишечестичних система”. С обзиром да испуњава критеријуме прописане од стране Министарства просвете, науке и технолошког развоја, сагласан сам са покретањем поступка за избор Николе Продановића у звање истраживач сарадник.

За састав Комисије за избор Николе Продановића у звање истраживач сарадник предлажем колеге:

- (1) др Ненад Вукмировић, виши научник сарадник, Институт за физику Београд,
- (2) др Антун Балаж, виши научник сарадник, Институт за физику Београд,
- (3) др Јелена Радовановић, ванредни професор Електротехничког факултета Универзитета у Београду.

Руководилац пројекта,

др Александар Белић,
научни саветник, Институт за физику Београд



Biografija Nikole Prodanovića

Nikola Prodanović rođen je u Postojni, R. Slovenija 28. 07. 1986. godine. Završio je OŠ „Dositej Obradović“ i Gimnaziju „Veljko Petrović“ u Somboru sa maksimalnim uspehom. Osvajao je mnogobrojne nagrade na takmičenjima iz prirodnih nauka i bio je učesnik Međunarodne olimpijade iz fizike 2005. godine u Španiji.

Završio je Elektrotehnički fakultet – Odsek za Fizičku elektroniku sa prosečnom ocenom 9.87 i diplomskim radom na temu „Fotonski kristali sa vezanim stanjem u kontinualnom delu spektra“ 2009. godine. Master studije je završio na istoj instituciji i odseku 2010. godine sa prosečnom ocenom 10.00 i završnim master radom na temu „Optimizacija AllnAs/InAs konvertora za silicijumske solarne ćelije na bazi kvantnih jama“. Od 1. 10. 2010. je student doktorskih studija na Elektronskom i elektrotehničkom fakultetu Univerziteta u Lidsu u Velikoj Britaniji sa očekivanim datumom završetka 1. 10. 2013. godine. Na doktorskim studijama se bavi teorijskim modelovanjem fizičkih procesa u kvantnim tačkama.

U toku školovanja je dobio mnogobrojne nagrade za akademski uspeh među kojima se posebno izdvaja stipendija Fonda za mlade talente Republike Srbije. Nikola je do sada objavio 5 radova u vodećim svetskim časopisima (kategorija M21) i autor je većeg broja konferencijskih radova.

Nikola Prodanović - Spisak radova i saopštenja sa konferencija

M21

1. N. Prodanovic, V. Milanovic, Z. Ikonic, D. Indjin and P. Harrison,
“Bound states in continuum: Quantum dots in a quantum well”
Physics Letters A, DOI: 10.1016/j.physleta.2013.05.051.
2. N. Prodanovic, Z. Ikonic, D. Indjin and P. Harrison,
“Relationship between electron-LO phonon and electron-light interaction in quantum dots”, Physical Review B 85, p. 195435 (2012).
3. N. Prodanovic, N. Vukmirovic, D. Indjin, Z. Ikonic, P. Harrison,
“Electronic states and intraband terahertz optical transitions in InGaAs quantum rods”,
Journal of Applied Physics 111, p. 073110 (2012).
4. N. Prodanovic, J. Radovanovic, V. Milanovic, S. Tomic,
“Optimization of InAs/AlInAs quantum wells based up-converter for silicon solar cells”,
Journal of Applied Physics 110, p. 063713 (2011).
5. N. Prodanovic, J. Radovanovic, V. Milanovic,
“Photonic crystals with bound states in continuum and their realization by an advanced
digital grading method”,
Journal of Physics A: Mathematical and Theoretical 42, p. 1 (2009).

M23

5. N. Prodanovic, J. Radovanovic, V. Milanovic,
“Engineering and advanced digitalization of photonic structures with bound field in the
continuum”,
Acta Physica Polonica A, 116, p. 607, preceded by poster presentation on “Photonica 09”
Conference, Belgrade (Serbia), 2009.

M34

6. N. Prodanovic, Z. Ikonic, D. Indjin, P. Harrison,
“Tailoring of Intraband Luminescence and Lifetime properties of Quantum Dots”,
The 7th International Conference on Quantum Dots, 13-18 May 2012, Santa Fe, USA,
Book of abstracts, p. 118 (2012).
7. N. Prodanovic, N. Vukmirovic, D. Indjin, Z. Ikonic and P. Harrison,
“Intraband optical properties of self-assembled InGaAs quantum rods and its dependence
on rod height”,
The 11th International Conference on Intersubband Transitions in Quantum Wells, 11-17
September 2011, Badesi, Italy, Book of abstracts (2011).

8. N. Prodanovic, J. Radovanovic, V. Milanovic, S. Tomic,
“Optimization of InAs/AlInAs quantum wells based up-converter for silicon solar cells”,
“Empirical Methods in Semiconductor Nano-Structures Design and Modelling” CECAM
Conference, Manchester (UK), Book of Abstracts, p. 24 (2010).

9. N. Prodanovic, N. Vukmirovic, D. Indjin, Z. Ikonc, P. Harrison,
“Intraband optical properties of self-assembled columnar quantum dots”, “QD2010”
Quantum dot Conference, Nottingham (UK), (2010).

10. N. Prodanovic, J. Radovanovic, V. Milanovic, D. Indjin, Z. Ikonc and P. Harrison,
„Enhanced digitalization technique for photonic structures generated to support a
localized field in the continuous part of the spectrum”,
UK Semiconductor Conference 2009, 1-2 July 2009, Sheffield, United Kingdom, Book
of Abstracts A-P-10, (2009).

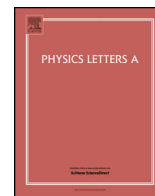
M53

11. N. Prodanovic, Z. Ikonc, D. Indjin, P. Harrison,
“Electron-LO Phonon and Electron-Photon Interactions analogy in Semiconductor
Quantum Dots”,
Journal of Physics: Conference Series, 367, p. 012008, 2012, preceded by poster
presentation on “TMCS III” Conference, Leeds (UK), (2012).

12. N. Prodanovic, N. Vukmirovic, D. Indjin, Z. Ikonc, P. Harrison,
“Theoretical modeling of InGaAs quantum rods: terahertz intraband absorption and its
dependence on rod height”,
Journal of Physics: Conference Series, 242, p. 2012, 2010, preceded by poster
presentation on “TMCS II” Conference, York (UK), (2010).

Contents lists available at SciVerse ScienceDirect

Physics Letters A

www.elsevier.com/locate/pla

Bound states in continuum: Quantum dots in a quantum well

Nikola Prodanović^{a,*}, Vitomir Milanović^b, Zoran Ikonić^a, Dragan Indjin^a, Paul Harrison^a^a Institute of Microwaves and Photonics, School of Electronic and Electrical Engineering, University of Leeds, Woodhouse Lane, Leeds LS2 9JT, UK^b School of Electrical Engineering, University of Belgrade, Bulevar Kralja Aleksandra 73, 11000 Belgrade, Serbia

ARTICLE INFO

Article history:

Received 8 March 2013

Received in revised form 19 May 2013

Accepted 24 May 2013

Available online xxxx

Communicated by R. Wu

Keywords:

Bound state in continuum

Quantum dot

Quantum well

ABSTRACT

We report on the existence of a bound state in the continuum (BIC) of quantum rods (QR). QRs are novel elongated InGaAs quantum dot nanostructures embedded in the shallower InGaAs quantum well. BIC appears as an excited confined dot state and energetically above the bottom of a well subband continuum. We prove that high height-to-diameter QR aspect ratio and the presence of a quantum well are indispensable conditions for accommodating the BIC. QRs are unique semiconductor nanostructures, exhibiting this mathematical curiosity predicted 83 years ago by Wigner and von Neumann.

© 2013 Elsevier B.V. All rights reserved.

1. Introduction

Semiconductor quantum dots exhibit full 3D confinement for carriers, giving a few bound integrable states with a discrete spectrum below the barrier, and free non-integrable states with continuum spectrum above the barrier. Quantum dots are often referred to as “artificial atoms” due to their discrete part of spectrum and discrete optical resonances arising from transitions between bound orbital states. Both atoms and quantum dots can be ionized, when electrons gain sufficient energy to escape the binding potential, and subsequently occupy free states – in vacuum in the case of atoms or bulk in the case of quantum dots.

However, boundedness and discreteness of an orbital state in quantum dots do not come necessarily together. We show in this Letter that novel semiconductor nanostructures, so called quantum rods, exhibit bound excited state with an energy embedded in the continuum of other free electronic states, above the ionization threshold. This is a so called bound state in continuum (BIC). There are various types of BIC reported since the foundation of quantum mechanics, but none of them were reported for atomic or condensed matter systems. In what follows, we state only a few. The first prediction originates back to 1929 when von Neumann and Wigner showed such a possibility by mathematical construction of a bounded potential accommodating a BIC [1]. This issue was revitalized by Stillinger and Herick [2] pointing out, 46 years later, that a BIC could occur in some specific molecular systems. The first artificial semiconductor nanostructure accommodating the bound state above ionization threshold, was reported in Ref. [3]. This

bound state was argued to be a consequence of Bragg reflection due to the superlattice. Even though above the barrier, this state wasn't surrounded by a continuum of states and it was strictly speaking a quasi-bound state with free motion in the lateral direction. Some theoretical proposals and proofs for the BIC existence were reported for more complex quantum mechanical systems. For example, coupled system of electrons and nuclei in molecules [4] was considered. BIC, as an quantum mechanical interference effect can occur in various abstract models. Some examples of theoretical abstract systems that support BIC were reported in Refs. [5–10]. Experimentally, only photonic crystal systems with the BIC were reported [11,12]. A theoretical design of one-dimensional photonic heterostructure, supporting the BIC was provided in Ref. [13].

In what follows, we briefly describe the geometrical and compositional properties of quantum rods, and based on that we provide proof for BIC existence. The type of BIC which occurs in quantum rods is somewhat different from the majority of BICs reported in the literature. The most similar system supporting the BIC was reported by Robnik et al. [14], and one could say that the BIC reported here represents the 3D generalization of the 2D potential theoretically constructed in [14]. The rest of the Letter is dedicated to the discussion of possible interesting features arising from BIC existence, together with available experimental data and concluding remarks.

2. Quantum rods

Quantum rods are elongated InGaAs quantum dots embedded in a InGaAs quantum well sandwiched by two GaAs bulk regions. Details of the QR fabrication can be found in Refs. [15–17]. A simplified model for geometric and compositional properties of these

* Corresponding author. Tel.: +44 7587029902.

E-mail address: elnpr@leeds.ac.uk (N. Prodanović).

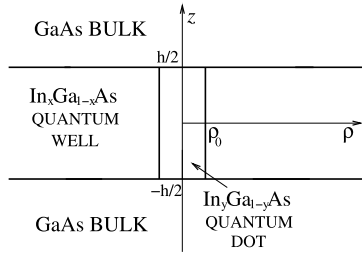


Fig. 1. Simplified geometric model of a quantum rod. Cylindrical symmetry is assumed, so the entire structure can be depicted within the z - ρ plane. Indium content of the dot region is larger than in the well region, i.e. $x < y$.

nanostructures is presented in Fig. 1. This structure consists of GaAs/InGaAs quantum well of width h over the region between $-h/2$ and $h/2$. The quantum dot is positioned within the quantum well so that the bulk region is above and below the dot in the z -direction and the quantum well is surrounding the rod in the radial direction. The entire structure is optically active giving the combined features of dot, well and the bulk as it is obvious from PL measurements [16,18]. The height of the rod and the width of the surrounding well are the same. This simplified model assumes that entire structure is cylindrically symmetric, even though such strict symmetry hasn't been reported. However, the general conclusions that follow do not depend on the exact shape of the rod basis. Therefore, we choose the circular shape of the basis in order to simplify theoretical consideration. The quantum rod has higher In content than the surrounding quantum well which makes the dot energetically deeper than the surrounding well.

3. Bound state in the continuum

One can naively expect that the quantum rod would accommodate bound states only below the quantum well barrier in the radial direction. However, due to bulk confinement in the z -direction, bound states could also appear with energies above the well barrier where also well continuum states are present giving the BIC. Such a situation resembles the one from Ref. [3] where a bound state occurs above the barrier of a superlattice, but it isn't surrounded by continuum states because the state itself is an impurity state in the superlattice, spaced from the continuum superlattice bands. Also, such a BIC is strictly speaking a quasi-bound state. We prove that in the case of a quantum rod, such state above the barrier is indeed surrounded by the continuum and is indeed bound for a wide range of parameter space.

Existence of the BIC in quantum rods is purely due to the interplay of the combined well and dot confinement. In order to prove this statement, consider the idealized quantum rod structure presented in Fig. 1. The quantum rod is considered isolated from the other quantum rods. We assume cylindrical symmetry of the entire structure, and the value of the embedding bulk barrier is set to infinity. The assumption of infinitely high bulk walls does not affect the general conclusion since the same conclusion follows from the full 8-band $\mathbf{k} \cdot \mathbf{p}$ model where the values for all barriers in the structure were taken with precise offsets and included strain effects. Now it becomes clear that this simplified model of realistic quantum rods presents the 3D generalization of the 2D potential constructed by Robnik et al. [14] in order to obtain the BIC, with the quantum well as escaping channel. However, it was pointed out in the same reference that existence of BIC in such potential is sensitive to perturbation, especially the one which might break the parallel geometrical shape of escaping channel. That shouldn't be a problem in this case, since the existence of quality quantum well seems very eminent, and the walls of quantum well escaping channel can be considered parallel to the infinity.

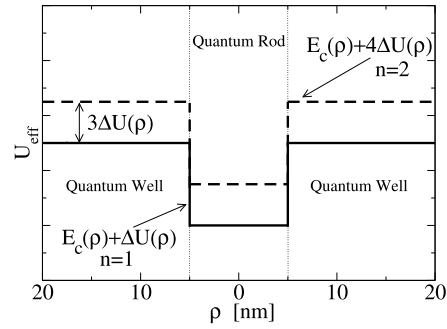


Fig. 2. Illustration of the energy span where a BIC can occur. The effective potential U_{eff} for the remaining one-dimensional radial eigenproblem is given for $l = 0$ and $n = 1, 2$. For $n = 1$ continuum states or quasi-bound well states occur for $E > U_b + \Delta U$. For $n = 2$ bound states might occur for $E < U_b + 4\Delta U$, whereas continuum states occur for $E > U_b + 4\Delta U$. Therefore the excited bound state in the well quasi-band continuum might occur for energies in the range $U_b + \hbar^2 \pi^2 / 2m_w \hbar^2 < E < U_b + 2\hbar^2 \pi^2 / m_w \hbar^2$.

In this simple model we solve one spinless electron single-band envelope function equation in polar coordinates:

$$\left(\frac{\hbar^2}{2} \nabla \frac{1}{m_e(\mathbf{r})} \nabla + E_c(\rho) + E_c^z(z) \right) \Psi(\mathbf{r}) = E \Psi(\mathbf{r}) \tag{1}$$

where

$$E_c(\rho) = \begin{cases} 0 & \text{for } \rho < \rho_0 \\ U_b & \text{for } \rho > \rho_0 \end{cases}$$

and

$$E_c^z(z) = \begin{cases} 0 & \text{for } -\frac{h}{2} < z < \frac{h}{2} \\ \infty & \text{for } z < -\frac{h}{2} \text{ or } z > \frac{h}{2} \end{cases}$$

Values of the effective mass $m_e(\mathbf{r})$ are m_d and m_w in the dot and the well respectively. In the bulk, where the value of the potential is set to infinity, the value of the effective mass is unnecessary. The potential offset between dot and the well region is U_b . Parameters ρ_0 and h are the radius and the height of the QR. Due to infinite bulk barrier and cylindrical symmetry, one can separate the variables of the wavefunction $\Psi(\mathbf{r}) = \Phi(\phi)Z(z)R(\rho)$. Furthermore, the solutions for $\Phi(\phi)$ and $Z(z)$ are $\Phi_l(\phi) = \frac{1}{\sqrt{2\pi}} e^{il\phi}$ and $Z_n(z) = \sqrt{\frac{2}{h}} \sin\left(\frac{n\pi}{h}\left(z + \frac{h}{2}\right)\right)$ where we introduce good quantum numbers l and n , integer and positive integers respectively. The remaining Schrödinger-like equation in the radial direction reads:

$$-\frac{\hbar^2}{2} \frac{1}{\rho} \frac{d}{d\rho} \frac{\rho}{m_e(\rho)} \frac{d}{d\rho} R_{nl}(\rho) + \left(E_c(\rho) - E + \frac{\hbar^2}{2m_e(\rho)} \left(\frac{n^2 \pi^2}{h^2} + \frac{l^2}{\rho^2} \right) \right) R_{nl}(\rho) = 0 \tag{2}$$

We provide the full solution to Eq. (2) in Appendix A. In order to maintain the simplicity, we will demonstrate the existence of the BIC by considering only the case with $l = 0$ and $n = 1, 2$.

The effective potential for the last eigenproblem in Eq. 2 is the expression given in brackets. The effective potential for $n = 1$ is $U_{\text{eff}}(\rho) = E_c(\rho) + \Delta U(\rho)$, where $\Delta U(\rho) = \hbar^2 \pi^2 / 2m_e(\rho) \hbar^2$ and for $n = 2$ it is $U_{\text{eff}}(\rho) = E_c(\rho) + 4\Delta U(\rho)$. The effective potential for $l = 0$ and $n = 1, 2$ is given in Fig. 2. Note that the effective mass depends only on the radial coordinate since the value of the effective mass in bulk is irrelevant due to infinite potential.

For $n = 1$ continuum states or quasi-bound well states occur for $E > U_b + \hbar^2 \pi^2 / 2m_w \hbar^2$. For $n = 2$ bound states might occur for $E < U_b + \hbar^2 2\pi^2 / m_w \hbar^2$, whereas continuum states occur for $E > U_b + 2\hbar^2 \pi^2 / m_w \hbar^2$. Therefore, the excited bound state for $n = 2$

in the well quasi-band continuum for $n = 1$ (above the ionization threshold) might occur at an energy between $U_b + \hbar^2\pi^2/2m_w h^2 < E < U_b + 2\hbar^2\pi^2/m_w h^2$. Note that the first bound states for $l = 0, n = 1, 2$ are so called s-like and p-like states as often referred to in literature. We give the numerical example of this p-like BIC in the next section.

4. Numerical results

In our previous work [19] we have calculated detailed electronic structure of the realistic quantum rods grown in [16] by using the 8-band $\mathbf{k} \cdot \mathbf{p}$ method with strain effects included. In this Letter we will use one-band model derived in previous chapter in order to demonstrate the existence of BIC and 8-band results will be used as a supporting reference.

For the fabricated rods reported in Ref. [16], the In content in the dot and the well is typically 0.45 and 0.16, respectively, and their radius was estimated to be around 5 nm. For such a structure we have extracted the value of dot-well band offset $U_b = 120$ meV, using the full 8 band $\mathbf{k} \cdot \mathbf{p}$ model with strain effects included [19]. The height of the rods from Ref. [16] is in the range 10–40 nm.

In the following, all energies are referenced to the bottom of the conduction band of the rod material. For the typical rod height of 10 nm, the continuum for $n = 1$ starts at 182 meV, and the p-like bound state for $n = 2$ is below the $n = 2$ continuum, starting at 356 meV. The splitting between s-like ground state and p-like first excited state (which is the BIC) is 200 meV. For the same rod, but with 15 nm height, we find 2 additional bound states, for $l = 0$ and $n = 3$ and 4, which are also embedded in the continuum. There are no discrete states solutions for $l > 0$. By increasing the rod height we generally get more bound states in the continuum, since new bound states with higher values of n appear. However, the energy of all bound states gets lower with increasing the quantum rod height [19], and consequently bound states with the lowest n might sink under the $n = 1$ continuum, ceasing to be BIC. Also, by increasing the rod radius, additional states may appear with higher value of quantum number l . These states may also become BIC.

Energy diagram of a 10 nm tall rod calculated by 8-band model is presented in Ref. [19]. Energy diagram clearly show the existence of the BIC. The higher the rod, the higher is the excited dot state embedded in continuum. For the 10 nm tall rod, the splitting between ground state and the bound state in the continuum is 150 meV. Higher value of s–p splitting is due to infinite potential barrier in growth direction which was realistically taken to be finite in 8-band model. In this work we used one-band model with infinite barriers as a default model in order to get insight in physics arguments of the BIC existence.

Therefore, we proved the existence of the bound state in continuum as a sole consequence of combined well-dot confinement, and for a wide range of structure parameters, especially the adjustable rod height.

5. Discussion

The above consideration shows that BIC occurs for higher values of the quantum number n , i.e. BIC has at least one node in the growth direction. The quantum rod must be sufficiently tall in order to support at least two bound states (s-like and p-like) localized in the dot due to the growth confinement, i.e. with quantum number $n > 0$. With increasing quantum number n , the effective potential $U_{\text{eff}}(\rho) = E_c(\rho) + \Delta U(\rho)$ might become a barrier instead of a well, since $m_d < m_w$. Therefore, the upper bound on a value of n for which BIC exists is imposed $n < \frac{\hbar}{\pi} \sqrt{\frac{U_b}{\hbar^2} \frac{m_w m_d}{m_w - m_d}}$ where m_w and m_d are effective masses of the well and the dot respectively.

We also conclude that confinement in the growth direction has to be stronger than the confinement in the radial direction caused by the shallower well. At the same time, well subbands may have energies lower than the bulk barrier, opening the possibility that their energy equals the energy of the excited bound state of the dot.

In similar nanostructures, quantum dots in a quantum well (DWELL), this effect does not exist. Conventional quantum dots have very low height to diameter aspect ratio and an excited bound state is guided by the radial confinement, i.e. the excited bound states have nodes in the radial direction and there is no bound state with nodes in the growth direction. Therefore, energy of such an excited state cannot be higher than the well barrier in the radial direction. One thus concludes that quantum rods are unique semiconductor nanostructures with 3D bound state in continuum as a consequence of their distinct features: high value of height-to-diameter aspect ratio and existence of the shallower surrounding well.

We have previously shown in Ref. [19] that only the growth-polarized light can excite an electron from the ground dot state in the conduction band to the first excited dot state which can be set to be BIC for particular heights of the rod. This is so called s–p-like optical transition. Such a transition is expected to be a single broadened line. We argue that homogeneous broadening is expected to be high due to effective interference of the continuum with the bound state via phonons. We also argue that asymmetrical lineshape of such optical resonance should be expected, also a consequence of interference of the continuum and p-like bound state along the resonant s–p transition. However, we do not expect that asymmetrical lineshape is observable due to high broadening and other resonances.

Intraband resonances of quantum rods were investigated in Ref. [17], where the rods were charged with several electrons, enough to completely fill the 3D confined states below the well barrier. Authors then used growth-polarized radiation to excite electrons, and they recognized a clear difference between well and dot resonances. The leading rod resonance comes from transition from excited and fully charged rod states to unoccupied states higher in the conduction band. However, authors in Ref. [17] argued that electron–electron interaction in fully charged rods shifts the bound electronic states to higher energies. Detailed theoretical examination of that situation is required due to electron–electron interaction which is responsible for perforation of the 2D electron gas, i.e. continuum. Nevertheless, the short lifetime of the BIC via fast scattering into the well subband was indicated in Ref. [17]. It is intuitively clear that such fast scattering occurs due to the availability of the continuum of free states around the energy of the BIC.

Altogether, one can conclude that carriers from the bound quantum rod state can be efficiently scattered into the continuum of the well by strong optical resonance due to ground state-BIC transition and coupling between the BIC and surrounding continuum. The similar effect, where strong optical resonance can trigger ionization from bound-like state to continuum state where carriers can freely move was explained in Ref. [20] for the case of 1D supercrystal formed of the vertically stacked self-assembled quantum dots. Specifically, first supercrystal miniband occurs in the barrier gap and second one in the conduction band. Optical transitions between these two minibands are strong since those minibands were formed of s-like and p-like states respectively. Therefore, this structure, if constructed as solar cell, exhibits increased efficiency due to strong transitions between first miniband buried in the barrier gap and second miniband buried within the conduction band continuum. In addition, strong optical transitions between below-the-barrier and above-the-barrier bound states were observed experimentally in Ref. [3] in a Bragg-confined quantum well structure.

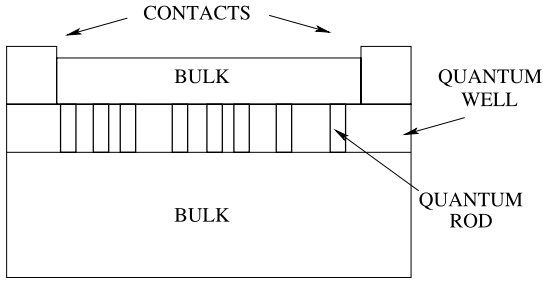


Fig. 3. Illustration of the polarization-independent terahertz photodetector. In this geometry, the electric field due to the bias on contacts is in the lateral direction.

These exotic optical properties of the BIC could allow experimental observation of the BIC and associated effects. The simplest version of such an experiment is based on doped structures with up to one electron per rod. In such a case, intraband optical transitions at low temperatures are limited to the transitions from the ground state. One could measure the absorption of far-infrared light in such doped quantum rods at low temperatures for two linearly polarized directions of incident light. We have also shown in Ref. [19] that radially polarized light can excite the electron from the same ground dot state to the first well subband. This transition is not expected to be a single broadened line due to the continuum of the well subband, but resonances are expected to start at an energy corresponding to the bottom of the first subband of the well. If these resonances for the radially polarized radiation were at lower energy than the first resonance for the growth-polarized radiation, this would present a clear evidence that the excited bound state has a higher energy than the minimum of the well subband, proving the existence of BIC.

Finally, we will briefly discuss a possible application of this effect. If an electron, excited into the BIC, efficiently scatters into the well subband, as indicated in Ref. [17], then a radially directed electric field can be used for efficient transport of carriers in the lateral direction. Strong optical resonance for the growth-polarized radiation is due to bound-to-bound transition and efficient transport can occur via radially free state channels around the excited bound state. On the other hand, for radially polarized incident radiation, carriers are excited directly into the well subband [19], from which they can be easily extracted by a lateral electric field. Therefore, strong resonance and efficient transport can be obtained for either polarization of the incident light, paving the way for polarization-independent terahertz detector. Such a detector is schematically depicted in Fig. 3. Contacts are positioned so to provide a lateral electric field. Upon absorption of the incident radiation the electron concentration in the well increases and leads to a photocurrent. However, strong reverse process was indicated in Ref. [21] that carriers in the conduction band of the well and bulk also efficiently scatter into the rod which can degrade the effect of detection. Therefore, this proposition for the efficient photodetector utilizing bound-to-BIC transition still needs to be carefully examined.

6. Conclusion

In summary, we proved that quantum rods can accommodate the excited normalizable state, energetically embedded in the continuum of the subband of the quantum well embedding it, where the electrons can be ionized into. We proved that existence of such states is entirely due to the interplay of two different types of confinement, namely the dot 3D confinement and the well confinement in the growth direction. We indicated that QRs are unique structures with this exotic mathematical property. As recently realized structures, quantum rods have not been extensively studied

experimentally, and we expect that interesting dynamical features due to the combined properties of bound and free states could arise.

Acknowledgements

N.P. acknowledges the support in part by the University of Leeds Fully Funded International Research Scholarships program and in part by the Ministry of Education and Science, Republic of Serbia, Scholarship program for students studying at the world's leading universities. V.M. acknowledges the support by Ministry of Education and Science, Republic of Serbia (Project III45010). Authors acknowledge support of NATO Science for Peace and Security project EAP.SFPP 984068 and European Cooperation in Science and Technology (COST) Actions BM1205 and MP1204.

Appendix A. Full solution to the model

In this appendix we provide the full solution to the radial equation (2). It can be rewritten as

$$\rho^2 \frac{d^2 R(\rho)}{d\rho^2} + \rho \frac{dR(\rho)}{d\rho} + ((k_{d/w}^n)^2 \rho^2 - l^2) R(\rho) = 0 \tag{A.1}$$

where the radial wavenumber depends on quantum number n only and is defined as

$$(k_{d/w}^n)^2 = \frac{2m_{d/w}}{\hbar^2} \left[E - E_{c,d/w} - \frac{\hbar^2 n^2 \pi^2}{2m_{d/w} h^2} \right] \tag{A.2}$$

Subscripts d and w refer to the dot and well domain, respectively. All material parameters are constant within each of these regions. For a fixed n , the wavenumber squared for the dot region $(k_d^n)^2$ is positive in the range of energies $E > \frac{\hbar^2 n^2 \pi^2}{2m_d h^2}$. However, the wavenumber squared for the well region $(k_w^n)^2$ is negative in energy interval $E < U_b + \frac{\hbar^2 n^2 \pi^2}{2m_w h^2}$.

Therefore, the solution for an energy in the interval $\frac{\hbar^2 n^2 \pi^2}{2m_d h^2} < E < U_b + \frac{\hbar^2 n^2 \pi^2}{2m_w h^2}$ reads

$$R_{nl}(\rho) = \begin{cases} C_1 J_l(k_d^n \rho) & \text{for } \rho < \rho_0 \\ C_2 K_l(\kappa_w^n \rho) & \text{for } \rho > \rho_0 \end{cases} \tag{A.3}$$

where we used the standard Bessel function notation and introduced $(\kappa_w^n)^2 = -(k_w^n)^2$ which is positive real number for the considered energy interval. The Bessel function of the second kind Y_l and modified Bessel function of the first kind I_l are absent from the solution due to their divergent behavior in corresponding domains. Boundary conditions at $\rho = \rho_0$ are the continuity of radial wavefunction and continuity of its derivative divided by effective mass, and lead to homogeneous system of linear equations in C_1 and C_2 which has a solution if

$$\frac{\kappa_w^n}{m_w} J_l(\rho_0 k_d^n) \frac{d}{d\rho} (K_l(\rho_0 \kappa_w^n)) = \frac{k_d^n}{m_d} K_l(\rho_0 k_d^n) \frac{d}{d\rho} (J_l(\rho_0 k_d^n)) \tag{A.4}$$

By solving this transcendental equation one obtains the discrete energy spectrum for fixed n and l and those solutions are numbered with index j . Eq. (A.4) has to be solved in the energy range $\frac{\hbar^2 n^2 \pi^2}{2m_d h^2} < E < U_b + \frac{\hbar^2 n^2 \pi^2}{2m_w h^2}$, but further narrowing of this range exists for $l \neq 0$. Taking into account the condition that energies of discrete levels have to be above the minima of effective potential one can show that narrowed energy range for solving Eq. (A.4) is $\frac{\hbar^2}{2m_d} (\frac{n^2 \pi^2}{h^2} + \frac{l^2}{\rho_0^2}) < E < U_b + \frac{\hbar^2 n^2 \pi^2}{2m_w h^2}$.

Each discrete energy defines the radial wavenumbers $k_{w/d}^{nj}$ and $\kappa_{w/d}^{nj}$ which do not depend explicitly on l (only implicitly,

via the solutions for discrete spectrum). The corresponding radial wavefunctions are

$$R_{nlj}(\rho) = \begin{cases} C_1 J_l(k_d^{nj} \rho) & \text{for } \rho < \rho_0 \\ C_1 \frac{J_l(k_d^{nj} \rho_0)}{K_l(k_w^{nj} \rho_0)} K_l(k_w^{nj} \rho) & \text{for } \rho > \rho_0 \end{cases} \quad (\text{A.5})$$

where the C_1 is determined by normalization.

For the remaining range of energies, i.e. $E > U_b + \frac{\hbar^2 n^2 \pi^2}{2m_w \hbar^2}$ the spectrum is continual and for each energy the corresponding radial wavefunction is

$$R_{nlE}(\rho) = \begin{cases} C_1 J_l(k_d^n \rho) & \text{for } \rho < \rho_0 \\ C_2 J_l(k_w^n \rho) + C_3 Y_l(k_w^n \rho) & \text{for } \rho > \rho_0 \end{cases} \quad (\text{A.6})$$

By using the same boundary and normalization condition one can obtain the constants C_1 , C_2 and C_3 . There are infinitely many continuum states for any energy counted by quantum number l , in contrast to discrete part of the spectrum where boundary conditions do not allow solutions to exist for values of quantum number l higher than some critical value. Such upper bound to the quantum number l depends also on quantum number n . For increasing value of n , the upper bound of l decreases and eventually there will be no discrete states for some critical value of quantum number n .

Consider now the general case of discrete states with quantum numbers $n = q_n$ and $l = q_l$. Such states can occur in the energy range $\frac{\hbar^2}{2m_d} (\frac{q_n^2 \pi^2}{\hbar^2} + \frac{q_l^2}{\rho_0^2}) < E < U_b + \frac{\hbar^2 q_n^2 \pi^2}{2m_w \hbar^2}$. (It is implicitly assumed that q_n and q_l are small enough so $\frac{\hbar^2}{2m_d} (\frac{q_n^2 \pi^2}{\hbar^2} + \frac{q_l^2}{\rho_0^2}) < U_b + \frac{\hbar^2 q_n^2 \pi^2}{2m_w \hbar^2}$.) We want to find the conditions for which the continuum with quantum number $n = p$ can embed the given bound state. The continuum with quantum number $n = p$ exists for energies $E > U_b + \frac{\hbar^2 p^2 \pi^2}{2m_w \hbar^2}$. Therefore, if $U_b + \frac{\hbar^2 p^2 \pi^2}{2m_w \hbar^2} < \frac{\hbar^2}{2m_d} (\frac{q_n^2 \pi^2}{\hbar^2} + \frac{q_l^2}{\rho_0^2})$, then a bound state with quantum numbers $n = q_n$ and $l = q_l$ can occur in the continuum of quantum number p in the range of energies $\frac{\hbar^2}{2m_d} (\frac{q_n^2 \pi^2}{\hbar^2} + \frac{q_l^2}{\rho_0^2}) < E < U_b + \frac{\hbar^2 q_n^2 \pi^2}{2m_w \hbar^2}$.

On the other hand, if $U_b + \frac{\hbar^2 p^2 \pi^2}{2m_w \hbar^2} > \frac{\hbar^2}{2m_d} (\frac{q_n^2 \pi^2}{\hbar^2} + \frac{q_l^2}{\rho_0^2})$ then bound state in the continuum occurs for energies satisfying $U_b + \frac{\hbar^2 p^2 \pi^2}{2m_w \hbar^2} < E < U_b + \frac{\hbar^2 q_n^2 \pi^2}{2m_w \hbar^2}$.

References

- [1] J. von Neumann, E. Wigner, *Zeitschrift für Physik* 30 (1929) 465.
- [2] F.H. Stillinger, D.R. Herrick, *Physical Review A* 11 (1975) 446.
- [3] F. Capasso, C. Sirtori, J. Faist, D.L. Sivco, S.G. Chu, A.Y. Cho, *Nature* 358 (1992) 565.
- [4] L.S. Cederbaum, R.S. Friedman, V.M. Ryaboy, N. Moiseyev, *Physical Review Letters* 90 (2003) 013001.
- [5] H. Nakamura, N. Hatano, S. Garmon, T. Petrosky, *Physical Review Letters* 99 (2007) 210404.
- [6] N. Moiseyev, *Physical Review Letters* 102 (2009) 167404.
- [7] J.S. Petrovic, V. Milanovic, Z. Ikonic, *Physics Letters A* 300 (2002) 595.
- [8] A.F. Sadreev, E.N. Bulgakov, I. Rotter, *Physical Review B* 73 (2006) 235342.
- [9] M.I. Molina, A.E. Miroshnichenko, Y.S. Kivshar, *Physical Review Letters* 108 (2012) 070401.
- [10] W. Hsueh, C. Chen, C. Chang, *Physics Letters A* 374 (2010) 4804.
- [11] D.C. Marinica, A.G. Borisov, S.V. Shabanov, *Physical Review Letters* 100 (2008) 183902.
- [12] Y. Plotnik, O. Peleg, F. Dreisow, M. Heinrich, S. Nolte, A. Szameit, M. Segev, *Physical Review Letters* 107 (2011) 183901.
- [13] N. Prodanovic, V. Milanovic, J. Radovanovic, *Journal of Physics A – Mathematical and Theoretical* 42 (2009) 415304.
- [14] M. Robnik, *Journal of Physics A – Mathematical and General* 19 (1986) 3845.
- [15] P. Ridha, L. Li, A. Fiore, G. Patriarche, M. Mexis, P.M. Smowton, *Applied Physics Letters* 91 (2007) 191123.
- [16] L. Li, G. Patriarche, N. Chauvin, P. Ridha, M. Rossetti, J. Andrzejewski, G. Sek, J. Misiewicz, A. Fiore, *IEEE Journal of Selected Topics in Quantum Electronics* 14 (2008) 1204.
- [17] C.M. Morris, D. Stehr, H. Kim, T.-A. Truong, C. Pryor, P.M. Petroff, M.S. Sherwin, *Nano Letters* 12 (2012) 1115.
- [18] R. Nedzinskas, B. Cechavicius, J. Kavaliauskas, V. Karpus, G. Valusis, L. Li, S. Khanna, E. Linfield, *Nanoscale Research Letters* 7 (2012) 609.
- [19] N. Prodanović, N. Vukmirović, D. Indjin, Z. Ikonić, P. Harrison, *Journal of Applied Physics* 111 (2012) 073110.
- [20] S. Tomić, *Physical Review B* 82 (2010) 195321.
- [21] D. Stehr, C.M. Morris, D. Talbayev, M. Wagner, H.C. Kim, A.J. Taylor, H. Schneider, P.M. Petroff, M.S. Sherwin, *Applied Physics Letters* 95 (2009) 251105.

Relationship between electron-LO phonon and electron-light interaction in quantum dots

Nikola Prodanović,* Zoran Ikonić, Dragan Indjin, and Paul Harrison

*Institute of Microwaves and Photonics, School of Electronic and Electrical Engineering, University of Leeds,
Woodhouse Lane, Leeds LS2 9JT, United Kingdom*

(Received 23 February 2012; published 16 May 2012)

The relationship between the Frölich electron-LO phonon interaction and the electron-light interaction in the conduction band of quantum dots (QDs) based on polar semiconductors is investigated and used to parametrize the intersublevel polaron lifetime. Based on this, the ratio of the optical gain cross section and nonradiative lifetime is described in terms of the QD geometrical and compositional parameters, which is important for possible intraband lasing transitions in QDs.

DOI: [10.1103/PhysRevB.85.195435](https://doi.org/10.1103/PhysRevB.85.195435)

PACS number(s): 78.67.Hc, 71.38.-k, 73.21.La

I. INTRODUCTION

In the last two decades, quantum dots have attracted considerable attention as potential candidates for improved lasing properties compared to their quantum well counterparts. The modified density of states due to the 3D quantum confinement increases the efficiency of lasing in comparison to the standard 1D confined structures, i.e., the quantum wells.^{1,2} Experimental evidence that the system with truly discrete states should have a lower threshold current comes from the extremely low threshold currents observed in quantum-well-based quantum cascade lasers in the strong magnetic field.^{3,4}

In Refs. 5 and 6 it was suggested that the dominant transition observed in the PL spectra is the transition between *s*-like and *p*-like states, which was based on numerical calculation of electronic states and optical matrix elements within the dipole approximation. There have been several reports on the observed intraband photoluminescence based on the *s-p*-like transitions in the quantum dot cascades.⁵⁻⁷ Room temperature intraband photoluminescence was observed in Ref. 8. However, lasing has not yet been observed.

Several theoretical proposals have been made for an intersublevel quantum dot cascade laser. They are either 2-level systems utilizing the *s-p*-like resonant transition for lasing⁹⁻¹¹ or 3-level systems¹² with the lasing transition between higher excited states in the quantum dots (QDs). The resonant *s-p*-like transition might be used for lasing in future designs of the QD intersublevel emitter. If not, we will here restrict considerations to this transition and the derived theory can be applied to other cases with a few modifications.

This resonant *s-p*-like transition requires a detailed investigation in terms of the radiative and nonradiative transition strengths. In order to obtain lasing, the strength of the radiative transition has to overcome population inversion losses due to nonradiative transitions. Therefore, the theoretical description of radiative and nonradiative relaxation processes is crucial, and it would be convenient to provide a theoretical insight which incorporates both nonradiative and radiative transitions.

The dipole approximation of the electron-radiation coupling has been widely accepted and used for the absorption and emission processes in various semiconductor nanostructures. The dipole approximation assumes that the light wavelength is substantially larger than the dot size, and therefore the electromagnetic field can be considered as spatially constant.

On the other hand the main source of nonradiative transitions comes from the electron-phonon coupling. Phonons behave as waves in the same manner as photons, and their second quantization is performed analogously.

The dominant electron-phonon interaction is Frölich interaction of electrons and longitudinal optical (LO) phonons. The Frölich interaction can be viewed as interaction of an electron and electromagnetic wave induced by dipole-like LO phonon vibrations. This sets up an analogy between the electron-phonon and the electron-photon interactions. The fundamental difference is that wave vectors of the relevant phonons are larger than those of photons and the dipole approximation does not hold for phonons.

Detailed theoretical predictions on the key nonradiative relaxation processes in the QD structures caused by Frölich interaction have evolved, relying on an increasing amount of available experimental data. First, it was thought that due to the discrete nature of the electronic structure and the nearly constant energy of LO phonons, the so-called phonon bottleneck would occur.¹³ However, a great amount of experimental data showed the absence of this effect.^{14,15}

Magneto-optical experiments in Refs. 16 and 17 showed that QDs behave like complex condensed matter systems where electrons and phonons interact strongly via polar Frölich coupling, thus forming quasiparticles, so-called polarons. Therefore, the simple picture of weak electron-phonon interaction was not appropriate.^{18,19} The most prominent theoretical justification for a short lifetime of excited carriers in QDs has been presented in Refs. 15 and 20, where the lattice anharmonicity perturbation enables the energy exchange between different polaron modes, thus enabling relaxation toward the thermodynamical equilibrium.

The electron-phonon interaction remains the fundamental factor governing excited carrier nonradiative relaxation in QDs. The main aim of this work is to develop a simple model to establish a relationship between the radiative and the nonradiative transition strengths of carriers in QDs. The basis for it is a similar physical electromagnetic interaction between electrons and phonons, and electrons and photons. We will elaborate the relationship between these two interactions, and a short review of finite polaron lifetime theory will follow together with a model for optical gain and absorption coefficients. The model will then be used to derive important conclusions on the geometrical and compositional optimization of QDs as

possible active media. We will also underline the important role of state-of-the-art postgrowth fabrication modifications of QDs such as rapid thermal annealing²¹ or quantum rod elongation^{22,23} in future optimizations.

II. THE RELATIONSHIP

Since we are interested only in *s-p*-like resonant coupling we introduce a reduction of the one-electron subspace into only the ground and the first excited electron states. Those electronic states will be further labeled with $|\psi_a\rangle$ and $|\psi_b\rangle$, or shortly $|a\rangle$ and $|b\rangle$, with energies E_a and E_b .

In this two-level system, the most important parameter regarding the electron-light interaction in dipole approximation is coordinate matrix element $\mathcal{R}_{ab} = \int d^3\mathbf{r} \psi^{(a)*}(\mathbf{r}) \hat{\mathbf{r}} \psi^{(b)}(\mathbf{r})$ and will be referred to as a ‘‘dipole coupling vector.’’ On the other hand, the same parameter for the Frölich interaction of the electron with the LO phonon mode with wave vector \mathbf{k} is $\mathcal{H}_{ab}^k = \int d^3\mathbf{r} \psi^{(a)*} \frac{e^{i\mathbf{k}\cdot\mathbf{r}}}{k} \psi^{(b)}$ and will be referred to as a ‘‘Frölich coupling function’’ (FCF) on wave vector \mathbf{k} . The main aim here is to find a relationship between the dipole coupling vector \mathcal{R}_{ab} and Frölich coupling function \mathcal{H}_{ab}^k .

In quantum dots, due to confinement, the Frölich coupling function falls rapidly to zero even for relatively small values of wave vector \mathbf{k} . It behaves as a distribution function with *p*-orbital-like shape with the maximum value in the limit $k \rightarrow 0$. With the aim of estimating this value, one has to expand the expression for the Frölich coupling function as

$$\begin{aligned} \mathcal{H}_{ab}^k &= \int d^3\mathbf{r} \psi^{(a)*} \frac{\cos \mathbf{k} \cdot \mathbf{r}}{k} \psi^{(b)} + i \int d^3\mathbf{r} \psi^{(a)*} \frac{\sin \mathbf{k} \cdot \mathbf{r}}{k} \psi^{(b)} \\ &= \frac{1}{k} \int d^3\mathbf{r} \psi^{(a)*} \psi^{(b)} + i \mathbf{e}_k \cdot \int d^3\mathbf{r} \psi^{(a)*} \mathbf{r} \psi^{(b)} \\ &\quad - \frac{k}{2} \int d^3\mathbf{r} \psi^{(a)*} (\mathbf{e}_k \cdot \mathbf{r})^2 \psi^{(b)} \\ &\quad - i \frac{k^2}{6} \int d^3\mathbf{r} \psi^{(a)*} (\mathbf{e}_k \cdot \mathbf{r})^3 \psi^{(b)} + \dots, \end{aligned} \quad (1)$$

where the second equation represents the Taylor series of sine and cosine functions, and $\mathbf{e}_k = \frac{\mathbf{k}}{k}$.

Given that electronic states $|\psi_a\rangle$ and $|\psi_b\rangle$ are states with a dominant optical transition—i.e., the intensity of the dipole

coupling vector between these two states, \mathcal{R}_{ab} , is significant—then, in most cases, one concludes that states $\psi^{(a)}$ and $\psi^{(b)}$ have well-defined and opposite parity. Therefore, in such a case, the first term in Eq. (1) vanishes and one gets

$$\mathcal{H}_{ab}^k = i \left(\mathbf{e}_k \cdot \mathcal{R}_{ab} - \frac{k^2}{6} \int d^3\mathbf{r} \psi^{(a)*} (\mathbf{e}_k \cdot \mathbf{r})^3 \psi^{(b)} + \dots \right). \quad (2)$$

In the limit $k \rightarrow 0$ expression (2) becomes

$$\mathcal{H}_{ab}^k = \mathbf{e}_k \cdot \mathcal{R}_{ab}. \quad (3)$$

Hence, the maximum of the scalar field \mathcal{H}_{ab}^k is proportional to the intensity of the dipole coupling vector, and is at $k \rightarrow 0$.

It should be pointed that the FCF is singular at $k = 0$, and also the vector \mathbf{k} does not have a defined direction, and therefore the expression $\mathbf{e}_k \cdot \mathcal{R}_{ab}$ is not defined. However, the factor $\mathbf{e}_k \cdot \mathcal{R}_{ab}$ indicates that even for small k the distribution \mathcal{H}_{ab}^k has a strongly anisotropic behavior. For \mathbf{k} pointing in the direction of the dipole coupling vector, the FCF exhibits the weakest negative slope. This slope is increasing with increasing angle between \mathbf{k} and the FCF and decays rapidly to zero when \mathbf{k} becomes almost perpendicular to the dipole coupling vector. In the limit where \mathbf{k} is exactly perpendicular, the FCF is zero. All these features prove that the FCF has a *p*-orbital-like shape. This was indeed expected, since the FCF is essentially a Fourier transform of an even function.

One can demonstrate these statements by taking a simple example of a hard-wall cuboidal quantum dot where it is possible to calculate analytically \mathcal{H}_{12}^k between the ground and the first excited state. The results for the quantum box of height 20 nm and square basis side of 15 nm are presented in Fig. 1(a) in the k_x - k_z plane without losing generality. The FCF behaves in the same way in the direction k_x as in k_y , for a square base case.

Therefore, we can model the Frölich coupling function by a bell-shaped distribution function, with the maximal value at $k \rightarrow 0$ proportional to the intensity of the dipole coupling vector and multiplied by the $\frac{k_z}{k}$, where i denotes the direction

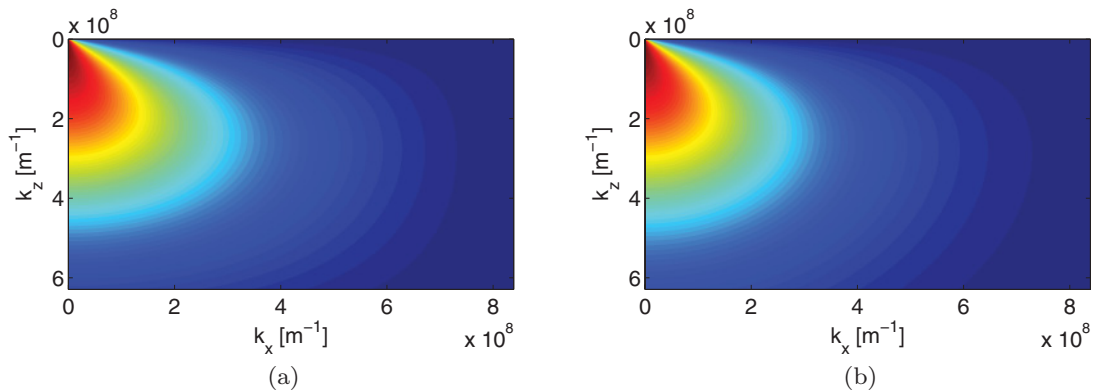


FIG. 1. (Color online) (a) The Frölich coupling function for a hard-wall box calculated in the k_x - k_z plane. The height of the dot is 20 nm and the square basis side is 15 nm. (b) The Frölich coupling function modeled by a Gaussian with fitted line width inversely proportional to the dot dimensions of the hard-walled QD. The whole Gaussian is multiplied by the cosine of the angle between \mathbf{k} and k_z .

of the dipole coupling vector. This model gives

$$|\mathcal{H}_{ab}^k| = |\mathcal{R}_{ab}| \frac{k_z}{\sqrt{k_x^2 + k_y^2 + k_z^2}} \mathcal{I}(\mathbf{k}), \quad (4)$$

where $\mathcal{I}(\mathbf{k})$ is the anisotropic distribution function with maximum $\mathcal{I}(0) = 1$. Therefore, we have parametrized the FCF via two factors. One is the dipole coupling vector \mathcal{R}_{ab} which is a well-known spectroscopic quantity, and the second is the distribution function with the property $\mathcal{I}(0) = 1$. All details of the quantum dot are hidden in the width and line shape of this function. We will show later that the most important quantity regarding nonradiative relaxation is the integral of the squared absolute value of distribution function. This is why the exact line shape has a limited significance. On the other hand, we will show that widths of the distribution functions are closely related to the size of the quantum dot in the corresponding direction.

III. POLARON STATES

Electrons and LO phonons are in a strong-coupling regime in the polar semiconductor quantum dots.^{16,24} The full Hamiltonian to be considered accounts for the Frölich coupling between electrons and LO phonons, i.e.,

$$H = H_e + H_{ph} + \sqrt{\frac{e^2 \hbar \omega_{LO}}{2V} \left(\frac{1}{\epsilon_\infty} - \frac{1}{\epsilon_{st}} \right)} \times \sum_{ijk} \mathcal{H}_{ij}^k \hat{a}_i^+ \hat{a}_j (\hat{b}_k + \hat{b}_{-k}^+), \quad (5)$$

where H_e is the electronic part of the Hamiltonian, H_{ph} is the phonon part of the Hamiltonian, \hat{b}_k and \hat{b}_k^+ are phonon annihilation and creation operators, and \hat{a}_i and \hat{a}_i^+ are the corresponding operators for electrons. It has been argued that one has to diagonalize this full Hamiltonian in order to obtain agreement with results obtained in magneto-optical experiments.^{15–17}

The diagonalization procedure from Ref. 19 has been adopted here. The Hamiltonian, Eq. (5), commutes with the electron number operator \hat{N} and therefore can be solved in each subspace for a constant number of electrons. Therefore, the one-electron limitation is introduced here together with the two-level system explained above.

The eigenstates of the trivial case of the Hamiltonian without electron-phonon interaction is a simple uncorrelated eigenbasis formed by the direct product of a pure electronic eigenstates and pure phonon eigenstates. When it comes to the full Hamiltonian, as has been proved in Refs. 17 and 19, only a finite number of LO modes couples with a finite number of electronic states in the nondispersive phonon modes approximation. For two-level electronic systems only three LO modes are considered. Their further orthonormalization²⁵ and proper unitary rotation give three new modes which are coupled to a two-level system with one electron. Only one mode couples the s - p resonant transition to the classical emission or absorption of one phonon and will be denoted as B_1 . The second mode couples the s - p resonant transition with the self-translation which gives rise to the Franck-Condon factors.¹⁹ It will be denoted as B_2^γ where the parameter γ

represents translation. The third mode is properly translated so it does not couple to the resonant s - p transition in the one-electron case and can be omitted from further consideration.

Further space reduction was obtained in Ref. 19 by introducing the rotating wave approximation, by choosing only the coupling states differing by the detunings $\delta_\pm = E_b - E_a \pm \hbar \omega_{LO}$. The first state has the electron in state b and “certain phonon configuration.” The second state has the electron in state a and the same phonon configuration, with only one additional phonon in mode B_1 and “translated” mode B_2^γ with the same occupation number. The relationship between these translated and initial modes is determined by general Franck-Condon factors. By neglecting the polaronic shift terms, it is possible to obtain approximate analytical solution of any such 2×2 Hamiltonian. Thus, the basis considered is

$$|2'\rangle = |b; n_1^0; n_2^\gamma\rangle, \quad |3'\rangle = |a; n_1^0 + 1; n_2^0\rangle,$$

where $n_1 = n_2 = 0$. We additionally take two adjacent states into account, namely the ground state a with zero phonons (i.e., uncorrelated ground state) and its coupling state b with one phonon in mode B_1 and the “translated” mode B_2^γ with the same occupation number:

$$|1'\rangle = |a; n_1^0; n_2^0\rangle, \quad |4'\rangle = |b; n_1^0 + 1; n_2^\gamma\rangle.$$

The superscript at the phonon modes denotes translation of the mode from the bulk one. Enumeration of the basis states is made to order the states according to their increasing energy; i.e., we consider the case where the detuning is $\delta_- < 0$.

The solution of this model is also given in Ref. 19 and it reads

$$\begin{aligned} |1\rangle &= \sqrt{\frac{1}{2} \left(1 - \frac{\delta_+}{R_+} \right)} |4'\rangle + \sqrt{\frac{1}{2} \left(1 + \frac{\delta_+}{R_+} \right)} |1'\rangle, \\ |2\rangle &= \sqrt{\frac{1}{2} \left(1 - \frac{\delta_-}{R_-} \right)} |2'\rangle - \sqrt{\frac{1}{2} \left(1 + \frac{\delta_-}{R_-} \right)} |3'\rangle, \\ |3\rangle &= \sqrt{\frac{1}{2} \left(1 + \frac{\delta_-}{R_-} \right)} |2'\rangle + \sqrt{\frac{1}{2} \left(1 - \frac{\delta_-}{R_-} \right)} |3'\rangle, \\ |4\rangle &= \sqrt{\frac{1}{2} \left(1 + \frac{\delta_+}{R_+} \right)} |4'\rangle - \sqrt{\frac{1}{2} \left(1 - \frac{\delta_+}{R_+} \right)} |1'\rangle, \end{aligned}$$

where $R_+ = \sqrt{\delta_+^2 + 4|F_n^\gamma C_{ab}|^2}$ and $R_- = \sqrt{\delta_-^2 + 4|F_n^\gamma C_{ab}|^2}$ are the Rabi splittings, while $F_n^\gamma = \langle n|n \rangle_\gamma$ is the Franck-Condon factor and $C_{ab} = \sum_{\mathbf{q}} |M_{ab}(\mathbf{q})|^2$ is a normalization constant used to normalize the mode B_1 . If one assumes zero energy of the state $|1'\rangle$ the eigenenergies of this polaron model are

$$\begin{aligned} E_1 &= \frac{1}{2}(\delta_+ - R_+), & E_2 &= \frac{1}{2}(\delta_+ - R_-), \\ E_3 &= \frac{1}{2}(\delta_+ + R_-), & E_4 &= \frac{1}{2}(\delta_+ + R_+). \end{aligned}$$

In conclusion to this section, the most important quantity, directly responsible for formation of the coherent polaron modes, is the normalization constant C_{ab} . In terms of the FCF this normalization constant reads

$$C_{ab} = \frac{e^2 \hbar \omega_{LO}}{16\pi^3} \left(\frac{1}{\epsilon_\infty} - \frac{1}{\epsilon_{st}} \right) \int d^3 \mathbf{k} |\mathcal{H}_{ab}^k|^2 \quad (6)$$

and will be further referred to as the Frölich coupling constant. By using the relation (4), the Frölich coupling constant becomes

$$|C_{ab}|^2 = \frac{e^2 \hbar \omega_{LO}}{16\pi^3} \left(\frac{1}{\epsilon_\infty} - \frac{1}{\epsilon_{st}} \right) |\mathcal{R}_{ab}|^2 S, \quad (7)$$

where

$$S = \int d^3 \mathbf{k} \frac{k_z^2}{k_x^2 + k_y^2 + k_z^2} \mathcal{I}^2(\mathbf{k}) \quad (8)$$

will be further on referred to as the coupling integral constant.

We have deconstructed the Frölich coupling constant for any quantum dot via factors containing the dipole coupling vector and integrals of the distribution function. Due to this integral, the precise shape of this distribution function becomes unimportant, and only its linewidth remains as a crucial factor determining the value of the coupling integral constant S .

IV. INFLUENCE OF QD GEOMETRY AND COMPOSITION

In the following we give a quantitative description of the influence of the QD confinement on the value of expression (6). Consider first the distribution function. Anisotropy of this function stems from the dimensional anisotropy of the dot. Thus, for anisotropic QDs the linewidth of such a distribution function varies with the direction in \mathbf{k} space.

The Frölich coupling function can be thought of as a Fourier transform of the product of wave functions in the ground and excited state divided by k . By varying the dot dimensions we can shrink or expand the envelope wave functions. This can be modeled by

$$\psi(x, y, z) \rightarrow \sqrt{\alpha_x \alpha_y \alpha_z} \psi(\alpha_x x, \alpha_y y, \alpha_z z). \quad (9)$$

Using these scaled wave functions in the Frölich coupling function, and taking a particular direction, e.g., the “ x ” direction (i.e., setting $k_y = k_z = 0$), one concludes that the

FCF has the behavior

$$\mathcal{H}_{ab}(k_x, 0, 0) \rightarrow \frac{1}{\alpha_x} \mathcal{H}_{ab}\left(\frac{k_x}{\alpha_x}, 0, 0\right). \quad (10)$$

However, the prefactor $\frac{1}{\alpha_x}$ is already included in the scaling of the dipole coupling vector, and therefore only the scaling of the distribution function width has to be considered further. By increasing the dot size in the chosen direction one can decrease the distribution function width in that direction. However, this trend remains up to some minimal, critical size in a particular direction. Beyond this point, the envelope wave function does not shrink any further, but instead starts leaking outside the dot. In the hard-wall example, it is possible to use a Gaussian without a normalization prefactor as a distribution function. The results of such a model are presented in Fig. 1(a). The width of the Gaussian is inversely proportional to the dot extension in the corresponding direction. The modeling by the Gaussian curve is also the exact solution for a parabolic QD (see Appendix of Ref. 19).

For calculations with better accuracy we use an 8-band $\mathbf{k} \cdot \mathbf{p}$ method with strain effects included to calculate the Frölich coupling function and demonstrate its dependence on the dot size.^{11,18,26,27} In Figs. 2(a) and 2(b) we present the calculated FCF for lens-shaped dots of height 8 nm, indium content 1, and radius 22 nm. The second dot is twice as high, 16 nm, and we note that FCF has accordingly shrunk twofold in this direction. The In content in the QD also affects the width of the distribution function. By decreasing the In content one decreases the QD potential well and the confinement. The wave functions then expand and the FCF consequently shrinks, and so does the distribution function. This is demonstrated in Figs. 3(a) and 3(b), where two geometrically identical QDs (cylinder shaped) have different In content, of 1 and 0.6, respectively. We note that FCF in Fig. 3(b) is slightly narrower than that in Fig. 3(a). It is expected that the maximal possible width of the distribution function in terms of QD depth occurs for the hard-wall QD, since it has infinite potential well. The opposite limit occurs in bulk, where the width is zero; i.e., the

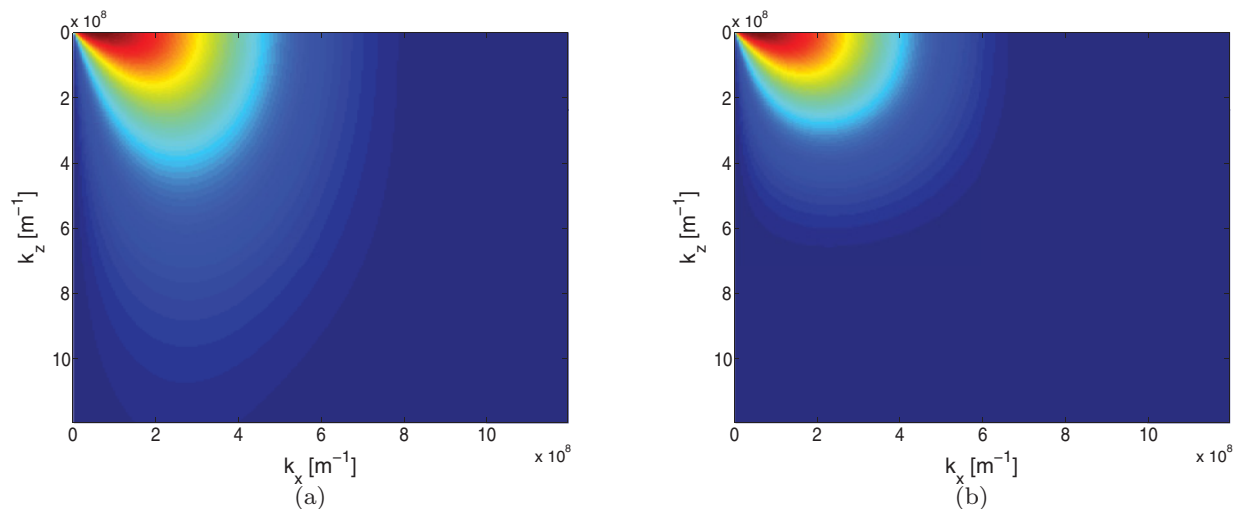


FIG. 2. (Color online) FCF for two different lens-shaped cylindrically symmetric QDs calculated in the k_x - k_z plane by the 8-band $\mathbf{k} \cdot \mathbf{p}$ method with strain effects included. Indium content in both dots is 1, radius is 22 nm, and their height is (a) 8 nm and (b) 16 nm.

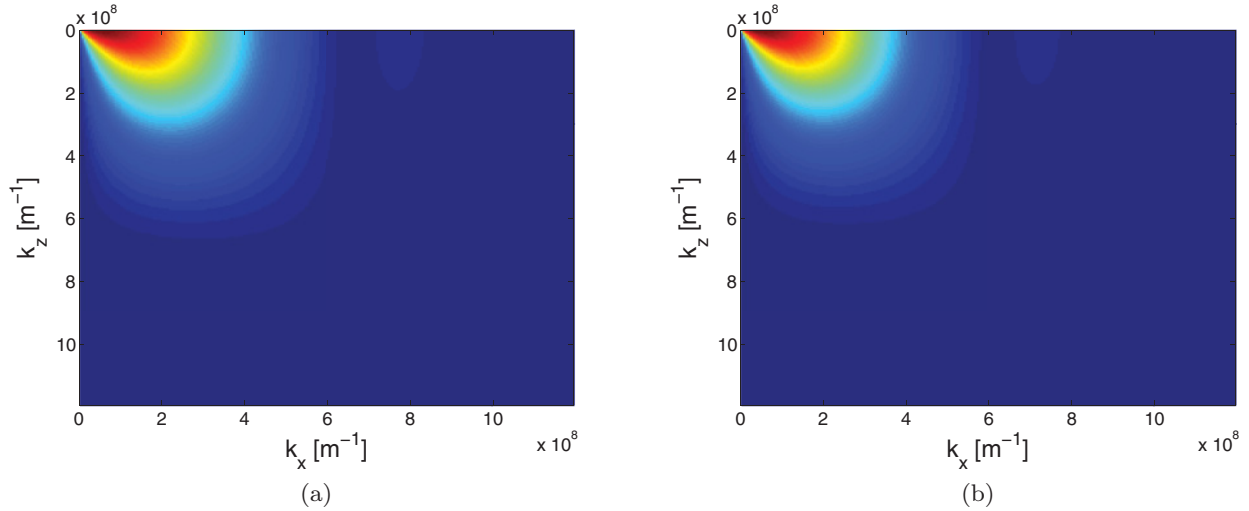


FIG. 3. (Color online) (a) FCF for two different cylinder-shaped QDs calculated in the k_x - k_z plane by the 8-band $\mathbf{k} \cdot \mathbf{p}$ method with strain effects included. Indium content in dots is (a) 1 and (b) 0.6, and their radius and height are 22 nm and 12 nm, respectively, in both cases.

wave function is a pure plane wave. It is difficult to predict a more accurate dependence of the width of the distribution function, but a monotonic behavior is expected between these two limits.

In summary, we have introduced four parameters: $\alpha_x, \alpha_y, \alpha_z$, and σ . The first three parameters measure the relative QD extension in a specified direction, and the parameter σ is an increasing function of the In content in the QD. By varying these geometrical parameters the distribution function evolves as

$$\mathcal{I}(k_x, k_y, k_z) \rightarrow \mathcal{I}\left(\frac{\alpha_x}{\sigma}k_x, \frac{\alpha_y}{\sigma}k_y, \frac{\alpha_z}{\sigma}k_z\right) \quad (11)$$

and consequently the coupling integral constant evolves as

$$S \rightarrow \int d^3\mathbf{k} \frac{k_z^2}{k_x^2 + k_y^2 + k_z^2} \mathcal{I}\left(\frac{\alpha_x}{\sigma}k_x, \frac{\alpha_y}{\sigma}k_y, \frac{\alpha_z}{\sigma}k_z\right), \quad (12)$$

which gives

$$\begin{aligned} S &\rightarrow \frac{\sigma^3}{\alpha_x \alpha_y \alpha_z} \int d^3\mathbf{k} \frac{k_z^2}{\left(\frac{\alpha_x}{\sigma}\right)^2 k_x^2 + \left(\frac{\alpha_y}{\sigma}\right)^2 k_y^2 + k_z^2} \mathcal{I}(\mathbf{k}) \\ &= \frac{\sigma^3}{\alpha_x \alpha_y \alpha_z} S'. \end{aligned} \quad (13)$$

Equation (13) describes the variation of the coupling integral constant in terms of quantum dot geometric and composition parameters. The largest contribution comes from the prefactor. Coupling integral constant S is slightly different from S' ; i.e., it differs only by the “cosine part.” In the case of an isotropic enlargement of the QD size, the “cosine part” in the integrals remains unchanged and therefore so do the constants S and S' .

V. LIGHT ABSORPTION AND STIMULATED EMISSION

The polaron ground state is $|1\rangle$ with the dominant component being the electron ground state. In the case of $\delta_- < 0$, the first excited polaron state is $|2\rangle$. As expected, the dominant component of that state is the first excited electron state,

which enables efficient optical excitation of that polaron state from the ground state. Therefore, when dealing with optical excitation, we will omit the polaronic nature of the carriers in QDs and will derive expressions for the quantities of interest with pure electronic notation. Later, we will only replace the electronic notation with the corresponding polaronic notation. Let the system be described semiclassically, with particular interest in estimating the transition rate between the lower state $|a\rangle$ with energy E_a and the higher state $|b\rangle$ with energy E_b . Within this semiclassical approach, Fermi’s golden rule transition rate can be used to find the coefficients of absorption and stimulated emission gain in the active medium. The optical cross section gives the absorption line and gain when multiplied by the population difference. With the “ $-e\hat{\mathbf{r}} \cdot \mathbf{E}$ ” interaction the expression for optical cross section reads²⁸

$$\sigma_{ab}^e(\omega) = \frac{4\pi|e|^2\omega}{\bar{n}\varepsilon_0 c m_0^2} |\mathcal{R}_{ab} \cdot \mathbf{e}|^2 g(E_b - E_a \mp \hbar\omega), \quad (14)$$

where $g(E_b - E_a \mp \hbar\omega)$ is the normalized distribution function (e.g., Gaussian), recovering the inhomogeneous broadening due to the size inhomogeneity of the quantum dot ensemble and \mathbf{e} is the light polarization unit vector. Constants e , m_0 , \bar{n} , and c are electron charge and mass, refractive index of the quantum dot, and speed of light. The sign “ $-$ ” corresponds to absorption and “ $+$ ” to emission.

VI. NONRADIATIVE POLARON LIFETIME

After excitation, the relaxation of nonequilibrium polarons is enabled by anharmonic perturbation of the crystal. So far, this has been the most reliable theoretical explanation of the finite excited carrier lifetime proposed in Ref. 29. This potential acts only on the phonon factor in the polaron state. Besides the zero-phonon component in the excited polaron state, there is also a one-phonon component responsible for nonradiative relaxation of the excited polaron due to crystal anharmonicity potential. Therefore, the nonradiative decay rate has to be proportional to the absolute squared value of

the weights of the relevant components:

$$\Gamma(E_i) = \frac{1}{4}\Gamma_{\text{ph}}(E_i) \left(1 + \frac{\delta_+}{R_+}\right) \left(1 + \frac{\delta_-}{R_-}\right). \quad (15)$$

The quantity $\Gamma_{\text{ph}}(E_i)$ represents the bare decay rate of phonons which would have polaron energies driven by anharmonicity potential:

$$\Gamma_{\text{ph}}(E_i) = \frac{2\pi}{\hbar} \sum_j |\langle j|V_a|3'\rangle|^2. \quad (16)$$

The summation is performed over all possible decay channels of mode B_1 with one phonon. Detailed discussion on decay channels and the derivation of analytical expression for $\Gamma_{\text{ph}}(E_i)$ can be found in Ref. 29.

It was pointed out in Ref. 20 that a strong inhibition of this mechanism occurs at lower values of the energy splitting between the electronic ground and excited states. In other words, the squared detuning δ_-^2 becomes significantly larger than the squared Frölich coupling constant, leading to a simplified linearized ratio of detuning and Rabi splitting:

$$1 + \frac{\delta_-}{R_-} \approx 2 \frac{|F_n^\gamma C_{\text{ab}}|^2}{\delta_-^2}. \quad (17)$$

Furthermore, by using an additional approximation $\frac{\delta_+}{R_+} \approx 1$ and $F_n^\gamma \approx 1$, which holds for small values of the parameter γ , one can write

$$\Gamma(E_i) = \Gamma_{\text{ph}}(E_i) \frac{|C_{\text{ab}}|^2}{\delta_-^2}. \quad (18)$$

Therefore, the Frölich coupling constant is directly proportional to the lifetime of the excited carrier in the quantum dot.

VII. LASING EFFICIENCY

In order to consider a transition as a possible lasing transition, both the radiative and nonradiative lifetimes are important. The longer the nonradiative lifetime, the higher is the likelihood of photon emission. Thus, we define a figure of merit for such a transition as the ratio of the optical cross section and the nonradiative transition rate for the light polarized along the dipole coupling vector $K_{\text{ab}}(\omega) = \frac{\sigma_{\text{ab}}(\omega)}{\Gamma(E_i)}$. By using Eqs. (14) and (18) the lasing figure of merit becomes

$$K_{\text{ab}}(\omega) = \frac{64\pi^4 g(E_i \mp \hbar\omega)}{\bar{n}\epsilon_0 c m_0^2 \hbar^2 \omega_{\text{LO}} \left(\frac{1}{\epsilon_\infty} - \frac{1}{\epsilon_{\text{st}}}\right) S(E_i) \Gamma_{\text{ph}}}. \quad (19)$$

The inhomogeneous broadening $g(E_i \mp \hbar\omega)$ clearly affects this laser efficiency coefficient, via the optical cross section. Increasing the inhomogeneous broadening width will decrease the laser efficiency for a specific frequency of light. The ratio $\frac{E_i}{\Gamma_{\text{ph}}}$ is proportional to $\frac{1}{E_i^n}$, where n is an integer depending on the active disintegration channel. A detailed discussion on this subject is presented in Ref. 29, but the general conclusion is that a decrease of polaron s - p -like splitting E_i will lead to improved lasing efficiency. Dot enlargement and a reduced In content also lead to a decrease of the quantity S , as explained in the previous section. Furthermore, the squared detuning δ_-^2 then increases and leads to improved lasing efficiency.

It is clear now that novel postfabrication techniques such as rapid thermal annealing²¹ or quantum rod elongation^{22,23} could produce structures with higher lasing efficiency coefficient. One can enlarge the dot, or reduce the In content by using those techniques. In Ref. 20, it has been demonstrated that the nonradiative polaron lifetime is increased by rapid thermal annealing. However, we have shown here that this does not affect adversely the radiative lifetime, thus increasing the overall figure of merit (19).

VIII. CONCLUSION

In summary, in an ideal symmetric case, the FCF was parametrized with the dipole coupling vector (optical matrix element) and the distribution function whose widths were related to geometrical and compositional properties of the quantum dot. Based on such parametrization we have established a direct relationship between nonradiative lifetime and optical gain for a possible lasing transition in self-assembled quantum dots based on polar semiconductors. This was further used to derive an appropriate figure of merit for the lasing transition, which depends directly on geometrical parameters of the dot and on the level spacing. Enlargement of the quantum dot and reduction of In content in the dot lead to a higher figure of merit and both can be achieved by rapid thermal annealing. Novel structures such as quantum rods can be elongated in the growth direction, leading to a higher figure of merit.

Certainly, going to the extreme with such tailoring of dot structure will eventually bring in additional effects which may deteriorate lasing, and were not here accounted for. As the level spacing decreases, the thermal backfilling sets in, reducing the population inversion. Furthermore, the difficulty of selective electron injection into the excited state becomes more prominent as it gets close to the ground state.

Therefore, one has to solve the full system of rate equations in order to model the quantum-dot-based quantum cascade laser properly. The aim of this work was primarily to study the radiative versus nonradiative lifetimes, and to describe this problem via the minimum possible number of parameters. We also aimed to simplify the description of the Frölich coupling between confined electron states in the QD conduction band. The important parameters in this coupling have been deconstructed as much as possible to experimentally measurable spectroscopic quantities such as level spacing and dipole coupling vector.

ACKNOWLEDGMENTS

N.P. acknowledge the support in part by the University of Leeds Fully Funded International Research Scholarships program and in part by the Serbian Ministry of Education Scholarship program for students studying at the world's leading universities. The authors acknowledge support of NATO Science for Peace and Security Project No. EAP.SFPP 984068. The authors also acknowledge Nenad Vukmirovic for providing the 8-band $\mathbf{k} \cdot \mathbf{p}$ method based numeric solver used for some comparable simulations.

*elnpr@leeds.ac.uk

- ¹Y. Arakawa and H. Sakaki, *Appl. Phys. Lett.* **40**, 939 (1982).
- ²N. N. Ledentsov, M. Grundmann, F. Heinrichsdorff, D. Bimberg, V. M. Ustinov, A. E. Zhukov, M. V. Maximov, Z. I. Alferov, and J. A. Lott, *IEEE J. Sel. Top. Quantum Electron.* **6**, 439 (2000).
- ³G. Scalari, S. Blaser, J. Faist, H. Beere, E. Linfield, D. Ritchie, and G. Davies, *Phys. Rev. Lett.* **93**, 237403 (2004).
- ⁴A. Wade, G. Fedorov, D. Smirnov, S. Kumar, B. S. Williams, Q. Hu, and J. L. Reno, *Nature Photonics* **3**, 41 (2009).
- ⁵N. Ulbrich, J. Bauer, G. Scarpa, R. Boy, D. Schuh, G. Abstreiter, S. Schmult, and W. Wegscheider, *Appl. Phys. Lett.* **83**, 1530 (2003).
- ⁶C. Fischer, P. Bhattacharya, and P.-C. Yu, *Electron. Lett.* **39**, 1537 (2003).
- ⁷S. Anders, L. Rebohle, F. F. Schrey, W. Schrenk, K. Unterrainer, and G. Strasser, *Appl. Phys. Lett.* **82**, 3862 (2003).
- ⁸D. Wasserman, T. Ribaudo, S. A. Lyon, S. K. Lyo, and E. A. Shaner, *Appl. Phys. Lett.* **94**, 061101 (2009).
- ⁹C.-F. Hsu, J.-S. O. P. Zory, and D. Botez, *IEEE J. Sel. Top. Quantum Electron.* **6**, 491 (2000).
- ¹⁰V. M. Apalkov and T. Chakraborty, *Appl. Phys. Lett.* **78**, 1820 (2001).
- ¹¹N. Vukmirovic, D. Indjin, Z. Ikonic, and P. Harrison, *IEEE Photonics Technol. Lett.* **20**, 129 (2008).
- ¹²I. A. Dmitriev and R. A. Suris, *Phys. Status Solidi A* **202**, 987 (2005).
- ¹³U. Bockelman and G. Bastard, *Phys. Rev. B* **42**, 8947 (1990).
- ¹⁴S. Sauvage, P. Boucaud, R. P. S. M. Lobo, F. Bras, G. Fishman, R. Prazeres, F. Glotin, J. M. Ortega, and J.-M. Gérard, *Phys. Rev. Lett.* **88**, 177402 (2002).
- ¹⁵E. A. Zibik, L. R. Wilson, R. P. Green, G. Bastard, R. Ferreira, P. J. Phillips, D. A. Carder, J.-P. R. Wells, J. W. Cockburn, M. S. Skolnick, M. J. Steer, and M. Hopkinson, *Phys. Rev. B* **70**, 161305 (2004).
- ¹⁶S. Hameau, Y. Guldner, O. Verzellen, R. Ferreira, G. Bastard, J. Zeman, A. Lemaître, and J. M. Gérard, *Phys. Rev. Lett.* **83**, 4152 (1999).
- ¹⁷S. Hameau, J. N. Isaia, Y. Guldner, E. Deleporte, O. Verzellen, R. Ferreira, G. Bastard, J. Zeman, and J. M. Gérard, *Phys. Rev. B* **65**, 085316 (2002).
- ¹⁸N. Vukmirović, Z. Ikonić, D. Indjin, and P. Harrison, *Phys. Rev. B* **76**, 245313 (2007).
- ¹⁹T. Stauber, R. Zimmermann, and H. Castella, *Phys. Rev. B* **62**, 7336 (2000).
- ²⁰E. A. Zibik, T. Grange, B. A. Carpenter, N. E. Porter, R. Ferreira, G. Bastard, D. Stehr, S. Winnerl, M. Helm, H. Y. Liu, M. S. Skolnick, and L. R. Wilson, *Nature Mater.* **8**, 803 (2009).
- ²¹S. Fafard, Z. R. Wasilewski, C. N. Allen, D. Picard, M. Spanner, J. P. McCaffrey, and P. G. Piva, *Phys. Rev. B* **59**, 15368 (1999).
- ²²L. Li, G. Patriarche, N. Chauvin, P. Ridha, M. Rossetti, J. Andrzejewski, G. Sek, J. Misiewicz, and A. Fiore, *IEEE J. Sel. Top. Quantum Electron.* **14**, 1204 (2008).
- ²³J. He, H. J. Krenner, C. Pryor, J. P. Zhang, Y. Wu, D. G. Allen, C. M. Morris, M. S. Sherwin, and P. M. Petroff, *Nano Lett.* **7**, 802 (2007).
- ²⁴T. Inoshita and H. Sakaki, *Phys. Rev. B* **56**, R4355 (1997).
- ²⁵T. Stauber and R. Zimmermann, *Phys. Rev. B* **73**, 115303 (2006).
- ²⁶N. Prodanović, N. Vukmirović, D. Indjin, Z. Ikonić, and P. Harrison, *J. Phys.: Conf. Ser.* **242**, 012012 (2010).
- ²⁷N. Vukmirović, D. Indjin, V. D. Jovanović, Z. Ikonić, and P. Harrison, *Phys. Rev. B* **72**, 075356 (2005).
- ²⁸W. E. Lamb, R. R. Schlicher, and M. O. Scully, *Phys. Rev. A* **36**, 2763 (1987).
- ²⁹T. Grange, R. Ferreira, and G. Bastard, *Phys. Rev. B* **76**, 241304 (2007).

Electronic states and intraband terahertz optical transitions in InGaAs quantum rods

Nikola Prodanović, Nenad Vukmirović, Dragan Indjin, Zoran Ikonić, and Paul Harrison

Citation: *J. Appl. Phys.* **111**, 073110 (2012); doi: 10.1063/1.3692069

View online: <http://dx.doi.org/10.1063/1.3692069>

View Table of Contents: <http://jap.aip.org/resource/1/JAPIAU/v111/i7>

Published by the [AIP Publishing LLC](#).

Additional information on *J. Appl. Phys.*

Journal Homepage: <http://jap.aip.org/>

Journal Information: http://jap.aip.org/about/about_the_journal

Top downloads: http://jap.aip.org/features/most_downloaded

Information for Authors: <http://jap.aip.org/authors>

ADVERTISEMENT



AIP Advances

Now Indexed in Thomson Reuters Databases

Explore AIP's open access journal:

- Rapid publication
- Article-level metrics
- Post-publication rating and commenting

Electronic states and intraband terahertz optical transitions in InGaAs quantum rods

Nikola Prodanović,^{1,a)} Nenad Vukmirović,² Dragan Indjin,¹ Zoran Ikonić,¹ and Paul Harrison¹

¹*Institute of Microwaves and Photonics, School of Electronic and Electrical Engineering, University of Leeds, Woodhouse Lane, Leeds LS2 9JT, United Kingdom*

²*Scientific Computing Laboratory, Institute of Physics Belgrade, University of Belgrade, Pregrevica 118, 11080 Belgrade, Serbia*

(Received 30 August 2011; accepted 9 February 2012; published online 11 April 2012)

Strain-dependent eight-band $k \cdot p$ method is used to analyze the electronic structure and intraband optical transitions in self-assembled InGaAs quantum rods in the terahertz range. The calculation of absorption spectra for the growth- and in-plane-polarized radiation shows some similarities to those of quantum well and single quantum dot structures, augmented with contribution from transitions between the dot and quantum well states. The influence of rod height on the electronic structure and the intraband absorption spectra is also investigated. It is found that the energy of maximal terahertz absorption can be tailored by the rod height for both in-plane and in-growth polarized radiation. © 2012 American Institute of Physics. [<http://dx.doi.org/10.1063/1.3692069>]

I. INTRODUCTION

Semiconductor quantum dots are continuously attracting significant research interest, because their properties can be engineered, via their structural parameters, allowing the design of dots with electronic and optical properties suited to a particular application. In many cases, they are expected to offer better performance than similar devices based on quantum wells and wires. The growth of such structures is typically in the Stranski-Krastanov mode, which produces self-assembled dots with the height-to-diameter aspect ratio well below one and without a precise controllability of their size.

Novel quantum nanostructures—quantum rods or quantum posts—have recently been realized.^{1–4} In contrast to self-assembled quantum dots with typical heights of a few nanometers, quantum rods can be grown with heights up to several tens of nanometers. They have quite large aspect ratios, the controllability of which is achieved by alternating deposition of very short (of the order of monolayer) layers of InAs and GaAs. Subsequent intermixing of InAs and GaAs leads to InGaAs quantum rods with large and precisely tunable aspect ratio. Recent experiments on carrier capture dynamics in quantum rod structures⁵ suggest that quantum rods may be very promising for future device applications. There is also a very recent report⁶ that charged quantum rods embedded in a quantum well matrix give rise to a “perforated” electron gas. Additional growth control by using different arsenic sources has been reported.^{7,8}

It is, therefore, of interest to develop a full theoretical description of electronic and optical properties, which would enable the purpose engineering of quantum rod-based structures. Initial work in this area has focused on calculation of energy levels and interband optical properties,^{1,2,9} as well as theoretical investigation of dominant physical effects affect-

ing their interband optical properties.¹⁰ We have recently performed preliminary work on calculation of intraband (intersubband) absorption in the THz spectral range.¹¹ Following the recent experimental observation and theoretical analysis of terahertz ionization of highly charged quantum posts,⁶ in this work, we focus on detailed simulations of THz intraband optical absorption of polarized radiation at extremely low and liquid nitrogen temperatures. Within this scope, it suffices to consider the rod electronic structure alone, neglecting the formation of polaron states discussed in Ref. 12, because the spectrum of polaron states is not significantly different from a pure electronic spectrum in terms of optical probing.

We first briefly describe the strain-dependent eight-band $k \cdot p$ model for the electronic structure and the absorption cross sections calculation. The results are also compared to those obtained within the simple effective mass model, the latter being quite useful for qualitative insight.

II. THEORETICAL MODEL

A. Electronic structure: Eight band $k \cdot p$ model

The electronic structure of quantum rods is calculated within the eight-band envelope function $k \cdot p$ model.^{13–17} The strain distribution was found within the continuum mechanical model,¹⁸ with the calculation based on the finite element method.¹⁹

As for the rod cross section, both the cylindrical^{5,6,20} and square-based¹ shapes were reported. Yet, in our previous study of InGaAs quantum dots,²¹ we have shown that the intraband absorption spectrum is essentially the same for truncated square-based pyramids and truncated cones. This indicates that the details of the base shape (square versus circle) are not very important and have assumed the cylindrically shaped rods in our simulations, which should capture the essential features of an intraband absorption spectra of rods with different cross sections. Such an approximation is

^{a)}Electronic mail: elnpr@leeds.ac.uk.

further supported by the fact that, as described in Sec. II B–Sec. IV, the main features of bound-to-bound optical transitions are the same in the simple effective mass particle-in-a-box model for a square-based rod and in the full simulation with a cylindrical rod, and it is even less likely that the properties of unbound states are significantly affected by the exact shape of the rod base.

With the cylindrical shape of rods assumed, the axial approximation²¹ was used. The Hamiltonian eigenvalue problem was then solved using the orthonormal function expansion, where the basis was formed from the direct product of Bessel functions in the radial direction and plane waves in the growth (z) direction. The cylindrical symmetry of the rods introduces a good quantum number (m_f), describing the z – component of the total quasi-angular momentum, which takes half-integer values.^{21,22} The optical transition selection rules then allow only the transitions with $\Delta m_f = 0$ in the case of z – polarised radiation and $|\Delta m_f| = 1$ for the in-plane, e.g., x – polarised radiation.

The calculated electronic structure is then used to find the intraband absorption spectra. The case of $T = 0$ has been investigated previously,¹¹ assuming that only the ground state is occupied (the two-fold degeneracy of $|m_f|$ states then implies that no more than two electrons can be present in the quantum rod). In this work, we consider the lattice temperatures of either 0 K or 77 K. The latter case allows thermal population of higher states and absorption from these states as well. The inhomogeneity of the quantum rod ensemble (fluctuations of rod size and deviations of the base shape from perfect circular or square) gives contribution to transition linewidths and is taken into account by assuming a Gaussian line shape with a standard deviation σ equal to 10% of the transition energy, i.e., $\sigma = 0.1(E_f - E_i)$.

Under equilibrium conditions, a transition in the quantum rod has the effective absorption cross-section,

$$\sigma_e(i \rightarrow f) = \frac{2\pi\hbar}{\tilde{n}\epsilon_0 c E} \left| \frac{\langle i | \hat{H}' | f \rangle}{A} \right|^2 \frac{1}{\sigma\sqrt{2\pi}} \times \exp\left(-\frac{(E - (E_f - E_i))^2}{2\sigma^2}\right) \Theta_{if}, \quad (1)$$

where i and f denote the initial and final state and \tilde{n} the refractive index. The dipole perturbation $\hat{H}' = \frac{e}{m_0} \hat{\mathbf{p}} \cdot A\epsilon$ depends on the incident radiation magnetic vector potential A and its polarization unit vector ϵ , and Θ_{if} is the difference of the initial and final state population,

$$\Theta_{if} = \frac{1}{\exp\frac{(E_i - E_F)}{k_b T} + 1} - \frac{1}{\exp\frac{(E_f - E_F)}{k_b T} + 1},$$

where E_F is the Fermi level, determined by the average number of electrons in a rod.

B. Effective mass model

For a simple picture of phenomena observed in the detailed calculation, we also give a simple effective-mass

model of the electronic structure, dipole matrix elements, and optical cross-sections for states confined in the dot or in the well embedding the dot.

Consider a cuboidal quantum dot embedded in an infinite potential barrier with a square base of side length a and height d . Envelope functions of its eigenstates are

$$\Psi_i(x, y, z) = \frac{2\sqrt{2}}{a\sqrt{d}} \sin\left(\frac{x n_x^i \pi}{a}\right) \sin\left(\frac{y n_y^i \pi}{a}\right) \sin\left(\frac{z n_z^i \pi}{d}\right) \quad (2)$$

and the corresponding energies,

$$E_i = \frac{\pi^2 \hbar^2}{2m^* a^2} ((n_x^i)^2 + (n_y^i)^2) + \frac{\pi^2 \hbar^2}{2m^* d^2} (n_z^i)^2. \quad (3)$$

Similarly, in an infinitely deep quantum well, the eigenstates are

$$\Psi_{k_x, k_y, n}(x, y, z) = \frac{\sqrt{2}}{a\sqrt{d}} e^{ik_x x} e^{ik_y y} \sin\left(\frac{zn\pi}{d}\right) \quad (4)$$

and the corresponding energies

$$E_{k_x, k_y, n} = \frac{\hbar^2}{2m^*} (k_x^2 + k_y^2) + \frac{\pi^2 \hbar^2}{2m^* d^2} n^2, \quad (5)$$

where (k_x, k_y) is the in-plane wave vector and the quantum number n counts the subbands.

In order to use Eq. (1), one requires the momentum matrix element $\mathbf{p}_{if} = \int \Psi_i \hat{\mathbf{p}} \Psi_f d\mathbf{r}$. For light polarization, $\epsilon = \epsilon_x \mathbf{i} + \epsilon_z \mathbf{k}$, where z is the growth and x the in-plane direction, the momentum matrix elements are straightforwardly found as

$$p_{if}^x = \begin{cases} 4i\hbar \frac{\phi_{if}^x}{a} & \text{for } (n_x^i - n_x^f) \text{ odd} \\ 0 & \text{for } (n_x^i - n_x^f) \text{ even} \end{cases}, \quad (6a)$$

$$p_{if}^z = \begin{cases} 4i\hbar \frac{\phi_{if}^z}{d} & \text{for } (n_z^i - n_z^f) \text{ odd} \\ 0 & \text{for } (n_z^i - n_z^f) \text{ even} \end{cases}, \quad (6b)$$

where

$$\phi_{if}^x = \epsilon_x \delta_{n_x^i n_x^f} \delta_{n_z^i n_z^f} \frac{n_x^i n_x^f}{(n_x^i)^2 - (n_x^f)^2},$$

$$\phi_{if}^z = \epsilon_z \delta_{n_x^i n_x^f} \delta_{n_y^i n_y^f} \frac{n_z^i n_z^f}{(n_z^i)^2 - (n_z^f)^2}.$$

All selection rules are included in Eqs. (6a) and (6b).

For the quantum well surrounding the dot, the only non-zero matrix element is

$$P_{k_x, k_y, n, k_x', k_y', m}^z = \begin{cases} 4i\epsilon_z \frac{\hbar}{d} \delta_{k_x k_x'} \delta_{k_y k_y'} \frac{mn}{m^2 - n^2} & \text{for } (m - n) \text{ odd} \\ 0 & \text{for } (m - n) \text{ even} \end{cases}. \quad (7)$$

III. NUMERICAL RESULTS AND DISCUSSION

A. Electronic structure

The electronic structure of quantum rods was calculated using the 8-band $k \cdot p$ envelope function model. The rod material composition and geometric parameters were taken in accordance with the literature data. The rod diameter was taken to be 10 nm,¹ and the rod height was varied from 2.5 nm to 60 nm, which covers the typical range of quantum rod heights.^{1,2} The InAs/GaAs short-period superlattice, away from the quantum rod, transforms into an InGaAs alloy quantum well layer with In content of 16%¹ during the structure growth. The In content in the rod is approximately 45%.¹ The profile of the cylindrically symmetric structure in the $z-r$ plane is schematically shown in the inset of Fig. 1, and the conduction band edge profile in the growth direction for $r = 0$ (which includes the hydrostatic strain-induced shift) is shown in Fig. 1. The structure can be considered as a quantum well with the z axis as the growth direction and with the potential getting deeper in the radial direction, up to the rod radius of $r = 5$ nm.

The electronic structure of 60-nm- and 10-nm-high rods is displayed in Fig. 2, together with the wavefunction moduli squared for a number of relevant states. The electronic states can be classified as either free or non-free, according to whether their energies are above or below the barrier in the growth direction.

Numerical calculations were performed in the subspace defined by basis functions corresponding to the closed box around the whole structure, and these solutions make a discrete set. For quasi-bound and free states, this description is clearly only approximate, but one can still expect that such discretisation, in fact, samples the continuum (including the resonances) of the open system and should be able to capture the variation of optical transition matrix elements with the transition energy. All non-free states can be further divided into three subgroups. The first subgroup, labeled with A in Fig. 2, includes states completely localized in the dot, which exist only due to the dot. Their total energies do not have to be lower than the barrier in the radial direction, as is the case, e.g., for state A_4 for the 60-nm-high rod or state A_2 for

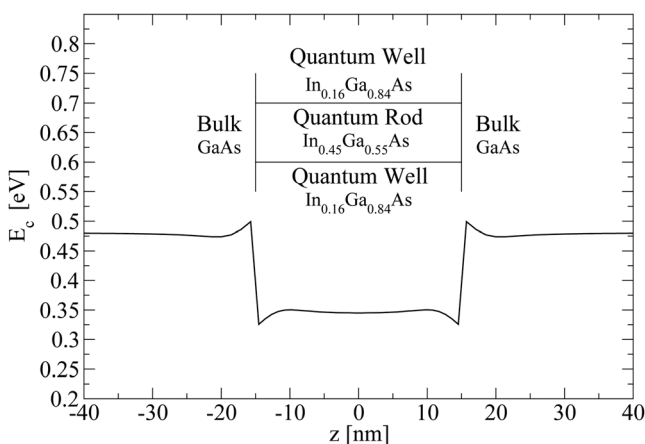


FIG. 1. The conduction band profile, including the hydrostatic strain potential, for a 30-nm-tall quantum rod. The structure layout in the $z-r$ plane is shown in the inset.

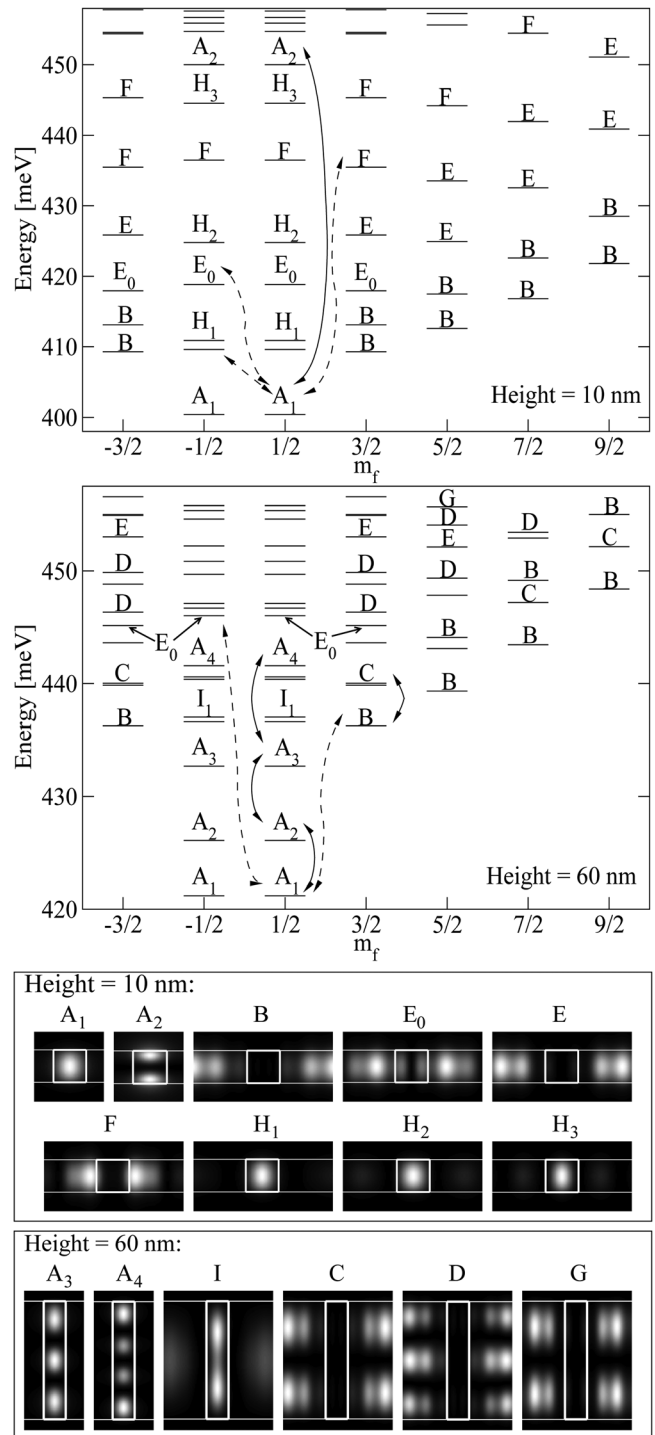


FIG. 2. Energy diagrams for quantum rods with 10 nm height (upper) and 60 nm height (the lower diagram). Different types of states have different (but height-independent) labels. The lower part of the figure shows various types of states (wavefunction structures) appearing in the quantum rods. Solid (dashed) double-headed lines indicate the dominant transitions for the z -(in-plane) polarized radiation.

the 10-nm-high rod (a part of their energy comes from quantisation in the z -direction). Since the In content-related barrier in the radial direction is about 30% lower than in the growth direction, these states behave like bound states in an infinite dot, described by Eq. (2). Increasing n_z increases the number of nodes in the growth direction. The quantum number m_f plays a role similar to quantum numbers n_x and n_y .

According to Eqs. (6a), (6b), and (7), only the transitions between the bound dot states, i.e., from (the only significantly populated) $m_f = \frac{1}{2}$ and $m_f = -\frac{1}{2}$ into higher states (observing the selection rules), can significantly contribute to absorption of radially polarized radiation. Dot states with higher values of m_f are absent.

Within the simple effective-mass model, those states would be described by the quantum numbers $n_x = 1$ and $n_y = 1$. For taller rods, the energy difference between these bound states decreases (Eq. (3)). This can be also seen from Fig. 2, where states A_1 , A_2 , and A_3 in 60-nm-high rods have energies lower than the radial barrier, but in the 10-nm-high rod, the p -like bound state A_2 is far above the s -like A_1 , with energy higher than the radial barrier. This is a very interesting feature. State A_2 is bound, although its energy is in the subband continuum. This indicates that an electron optically excited into A_2 state might be efficiently extracted by a lateral electric field, which will be discussed later on. The third state, A_3 , does not exist in the 10-nm-high rod, since the number of bound states in the well and the dot is reduced by decreasing the height of the dot, i.e., by decreasing the well width.

The second subgroup of non-free states appears for energies higher than the radial barrier, and these states are completely localized outside the rod. Their properties are determined by the well and will be hereafter called well states. These states are, actually, quantum well bound states behaving like plane waves in the radial direction and can be classified into subbands according to Eq. (4) and Eq. (5). Among the well states, one can recognize states from the same subband, because they look similarly, i.e., have the same number of nodes in the growth direction and similar wave-like behavior in the radial direction. Therefore, B, C, and D in Fig. 2 denote the 1st, 2nd, and 3rd subband in the growth direction. All these states behave like plane waves in the radial direction. Figure 2 shows that increasing the quantum number m_f gives states lined up along a parabolic “subband”. This is fully analogous to the wave in the radial (x or y) direction and its parabolic dispersion with k_x and k_y in a simple infinitely deep well.

The same as for the dot states, the energy difference between quantum well states within different subbands, but with the same m_f , decreases as the rod height increases (Eq. (5)). There are also a larger number of subbands in the well, causing complicated state ordering for taller rods. The density of states increases, leading to interlacing of states from different subbands (Fig. 2).

The third subgroup of non-free states, denoted as mixed states, are those which are only partially localized in the dot. For example, one of those states is labeled as the E_0 -state in Fig. 2. These largely delocalised states are denoted as E, F, and G and also form bands in the same way as B, C, and D states do, but their behavior in the radial direction is different. States E, F, and G are not homogeneous waves in the radial direction, although they are not localized either. Furthermore, their energy depends only mildly on the quantum rod and quantum well parameters. The state E_0 behaves as the ground state for the quasi-subband E. We also note that states F_0 and G_0 , as ground states for subbands F and G, could be added on the diagram, but they are not labeled in Fig. 2, since their exact nature is less clear.

There also exist non-free states labeled as H for the 10-nm-high rod and as I for the 60-nm-high rod in Fig. 2. Those states are partially localized outside the rod, but their shape is still largely influenced by the rod. Some of those states have no nodes in the growth direction, like H states, or one node, like I states, which indicates the order of their quantization. It is difficult to find a precise qualitative description or unambiguous classification of these states.

To conclude, by varying the height of the quantum rod structure, one can tune the energy spacing between various bound states. The spacing between consecutive dot bound states decreases with increasing the rod height. The same applies to the spacing between consecutive well states with the same m_f , but from different subbands. All that affects the ordering of states and enables tunability of absorption spectra for light polarized in the growth direction.

B. Intraband absorption spectra

All intra-subband transitions for in-plane, i.e., radially polarized radiation are forbidden (see Eq. (7)). From Eqs. (6a), (6b), and (7), it is clear that the momentum matrix elements depend only on the size of the structure in the direction of the light polarization, which, within the range of structures considered here, means that the absorption of z -polarized radiation will vary.

The lowest bound dot state is the ground state of the system and, except in the case of very long rods (e.g., 60 nm), the next couple of states belong to the first well subband, which can accommodate a number of electrons, due to their continuous nature. Assuming that the number of electrons per rod is small enough that only the ground dot state and the lowest subband states are significantly populated, the Fermi level is very close to the first subband minimum and the transitions from these states will give the major contribution to the total absorption.

What matters for a good photodetector performance are the transitions from the populated initial states to low-lying free states (resonances), because electrons in the latter can efficiently contribute to the current if the structure is biased. Yet, the cross-sections of these transitions may be very small compared to those for bound-to-bound transitions, according to Eq. (1), and this issue has to be investigated separately.

1. Absorption of z -polarized radiation

The absorption is strong only for transitions between opposite parity states, as is clear from the simple effective mass model (Eqs. (6b) and (7)). For example, according to Eq. (6b), one expects that the dominant matrix element for z -polarized radiation will be between the ground state with $n_x^i = 1$, $n_y^i = 1$, and $n_z^i = 1$ (s -like state) and $n_x^f = 1$, $n_y^f = 1$, and $n_z^f = 2$ (the p -like, also dot state, with a good overlap with the initial state), as the calculation indeed gives. The same rule applies to transitions between the well subbands, i.e., the matrix element is large for the transition between $n = 1$ and $n = 2$ states (Eq. (7)). As shown in Fig. 2 (solid double-arrowed lines), the dominant dipole matrix elements are usually between states of type A with opposite parity, e.g., $A_1 - A_2$, and between subbands B and C or C and D.

Increasing the dot height decreases both the momentum matrix element squared and the state spacing, and the latter dependence is stronger than the former, because it acts both explicitly and via the energy-dependent linewidth, resulting in increasing cross-section. This is predicted by both the full $\mathbf{k} \cdot \mathbf{p}$ and the simple effective mass model.

At higher temperatures, transitions from higher states of the quantum dot can also significantly contribute the total absorption, as they become increasingly populated. However, the absorption peak positions hardly change, because main additional transition, which was not active at $T = 0$ K, comes from the well states, and their spacing appears to be approximately the same as for the dot states.

Taller rods have a smaller state spacing, i.e., reduced transition energies of bound-to-bound transitions. Therefore, the absorption tunability for z -polarized radiation is achieved by changing the rod height for sufficiently tall rods, accommodating both an s -like and a p -like bound state.

This explains the cross-section for taller quantum rods calculated using Eq. (1), shown in Figs. 3 and 4. At $T = 0$ K, only the transitions from the dot ground, bound state, into the higher dot bound state exist (assuming a maximum of two electrons per dot). This is why a single peak appears for any height, shifting to lower frequency as height increases. At elevated temperatures, e.g., $T = 77$ K, an additional transition occurs from the first well subband, but at similar energies as transitions from the bound state. Therefore, Figs. 3 and 4 are generally similar. However, one can see from Fig. 4 that the absorption peak for the 60-nm-high rod decreases at elevated temperature, due to thermal population of the upper state. Clearly, taller rods with their small state spacings are more strongly affected by temperature.

The most interesting feature of intraband spectrum in this case is that, for a range of values of rod height, the dominant $s - p$ -like transition excites electrons into the quantum well continuum. These electrons can be efficiently extracted by a lateral electric field, thus providing a basis for the design of a lateral-extraction photodetector. The advantage of such a photodetector would be a strong bound-to-bound absorption

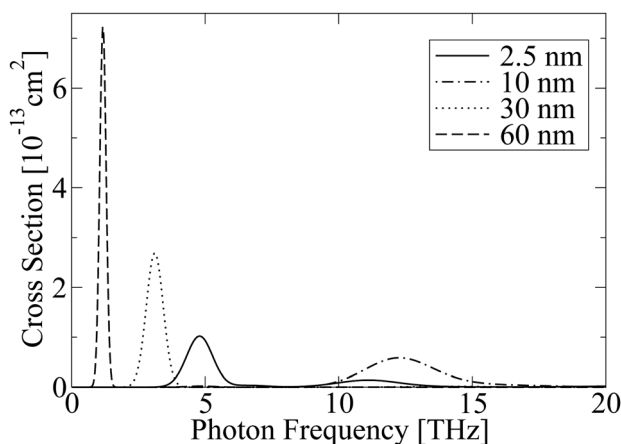


FIG. 3. Absorption cross-section for transitions from the ground state for z -polarized radiation at $T = 0$ K with one electron per rod. The absorption for the 2.5-nm-tall dot comes from the bound-to-continuum transition, since such a short dot can accommodate only one bound state. Absorption in taller rods comes from bound-to-bound transitions and follows the trend as the rod height varies.

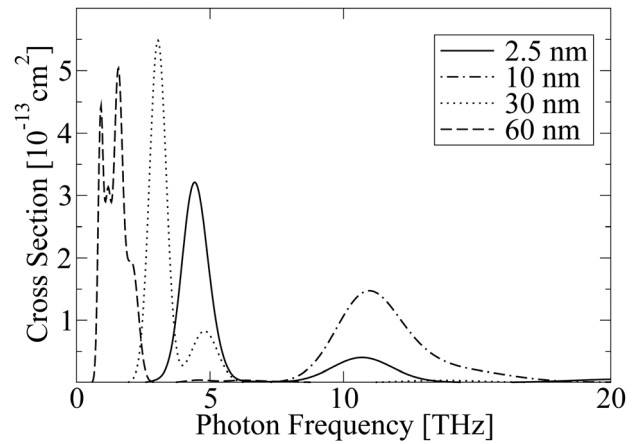


FIG. 4. Absorption cross-section for z -polarized radiation at $T = 77$ K with one electron per rod.

and an efficient continuum-like extraction of electrons. However, more detailed studies of electron transport are required before any more reliable conclusions can be made.

In the case of bound-to-continuum absorption, which can generate vertical photocurrent, the situation is quite different. Usually coming from transitions between non-subsequent states (in respect to size-quantization in the z -direction), this absorption may be quite small. The transition energy from the lowest bound to the barrier continuum state slowly decreases with increasing rod height. For larger matrix elements, one needs shorter rods, also evident from simple effective-mass model. For instance, the resonant bound-to-continuum absorption peak in the (rather flat) 2.5-nm-high quantum rod is comparable to bound-to-bound absorption. For higher rods (> 10 nm), however, bound-to-continuum absorption peaks are not observable on the same scale as bound-to-bound ones, due to the decreased values of momentum matrix elements, increased energy separation, and increased linewidth, which all lead to small absorption strength.

However, for extremely short rods, such as 2.5 nm (typical height of conventional quantum dots), the dominant transition for growth-polarized radiation is of bound-to-continuum type. These structures are not typical “rods”, and the results for them are given only for the sake of comparison between rods and conventional quantum dots.

2. Absorption of in-plane polarized radiation

The important issue in quantum well intraband photodetectors is that there is no absorption of in-plane polarized radiation, as is clear from Eq. (7). The quantum rod structure may have non-zero absorption of in-plane polarized radiation, e.g., based on transitions from the dot bound states with the quantum number $m_f = \frac{1}{2}$ into well and mixed states with $m_f = -\frac{1}{2}$.

The detailed examination of dominant optical matrix elements in the structure shows that transitions between bound states in the dot and higher well or mixed states, for the in-plane polarization, are more prominent than “intra-dot” transitions. With transitions between the subband states being forbidden, all absorption will come from transitions from the first bound state of the dot, with bound-to-bound transitions much stronger than bound-to-continuum transitions. The

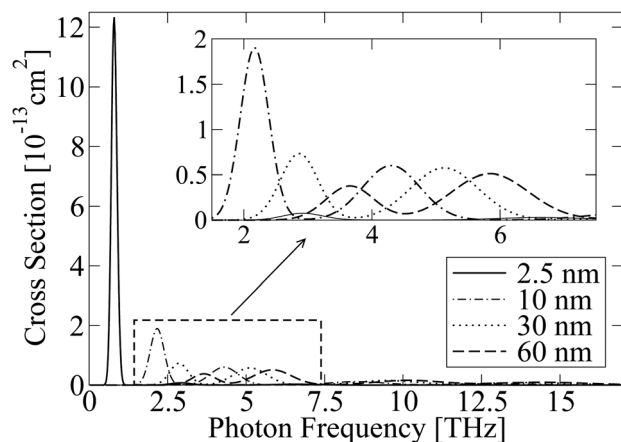


FIG. 5. Absorption cross-section for bound-to-bound transitions for in-plane polarized radiation at $T = 0$ K with one electron per rod.

bound-to-bound absorption peak can be tuned by changing the rod height, and results are shown in Fig. 5. Dominant transitions from the dot ground state are indicated with dashed double-headed lines in Fig. 2. Dominant bound-to-bound transitions in this case are transitions between A_1 and B or E_0 states.

The in-plane-polarized radiation can excite electrons into the well states. In contrast to the case of growth-polarization, the excited electrons are here already highly delocalized and easily extractable by lateral electric field. We conclude that a polarization-independent intraband lateral photodetector might be designed and optimized by a proper choice of rod height.

It is clear that the problem of small absorption strength for in-plane polarized radiation, compared to z -polarization, arises due to widely spread wavefunction of the mixed final state, which reduces the overlap with the initial dot bound state. The absorption peaks of bound-to-continuum transitions are also tunable with the rod height, same as in the case of z -polarization. Calculations show that the corresponding optical matrix elements increase with increasing dot height, in contrast to the case of z -polarization. For example, the first resonant bound-to-continuum transition in a 30-nm-high quantum rod has the transition matrix element similar to the bound-to-bound one at 3 THz, cf. Figure 5, and the situation remains like that down to the rod heights of ~ 10 nm, though not at 2.5 nm.

The opposite “direction” of the absorption peaks tunability for the two polarizations generally makes it possible to engineer the structure (find suitable rod height and diameter) so to get optimal functionality for both directions of incident radiation in the THz frequency range.

IV. CONCLUSION

In summary, a detailed strain-dependent eight-band $k \cdot p$ method was used to analyze the electronic structure and intraband optical properties of self-assembled quantum rods. It was found that their optical properties strongly depend on rod height, with an amount of tunability in terahertz frequency range, which enables engineering of these structures for optoelectronic applications. General features of the

absorption of z -polarized radiation are that it inherited properties of both an isolated quantum dot and a quantum well. The fact that p -like dot state is embedded in the well subband gives rise to the possibility of using the $s - p$ -like transitions in photodetection. The absorption of in-plane polarized radiation, which is due to electron transitions from the ground (dot-bound) state to the well states, is a benefit offered by this type of structures, in contrast to quantum wells. Such excited electrons can be efficiently extracted by lateral electric field, paving the way toward a polarization-independent lateral intraband terahertz photodetector.

ACKNOWLEDGMENTS

N.P. acknowledges the support in part by the University of Leeds Fully Funded International Research Scholarships program and in part by the Serbian Ministry of Education Scholarship program for students studying at the world’s leading universities. N.V. was supported in part by the Serbian Ministry of Science under project No. ON171017 and the European Commission under EU FP7 projects PRACE-IIP, HP-SEE, and EGI-InSPIRE. D.I., Z.I, and P.H. acknowledge support by NATO Science for Peace project EAP. SFFP 984068.

- ¹L. Li, G. Patriarche, N. Chauvin, P. Ridha, M. Rossetti, J. Andrzejewski, G. Sek, J. Misiewicz, and A. Fiore, *IEEE J. Sel. Top. Quantum Electron.* **14**, 1204 (2008).
- ²J. He, H. J. Krenner, C. Pryor, J. P. Zhang, Y. Wu, D. G. Allen, C. M. Morris, M. S. Sherwin, and P. M. Petroff, *Nano Lett.* **7**, 802 (2007).
- ³M. Motyka, G. Sek, K. Ryczko, J. Andrzejewski, J. Misiewicz, L. H. Li, A. Fiore, and G. Patriarche, *Appl. Phys. Lett.* **90**, 181933 (2007).
- ⁴P. Ridha, L. Li, A. Fiore, G. Patriarche, M. Mexis, and P. M. Smowton, *Appl. Phys. Lett.* **91**, 191123 (2007).
- ⁵D. Stehr, C. M. Morris, D. Talbayev, M. Wagner, H. C. Kim, A. J. Taylor, H. Schneider, P. M. Petroff, and M. S. Sherwin, *Appl. Phys. Lett.* **95**, 251105 (2009).
- ⁶C. M. Morris, D. Stehr, H. Kim, T.-A. Truong, C. Pryor, P. M. Petroff, and M. S. Sherwin, *Nano Lett.* **12**, 1115 (2012).
- ⁷L. H. Li, G. Patriarche, E. H. Linfield, S. P. Khanna, and A. G. Davies, *J. Appl. Phys.* **108**, 103522 (2010).
- ⁸R. Nedzinskas, B. Čechavičius, V. Karpus, J. Kavaliauskas, G. Valušis, L. H. Li, S. P. Khanna, and E. H. Linfield, *J. Appl. Phys.* **109**, 123526 (2011).
- ⁹T. Saito, H. Ebe, Y. Arakawa, T. Kakitsuka, and M. Sugawara, *Phys. Rev. B* **77**, 195318 (2008).
- ¹⁰J. Andrzejewski, G. Sęk, E. O’Reilly, A. Fiore, and J. Misiewicz, *J. Phys.: Conf. Ser.* **245**, 012038 (2010).
- ¹¹N. Prodanović, N. Vukmirović, D. Indjin, Z. Ikonić, and P. Harrison, *J. Phys.: Conf. Ser.* **242**, 012012 (2010).
- ¹²S. Hameau, J. N. Isaia, Y. Guldner, E. Deleporte, O. Verzellen, R. Ferreira, G. Bastard, J. Zeman, and J. M. Gérard, *Phys. Rev. B* **65**, 085316 (2002).
- ¹³T. B. Bahder, *Phys. Rev. B* **41**, 11992 (1990).
- ¹⁴S. Tomić, A. G. Sunderland, and I. J. Bush, *J. Mater. Chem.* **16**, 1963 (2006).
- ¹⁵N. Vukmirović, D. Indjin, V. D. Jovanović, Z. Ikonić, and P. Harrison, *Phys. Rev. B* **72**, 075356 (2005).
- ¹⁶V. Mlinar, M. Tadić, B. Partoens, and F. M. Peeters, *Phys. Rev. B* **71**, 205305 (2005).
- ¹⁷C. Pryor, *Phys. Rev. B* **57**, 7190 (1998).
- ¹⁸O. Stier, M. Grundmann, and D. Bimberg, *Phys. Rev. B* **59**, 5688 (1999).
- ¹⁹A. J. Davies, *The Finite Element Method* (Clarendon, Oxford, 1980).
- ²⁰H. Krenner, C. Pryor, J. He, J. Zhang, Y. Wu, C. Morris, M. Sherwin, and P. Petroff, *Physica E (Amsterdam)* **40**, 1785 (2008).
- ²¹N. Vukmirović, Ž. Gačević, Z. Ikonić, D. Indjin, P. Harrison, and V. Milanović, *Semicond. Sci. Technol.* **21**, 1098 (2006).
- ²²N. Vukmirović, D. Indjin, Z. Ikonić, and P. Harrison, *Appl. Phys. Lett.* **88**, 251107 (2006).

Optimization of InAs/AlInAs quantum wells based up-converter for silicon solar cells

Nikola Prodanović, Jelena Radovanović, Vitomir Milanović, and Stanko Tomić

Citation: *J. Appl. Phys.* **110**, 063713 (2011); doi: 10.1063/1.3641977

View online: <http://dx.doi.org/10.1063/1.3641977>

View Table of Contents: <http://jap.aip.org/resource/1/JAPIAU/v110/i6>

Published by the AIP Publishing LLC.

Additional information on J. Appl. Phys.

Journal Homepage: <http://jap.aip.org/>

Journal Information: http://jap.aip.org/about/about_the_journal

Top downloads: http://jap.aip.org/features/most_downloaded

Information for Authors: <http://jap.aip.org/authors>

ADVERTISEMENT



AIPAdvances

Now Indexed in Thomson Reuters Databases

Explore AIP's open access journal:

- Rapid publication
- Article-level metrics
- Post-publication rating and commenting

Optimization of InAs/AlInAs quantum wells based up-converter for silicon solar cells

Nikola Prodanović,¹ Jelena Radovanović,^{2,a)} Vitomir Milanović,² and Stanko Tomić³

¹*School of Electronic and Electrical Engineering, University of Leeds, Woodhouse Lane, Leeds LS2 9JT, United Kingdom*

²*School of Electrical Engineering, University of Belgrade, Bulevar kralja Aleksandra 73, 11120 Belgrade, Serbia*

³*Joule Physics Laboratory, School of Computing, Science and Engineering, University of Salford, Salford M5 4WT, United Kingdom*

(Received 7 June 2011; accepted 15 August 2011; published online 23 September 2011)

We present an optimization procedure for the design of InAs/AlInAs quantum well (QW) based up-converter for silicon solar cells. By utilizing nonlinear optical effects in QW structures, the up-conversion of low energy photons for which the silicon (Si) is transparent, into higher energy photons that can be absorbed by a Si solar cell, is achieved. Due to lack of the III-V material combinations that can provide a large enough conduction band offset to accommodate three bound states required for the optimal operation, we explore the possibilities of using continuum part of the spectrum as the third state. Optimization of the up-converter is performed by maximization of the second order susceptibility derived from the density matrix formalism. Our procedure is based on use of the genetic algorithm global optimization tool, as a “driver” routine for the eight-band $\mathbf{k} \cdot \mathbf{p}$ Hamiltonian “solver” of the QW electronic structure problem. © 2011 American Institute of Physics. [doi:10.1063/1.3641977]

I. INTRODUCTION

One of the major obstacles for high power conversion efficiency of the sun light with conventional semiconductor materials is that only photons with energies close to that of the semiconductor energy gap (E_g) are effectively converted into electron-hole pairs. Photons with energy lower than E_g are simply lost (the semiconductor is transparent to them) and of photons with higher energy ($> E_g$), only a part, i.e., those with energy almost equal to E_g are best suited for absorption. The majority of high energy electrons generated by photons with $> E_g$, (hot carriers) decay fast thermally to the conduction band Fermi level before they can contribute to the output current. The principal aim here must be to make a better use of the solar spectrum.^{1–7} One of the promising concepts is to place another device, a “light converter,” attached to the rear (front) of an existing solar cell (SC), to capture photons with energy below (above) the energy gap of SC and re-emit them at the higher (lower) energy to match the region where SC exhibits a very good spectral response. Thus it is possible to enhance the conversion efficiency of the SC device.^{8–11} Up or down conversion can occur in a three-level quantum mechanical systems in a manner that luminescent materials convert photons by utilizing nonlinear optical effects.

In this paper, we propose utilization of the quantum well structure, optimized with respect to its nonlinear susceptibility, as a luminescent material. For a three level system, the difference between the highest and the lowest bound state has to be approximately the same as the SC (in our case Si) energy gap.

A detailed examination of the literature^{12–14} proved that it was almost impossible to find well/barrier material combination among conventional III-V binaries and their alloys; which can provide for deep enough conduction band offset to accommodate at least three bound states, sufficiently spaced for 1.12 eV (Si energy gap) conversion. The main obstacle here was the appearance of indirect bands (originating from X or L states) in the barrier materials beyond certain Al concentration in Al containing ternaries. Therefore, the continual part of the spectrum has to be used instead as the third state. We have chosen $\text{Al}_{0.6}\text{In}_{0.4}\text{As}$ as a barrier and InAs as a well material for the design of the optical up-converter. Optimization of the QW based up-converter is performed by using the genetic algorithm (GA) as a global optimization tool,^{15–18} to maximize the second order nonlinear susceptibility by varying the QW structural parameters. The quantum well electronic states, wavefunctions, and optical dipole matrix elements needed to determine the nonlinear susceptibility were calculated from the eight-band $\mathbf{k} \cdot \mathbf{p}$ model that takes into account conduction to valence band band mixing as well as the effect of strain.

II. THEORETICAL CONSIDERATIONS

A. Genetic algorithm

Owing to the complexity of the target function of an up-converter, it would be very difficult to find its global maximum within given multidimensional domain by using classical optimization algorithms like downhill simplex or conjugate gradients¹⁹ or specialized methods²⁰ including isospectral transformations of the Hamiltonian.^{21–23} Therefore we formulate our method using the global optimization tool based on the genetic algorithm (GA).²⁴ Genetic algorithm is

^{a)}Author to whom correspondence should be addressed. Electronic-mail: radovanovic@ef.bg.ac.rs.

a global optimization search engine for the maximization of scalar functions, $f(x_1, x_1, \dots, x_n)$, of real vector arguments, (x_1, \dots, x_n) , where n is the number of independent parameters. The optimization mechanism behind the genetic algorithm can be understood analogously to the evolution of a biological system, i.e., a population of individuals. In such a system, evolution is interpreted as an optimization of certain fitness properties of the population.

In GA, the population is represented by a set of points $(x_1^i, x_1^i, \dots, x_n^i)$, in the parameter space, where $i = 1 \dots n_p$ and n_p is the population size. The algorithm starts from an initial population that is randomly chosen. The average value of the fitness (target) function in the initial population (for the initial set of parameters) can be very small, but it is expected to reach an optimal value through the evolutionary process (optimization). Starting from this initial population, the algorithm produces a new generation (“siblings”) in every subsequent iteration through the process of reproduction. Reproduction entails selection of two parents from a previous generation, and this is done stochastically, with probability proportional to the fitness, i.e., target value of the individuals in the old generation. The number of iterations in the GA can be fixed and should be set to a high enough value so that the algorithm may reach a predefined convergence criteria before termination.

B. Electronic structure model

To calculate the electronic structure of the up-converter, we have used the 8-band $\mathbf{k} \cdot \mathbf{p}$ Hamiltonian,²⁵ which at $k_{\parallel} = 0$ can be reduced to:

$$H = \begin{pmatrix} G & 0 \\ 0 & G \end{pmatrix} \quad (1)$$

with

$$G = \begin{pmatrix} E_{cb}(z) & 0 & \sqrt{2}\hat{U} & -\hat{U} \\ 0 & E_{hh}(z) & 0 & 0 \\ \sqrt{2}\hat{U}^\dagger & 0 & E_{lh}(z) & Q(z) \\ -\hat{U}^\dagger & 0 & Q^\dagger(z) & E_{so}(z) \end{pmatrix}$$

and

$$\hat{U} = \frac{\hbar}{\sqrt{6m_0}} \sqrt{E_p} \frac{d}{dz} \quad (2)$$

$$Q(z) = -\sqrt{2}\zeta(z) \quad (3)$$

$$E_{cb}(z) = E_{c0} + 2a_c(z) \left[1 - \frac{c_{12}(z)}{c_{11}(z)} \right] \varepsilon_{xx}(z) \quad (4)$$

$$E_{lh/hh}(z) = E_{v0} + 2a_v(z) \left[1 - \frac{c_{12}(z)}{c_{11}(z)} \right] \varepsilon_{xx}(z) \pm \zeta(z) \quad (5)$$

$$E_{so}(z) = E_{v0} - \Delta_{so}(z), \quad (6)$$

where $\zeta(z) = -b_{ax}(z)[1 - c_{12}(z)/c_{11}(z)]\varepsilon_{xx}$ is the shear strain, E_{c0} and E_{v0} represent the bottom of the conduction band and the top of the valence band of the unstrained bulk material, respectively, and m_0 is the free electron mass. Furthermore, E_p is the Kane energy, which is assumed to be z -independent and to take an average value throughout the structure, Δ_{so} is the spin-orbit splitting energy, b_{ax} is the axial deformation potential, and a_c and a_v are the hydrostatic deformation potentials for conduction and valence band, respectively. Finally, c_{11} and c_{12} stand for the elastic constants of the crystals that constitute the structure, while $\varepsilon_{xx} = (a_b - a_w)/a_w$ is the relative change in the lattice constants at the barrier-well interface, with a_b and a_w being the lattice constants of the bulk barrier and well material. The solution of the Hamiltonian eigenvalue problem:

$$\begin{pmatrix} E_{cb} & 0 & \sqrt{2}U & -U \\ 0 & E_{hh} & 0 & 0 \\ \sqrt{2}U^\dagger & 0 & E_{lh} & Q \\ -U^\dagger & 0 & Q^\dagger & E_{so} \end{pmatrix} \begin{pmatrix} \phi_c \\ \phi_{hh} \\ \phi_{lh} \\ \phi_{so} \end{pmatrix} = E \begin{pmatrix} \phi_c \\ \phi_{hh} \\ \phi_{lh} \\ \phi_{so} \end{pmatrix}, \quad (7)$$

can be found in an analytic form for a layered structure. From Eq. (7), we obtain a Schrödinger like equation for $\phi_c(z)$

$$-\frac{\hbar^2}{2} \frac{d}{dz} \frac{1}{m^*(E, z)} \frac{d}{dz} \phi_c(z) + E_{cb}(z) \phi_c(z) = E \phi_c(z), \quad (8)$$

with

$$m^*(E, z) = 3m_0^*(z)m_0 \times \frac{[E - E_{lh}(z)][E - E_{so}(z)] - 2\zeta^2(z)}{E_g(z)\{2[E - E_{so}(z) + 2\zeta(z)] + [E - E_{lh}(z)]\}} \quad (9)$$

where $E_g(z) = E_{c0}(z) - E_{v0}(z)$, while $m_0^*(z) = E_g(z)/E_p$ is the parabolic effective mass given in Table I. If $\zeta = 0$, $a_b = a_w$ and $E_{so} = E_{lh}$, then Eq. (9) reduces to the well-known expression for nonparabolic effective mass (Ref. 26): $m^*(E, z) = m_0^*(z)m_0 [1 + (E - E_{c0}(z))/E_g(z)]$.

TABLE I. The properties of AlAs and InAs used in calculations of layer parameters and electronic structure of the convertor (Refs. 12 and 13). VBO is the top of the valence band within the scale where VBO of InSb is set to zero.

	AlAs	InAs
a_0 [nm]	0.56611	0.60583
m_0^* [m_0]	0.15	0.026
E_g [eV]	3.01	0.359
E_p [eV]	21.1	21.5
VBO [eV]	-1.33	-0.59
Δ_{so} [eV]	0.28	0.39
a_c [eV]	-5.64	-5.08
a_v [eV]	-2.47	-1
b_{ax} [eV]	-2.3	-1.8
c_{11} [GPa]	1250	832.9
c_{12} [GPa]	534.1	452.6

The other envelope function components can be obtained from the solution of Eq. (8) as:

$$\phi_{lh}(z) = \frac{\sqrt{2}[E_{so}(z) - E] - \sqrt{2}\zeta(z)}{[E_{lh}(z) - E][E_{so}(z) - E] - 2\zeta^2(z)} \hat{U}\phi_c(z) \quad (10)$$

$$\phi_{so}(z) = -\frac{[E_{lh}(z) - E] - 2\zeta(z)}{[E_{lh}(z) - E][E_{so}(z) - E] - 2\zeta^2(z)} \hat{U}\phi_c(z), \quad (11)$$

and $\phi_{hh}(z)$ is decoupled at $k_{\parallel} = 0$.

It has been shown in Ref. 27 that the normalization condition for the i th state is given as:

$$1 = \langle \phi_{c,i} | \phi_{c,i} \rangle + \langle \phi_{so,i} | \phi_{so,i} \rangle + \langle \phi_{lh,i} | \phi_{lh,i} \rangle \quad (12)$$

and the dipole matrix elements read

$$\langle \psi_i | Z | \psi_j \rangle = \langle \phi_{c,i} | z | \phi_{c,j} \rangle + \langle \phi_{so,i} | z | \phi_{so,j} \rangle + \langle \phi_{lh,i} | z | \phi_{lh,j} \rangle \quad (13)$$

where ψ_i and ψ_j are i th and j th eigenstate of the 8-band Hamiltonian with components $\phi_{c,i}$, $\phi_{so,i}$, $\phi_{lh,i}$ and $\phi_{c,j}$, $\phi_{so,j}$, $\phi_{lh,j}$, respectively, and Z is the z coordinate operator represented as $Z = z|I|$ (I is the 3×3 unity operator).

All the equations in this section are derived for $k_{\parallel} = 0$, hence Eq. (9) is used to describe the effective mass $m^*(E, z)$, which includes the nonparabolic correction in addition to the conduction band-edge mass $m_0^*(z)m_0$. Among the quantities needed for evaluating the nonlinear optical susceptibility $\chi_{zzz}^{(2)}$, which is the main goal of this work, are the diagonal matrix elements ρ_{ll}^0 of the density matrix of the unperturbed system as described in the next section. These matrix elements may be found from 8×8 Hamiltonian for all $k_{\parallel} \neq 0$ via an extremely complex procedure. Therefore we have used two standard approximations: first, that the dependence of dipole matrix elements on k_{\parallel} is very weak, so that we may consequently use their $k_{\parallel} = 0$ values, and second, that $\rho_{ll}^0 = 1$ for $l = 1$, otherwise $\rho_{ll}^0 = 0$. In this case, it is sufficient to analyze the 8×8 Hamiltonian for $k_{\parallel} = 0$ only.

C. The target function model

If we expose an electronic system such as the optical converter to the incident radiation with electric field $\mathbf{E}(\mathbf{r}, t)$, then the response can be quantified via global polarization $\mathbf{P}(\mathbf{r}, t)$ of the system. Consequently, we define the linear susceptibility χ (the first term in the response expansion) and the tensor of nonlinear susceptibility χ_{ijk} (the second term in the response expansion) through the relation:

$$P_i = \chi E_i + \sum_{j,k} \chi_{ijk} E_j E_k. \quad (14)$$

Our aim here is to derive an expression for the polarization of electronic system, which depends on quadratic terms of the electric field, starting from the calculated electronic structure of the optical converter. Then it would be possible to obtain the second order susceptibility from such expres-

sion as a target function that will be used in the optimization process.

We use the density matrix formalism to describe the electronic system of the optical converter.²⁸ The electric field of the incident radiation is treated as a perturbation that excites the electrons to higher states of our QW structure. New collective electron state is described by the density matrix whose matrix elements are calculated using the perturbation theory. The susceptibility tensor then reads (Ref. 28):

$$\begin{aligned} \chi_{ijk}^{(2)}(E_p, E_q, E_p + E_q) = & -\frac{e^3 \bar{\rho}}{2} \sum_{lmn} \rho_{ll}^0 \\ & \times \left\{ \frac{r_{ln}^i r_{nm}^j r_{ml}^k}{[(E_{nl} - E_p - E_q) - i\Gamma_{nl}][(E_{ml} - E_p) - i\Gamma_{ml}]} \right. \\ & + \frac{r_{ln}^i r_{nm}^k r_{ml}^j}{[(E_{nl} - E_p - E_q) - i\Gamma_{nl}][(E_{ml} - E_q) - i\Gamma_{ml}]} \\ & + \frac{r_{ln}^k r_{nm}^i r_{ml}^j}{[(E_{mn} - E_p - E_q) - i\Gamma_{mn}][(E_{nl} + E_p) + i\Gamma_{nl}]} \\ & + \frac{r_{ln}^j r_{nm}^i r_{ml}^k}{[(E_{mn} - E_p - E_q) - i\Gamma_{mn}][(E_{nl} + E_q) + i\Gamma_{nl}]} \\ & + \frac{r_{ln}^j r_{nm}^i r_{ml}^k}{[(E_{nm} + E_p + E_q) + i\Gamma_{nm}][(E_{ml} - E_p) - i\Gamma_{ml}]} \\ & + \frac{r_{ln}^k r_{nm}^i r_{ml}^j}{[(E_{nm} + E_p + E_q) + i\Gamma_{nm}][(E_{ml} - E_q) - i\Gamma_{ml}]} \\ & + \frac{r_{ln}^k r_{nm}^j r_{ml}^i}{[(E_{ml} + E_p + E_q) + i\Gamma_{ml}][(E_{nl} + E_p) + i\Gamma_{nl}]} \\ & \left. + \frac{r_{ln}^j r_{nm}^k r_{ml}^i}{[(E_{ml} + E_p + E_q) + i\Gamma_{ml}][(E_{nl} + E_q) + i\Gamma_{nl}]} \right\} \quad (15) \end{aligned}$$

where cartesian indexes i, j, k are to be permuted as described in Ref. 28 (it should also be noted that the z component of the dipole matrix element is significantly larger than x and y components²⁹), $\bar{\rho}$ is the mean value of the electron density in the structure, ρ_{ll}^0 is the diagonal matrix element of the density matrix of the unperturbed system, r_{ln}^i is the i th component of the matrix element between states l and n , E_{nl} is the energy difference between states n and l , $E_{nl} = E_n - E_l$, Γ_{nl} is the relaxation factor between states n and l , while E_p and E_q are the relevant photon energies of radiation involved in the nonlinear effect.

Let us consider the QW up-converter with two bound states: E_1 and E_2 . The energy of the first of two incident photons, E_p , that take part in the nonlinear effect, has to match the energy difference between these two bound states to excite electrons from the first to the second bound state, $E_p = E_2 - E_1$. Furthermore, as a third state involved in the nonlinear process in Eq. (15), we have to choose a state in the continuum, E_r , because we could not find any suitable material combination among III-V binaries to support all bound states. This continuum state is taken as a minimal energy that still satisfies the transparency condition $T(E) = 1$. The relaxation of an electron from E_r to the ground state, E_1 , needs to produce a photon with the energy that matches the energy of the silicon SC bandgap, i.e.,

$E_r = E_g^{Si} + E_1$. At the same time, the second incident photon, E_q , needs to excite the electron from the second bound state to E_r , i.e., $E_q = E_r - E_2$. We assume that almost all electrons in the conduction band of the converter are in the ground bound state prior to exposing the converter to the incident radiation. It is reasonable to expect that such population can be obtained by adequate doping of the structure, while still having enough electrons for optical effects to be observable. Hence, $\rho_{ll}^0 = 1$ for $l = 1$ and $\rho_{ll}^0 = 0$ for $l \neq 1$ so that the summation in Eq. (15) over l vanishes and $l = 1$. The coordinate matrix element for transitions between continuous states may be neglected; this implies that the summation over m in Eq. (15) vanishes as well and $m = 2$. The relaxation parameters Γ_{nm} between states n and m are taken to be the same for all bound to continuum state transitions and are labeled with Γ_{c1} , while parameters for bound to bound state transitions are labeled with Γ_{21} . It can also be shown that the dominant term of Eq. (15) is:

$$\begin{aligned} \chi_{zzz}^{(2)}(E_p, E_q, E_p + E_q) = & -\frac{e^3 \tilde{\rho}}{2} \sum_{n>2} z_{1n} z_{n2} z_{21} \\ & \times \left\{ \left[\frac{1}{(E_{n1} - E_p - E_q) - i\Gamma_{c1}} + \frac{1}{(E_{n2} + E_p + E_q) + i\Gamma_{c1}} \right] \right. \\ & \times \left[\frac{1}{(E_{21} - E_p) - i\Gamma_{21}} + \frac{1}{(E_{21} - E_q) - i\Gamma_{21}} \right] \\ & + \left[\frac{1}{(E_{2n} - E_p - E_q) - i\Gamma_{2n}} + \frac{1}{(E_{21} + E_p + E_q) + i\Gamma_{21}} \right] \\ & \left. \times \left[\frac{1}{(E_{n1} + E_p) + i\Gamma_{c1}} + \frac{1}{(E_{n1} + E_q) + i\Gamma_{c1}} \right] \right\} \quad (16) \end{aligned}$$

where $z_{nm} = r_{nm}^z$, is the z component of the dipole matrix element. Because $E_{2n} < 0$, $E_{21} > 0$, and $E_{n1} > 0$, the second term in Eq. (16) can be neglected because it is far from the resonance. Also, the term $[(E_{n2} + E_p + E_q) + i\Gamma_{c1}]^{-1}$ is much smaller than $[(E_{n1} - E_p - E_q) - i\Gamma_{c1}]^{-1}$ and can be neglected too. The polarization and the electric field vectors are real quantities that imply that nonlinear susceptibility also has to be a real quantity. Therefore only the real part of Eq. (16) has to be evaluated. By taking all the previous considerations into account we obtain:

$$\begin{aligned} \chi_{zzz}^{(2)}(E_p, E_q, E_p + E_q) = & \frac{e^3 \tilde{\rho} z_{21}}{2} \sum_{n>2} z_{1n} z_{n2} \\ & \times \left\{ \frac{\Gamma_{c1}[(E_p - E_q)^2 + 2\Gamma_{21}^2] - \Gamma_{21}(E_p - E_q)(E_{n1} - E_p - E_q)}{\Gamma_{21}[(E_{n1} - E_p - E_q)^2 + \Gamma_{c1}^2][(E_p - E_q)^2 + \Gamma_{21}^2]} \right\} \quad (17) \end{aligned}$$

Because our up-converter design is limited by having only two bound states, the remaining sum over the continuum states index n can be transformed into integration: $\sum_n \rightarrow (L_z/2\pi) \int dk_z$, where L_z is the length of the structure. By using the relation $E(k_{||} = 0) = \hbar^2 k_{zb}^2 / 2m_b^*(E) + U_b$, the integration in k space can be transformed into integration over energies of the degenerate continuum states. Here, subscript b denotes the barrier layer and U_b is the conduction

band offset between the barrier and the well material. The final expression for the second order susceptibility, to be used as the target function in GA, reads:

$$\chi_{zzz}^{(2)}(E_p, E_q, E_p + E_q) = \left| \frac{e^3 \tilde{\rho}}{\sqrt{2\pi\hbar}} z_{21} \int_{U_b}^{\infty} D(E) dE \right| \quad (18)$$

where

$$\begin{aligned} D(E) = & \frac{\left[\frac{1}{2} \left(\frac{\Delta E}{\Gamma_{21}} \right)^2 + 1 \right] - \frac{1}{2} \left(\frac{\Delta E}{\Gamma_{21}} \right) \frac{E - E_r}{\Gamma_{c1}}}{\Gamma_{21} \left[\left(\frac{\Delta E}{\Gamma_{21}} \right)^2 + 1 \right]} \\ & \times \Lambda(E) \Theta(E) \frac{(E - U_b) \frac{dm_b^*(E)}{dE} + m_b^*(E)}{\sqrt{m_b^*(E)(E - U_b)}} \quad (19) \end{aligned}$$

and

$$\Lambda(E) = \tilde{z}_{1E_a} \tilde{z}_{2E_a} + \tilde{z}_{1E_b} \tilde{z}_{2E_b} \quad (20)$$

$$\Theta(E) = \frac{\Gamma_{c1}}{(E - E_r)^2 + \Gamma_{c1}^2}, \quad (21)$$

$$\Delta E = E_p - E_q \quad (22)$$

Here, E_a , E_b are the two orthogonal continuum double degenerate states with energy E . To prevent singularities in the limit $L_z \rightarrow \infty$, we introduce notation $\tilde{z}_{2E_{a,b}} = z_{2E_{a,b}} \sqrt{L_z}$ that allows for the factor L_z , arising from the density of continuum states, to be canceled out with the squared normalization factor of the continuum states L_z^{-1} originating from the expression for $\Lambda(E)$. One must also indicate that the function $\Lambda(E)$ does not depend on the selection of the basis states in the double degenerate subspace of the eigenvalue E with indices a and b .

We must also point out that many body effect have been neglected in our model, so $\chi_{zzz}^{(2)}$ has a linear dependence on the carrier density $\tilde{\rho}$. This approximation is valid for very low carrier densities (implicitly assumed here). For that reason, the numerical results are presented for the quantity $\chi_{zzz}^{(2)}/\tilde{\rho}$, seemingly independent of $\tilde{\rho}$. For higher values of $\tilde{\rho}$, the problem should be analyzed by using many body theory, as described in detail in Refs. 30–33. Certainly, the calculated results would quantitatively differ in that case in accordance with the increase of carrier densities. The exact determination of $\chi_{zzz}^{(2)}$ in the presence of many body effects will be presented elsewhere.

III. RESULTS AND DISCUSSION

A. Optimization of the QW based up-converter structures

To find the optimal QW up-converter design, we have examined two types of QW structures. The first type is a layered structure where the Al content is varied independently in all the layers except the first one (which forms the deepest part of QW and is made of pure InAs). In each subsequent optimization, the number of layers was increased to 2, 3, ...,

and overall improvement in the target susceptibility function was monitored. Those wells will further be referred to as the “one-step QW” for two layers, “two-steps QW” for three layers, and so on. The second type of QW structures is also layered but made of two materials only, $\text{Al}_{0.6}\text{In}_{0.4}\text{As}$ as the barrier and InAs as the well material. These structures will be labeled as a “double QW,” “triple QW,” etc.

For every compound layer, the material parameters to be used in Eq. (7) are obtained by linear interpolation of relevant AlAs and InAs data listed in Table I.^{12,13} The relaxation parameter between the bound states is assumed to be $\Gamma_{12} = 0.005$ eV, and all the relaxation parameters between continuum and bound states are taken as $\Gamma_{c1} = 0.02$ eV. In general, the values of relaxation parameters $\Gamma_{m,n}$ depend on the structural profile, carrier density, and temperature, as specified in Ref. 34 and may vary significantly (see Fig. 6 therein). The same is to be expected for the structure analyzed in this work. However, for transitions between two bound states (1 and 2), we have settled on the typical estimate of 5 meV used in the literature. For bound-continuum transitions, the linewidths $\Gamma_{c1}(k_z)$ and $\Gamma_{c2}(k_z)$ are assumed equal and amount to 20 meV, which is significantly larger than Γ_{12} , to account for the dominant effect of transmission peak width $T(k_z)$ on line broadening. The exact approach given in Ref. 34 would undoubtedly yield different and more precise values of parameters $\Gamma_{m,n}$, dependent on the wave-vector component k_z , nonetheless, the theory presented in this work could straightforwardly be adapted for such case.

Optimization of all the structures was performed by the genetic algorithm. In case of multi-steps QW structures, we vary the content of Al and the layer width in each of the step regions. It gives, in total, three free parameters for the one-step QW, five parameters for the two-step QW, and in general, $n_p = 2n_s + 1$ parameters, where n_s is the number of steps in the well. The Al mole fraction, x , in the step regions is limited to $x \in [0, 0.6]$. This still provides structures with acceptably low strain and direct energy bandgap in the barrier region. The lower boundary for the layer width is set to one monolayer (~ 0.3 nm) while the highest value is limited by the critical layer thickness caused by the strain.³⁵

In case of double QW structures, we vary only the layer widths of $\text{Al}_{0.6}\text{In}_{0.4}\text{As}$ and InAs , while the boundaries for the optimization parameters are chosen in the same manner as for the step QW structures. In this case, the total number of optimization parameters is $n_p = n_l$, where n_l is the number of layers in the structure. Optimization was also performed for the triple QW and QWs with higher number of layers.

In Fig. 1, the evolution of the susceptibility target function for the step QW is presented. The population (number of individual quantum wells being tested in each cycle for optimal value of $\chi_{zzz}^{(2)}$) is fixed to a typical value of 100, verified as suitable for problems of this type.^{18,36} For each generation, the value shown is selected as the highest among 100 members of the population in the optimization process. Maximum generations rule was used as the termination criterion, implying that GA stops when a specified number of generations have evolved (in our case 500 generations is sufficient). As the population evolves, its individuals become more and more similar, as evident from Fig. 1, and the optimization

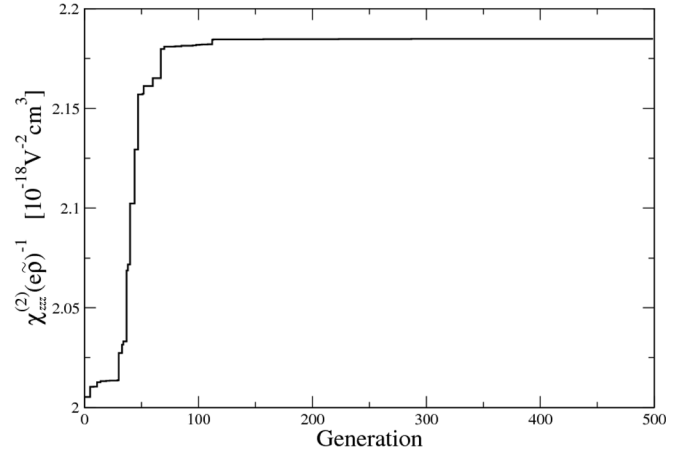


FIG. 1. The evolution of the scaled target function toward the optimal value. The vertical axis provides the maximum value of the susceptibility $\chi_{zzz}^{(2)}$ per mean density of the electron charge in the structure ($e\bar{\rho}$) in each cycle of the genetic algorithm. Each optimal value point refers to the best individual among the current population, and the quantity $e\bar{\rho}$ is subject to doping. The horizontal axis indicates the number of cycles (generations). The population size is set to 100 individuals, i.e., 100 QWs in each generation, covering the free parameters space. The maximum number of generations is used as a termination criterion and 500 generations prove sufficient for a successful optimization procedure.

process ends after completing 500 cycles, having selected an optimal individual.

The resulting one-step QW, that correspond to the maximal susceptibility $\chi_{zzz}^{(2)}/e\bar{\rho} = 2.185 \times 10^{-18} \text{ cm}^3 \text{ V}^{-2}$, is shown in Fig. 2. The layer widths are 2.23 nm and 3.5 nm, and the Al concentration in the step is 0.55. The energies amount to $E_1 = 0.39$ eV, $E_2 = 0.95$ eV, and $E_r = 1.51$ eV. It should be noted that in this structure, the widths of all the layers taken with arbitrary accuracy during the optimization. However, if we apply the technological constraint that the width of each layer must be an integer multiple of one monolayer, the target function reduces to $\chi_{zzz}^{(2)}/e\bar{\rho} = 0.892 \times 10^{-18} \text{ cm}^3 \text{ V}^{-2}$, which is 2.45 times smaller than in the previous case. This is still a satisfactory result, and with such modification, the layer widths become equal to 2.121 nm (7 monolayers) and 3.504 nm (12 monolayers), and Al concentration is 0.55. The energy spectra are: $E_1 = 0.41$ eV $E_2 = 0.96$ eV $E_r = 1.53$ eV.

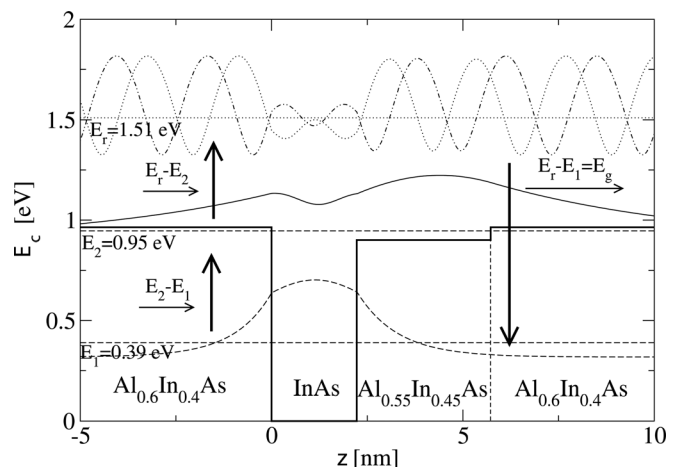


FIG. 2. The optimized step QW with respect to $\chi_{zzz}^{(2)}$.

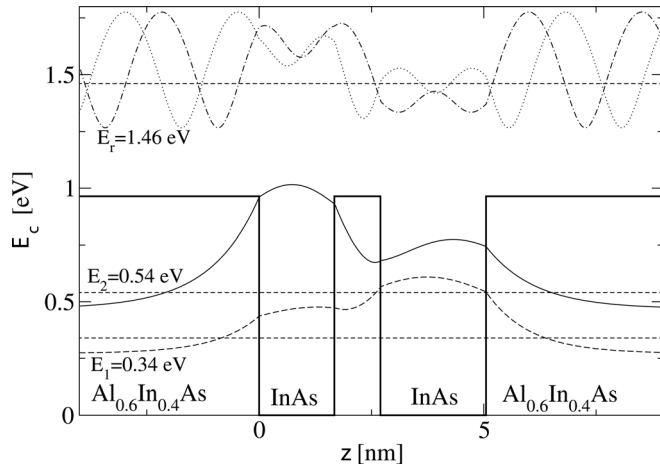


FIG. 3. The optimized double QW with respect to $\chi_{zzz}^{(2)}$.

An alternative way to model the up-converter is by optimizing multi-QW structures with only two different kinds of materials. In such structures, we can vary only the widths of the layers and the number of layers is always odd starting from 3. Optimization procedure based on GA leads to an optimal double well structure with $\chi_{zzz}^{(2)}/e\tilde{\rho} = 0.993 \times 10^{-18} \text{ cm}^3 \text{ V}^{-2}$, which is presented in Fig. 3. The layer widths are 1.689/1.022/2.341 nm, the Al concentration is 0.6, while the energies are at $E_2 = 0.34 \text{ eV}$, $E_1 = 0.54 \text{ eV}$, and $E_r = 1.46 \text{ eV}$. The maximal susceptibility $\chi_{zzz}^{(2)}$ of the optimized double well structure is 2.2 times lower than that of the step well. Again, after imposing technological constraints and rounding up the width of the layers to the integer multiple of one monolayer, the value of the target function reduces 1.15 times to $\chi_{zzz}^{(2)}/e\tilde{\rho} = 0.864 \times 10^{-18} \text{ cm}^3 \text{ V}^{-2}$. The layer widths are now: 1.515/1.164/2.121 nm, i.e., 5, 4, and 7 monolayers, respectively, with Al concentration of 0.6, and $E_1 = 0.38 \text{ eV}$, $E_2 = 0.57 \text{ eV}$, $E_r = 1.5 \text{ eV}$. In comparison to the step quantum well, the $\chi_{zzz}^{(2)}$ of the optimized double well with layers widths limited to the integer number of one monolayer has 2.55 times lower value. This is again an acceptable result, bearing in mind that in an arbitrarily chosen QW $\chi_{zzz}^{(2)}$ can be several orders of magnitude lower.

To check out if the structures with larger number of layers or steps can provide for the increased susceptibility, we have performed further optimizations of two-step, three-step as well as triple QW structures. We have observed that those more complex structures improve the susceptibility for only $\sim 5\%$ when compared to the one-step or double QW structures. Hence, it is probably not worth the technological effort to grow structures with increased number of layers due to negligible improvement of the desired effect. Thus for the multi-step wells structures, the optimal solution appears to be a one-step well. Furthermore, for the second type of structures, the optimal one is the simple double well with three layers.

We conclude that the optimized QW structure presented in Fig. 2 has the highest value of the target susceptibility function among all the layered structures considered here.

To obtain the overall efficiency improvement, it is necessary that the absolute value of the photon flux emitted

from the SC to the converter does not exceed the photon flux emitted from the converter and absorbed by SC. This implies that the SC chemical potential μ_{sc} should be smaller than the chemical potential of emitted light from the up-converter μ_c . Because the chemical potential of the radiation cannot exceed the lowest photon energy that forms the radiation, we have: $\mu_c < U_b - E_2$.⁸ For the optimized one-step QW, $\mu_c < 0.57 \text{ eV}$, and consequently, we must have $\mu_{sc} < 0.57 \text{ eV}$, if improvement in efficiency is expected.

Unfortunately the proposed QW structures are not deep enough to satisfy thermodynamical demands. If U_b was higher than the μ_{sc} , μ_c could have taken higher values and consequently, the efficiency improvement would be higher. For values of μ_c around 0.8 eV efficiency improvement is around 3%. Also, a higher value of μ_c gives the possibility for higher value of μ_{sc} which is optimal around 7.2 eV.

B. Analysis of the target function

To gain a better understanding of the requirements for the optimal structure, we proceed with the analysis of the target function (Eq. (18)). As presented in Fig. 2, $E_p \approx E_q \approx 0.56 \text{ eV}$, i.e., $\Delta E \approx 0$. From Eq. (19), it can be concluded that for a small values of ΔE , the integral function increases. However, ΔE determines only the first part of Eq. (19). Therefore, $\Lambda(E)$ and $\Theta(E)$ must also be examined. Those functions are given in Fig. 4 for the optimal quantum well structure from Fig. 2. In the limit $\Gamma_{c1} \rightarrow 0$, the value of $\Theta(E)$ (Eq. (21)) amounts to $\pi\delta(E - E_r)$. Thus, for the small values of Γ_{c1} , $\Theta(E)$ and consequently $D(E)$, have a peak at the energy E_r . This peak can be noticed in Fig. 4, but it is small when compared to the first peak of the sub-integral function $D(E)$. The first peak is usually determined by a peak of $\Lambda(E)$ function, which is always placed very close to the barrier top. This is somewhat expected because the continuous states are slow oscillating at the lower energies part of the continuum spectra. It rises very fast due to phase fitting and then slowly falls down to zero. However, there are cases when the peak at E_r is dominant. Such situation occurs when the pack of $\Lambda(E)$ has smaller values and while the same functions acquire generally higher

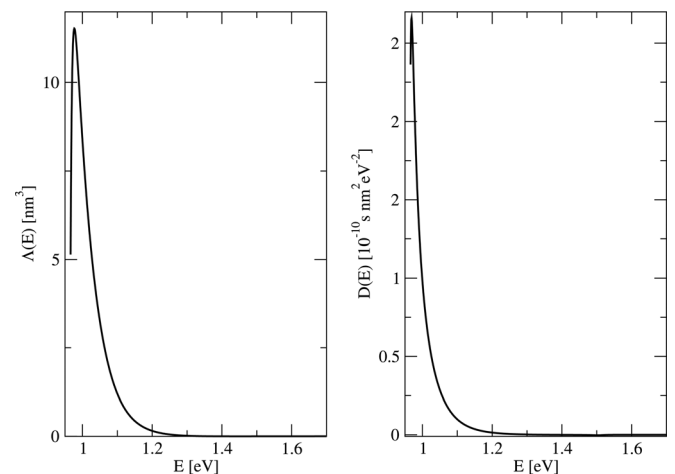


FIG. 4. Left energy function that explicitly involves bound to continuum-matrix elements for the optimized step quantum well from Fig. 2. Right: sub-integral function of the energy for the continuum states of the same QW.

values toward the infinity. Which peak is dominant should not be very important for the optimal value of Eq. (18). It turns out that for all the optimized QWs considered here, the first peak is always dominant. It suggests that $D(E)$ is not strongly dependent on the parameter Γ_{c1} which cannot be chosen with high accuracy anyway.

Ideally, for the proposed systems, both peaks should be at the same energy. This could be obtained for deeper QWs. The first peak is always very close to the top of the barrier as indicated in the preceding text. The position of the second peak is determined by the position of the first bound state. In the case of deeper QWs, it is expected that the first bound state is generally around the same position, and therefore E_r is closer to the top of the barrier. As a result, peaks would be multiplied and integral value would be higher.

IV. CONCLUSION

The optical up-converter for enhancing the silicon solar cells efficiency based on the InAs/AlInAs asymmetric step QW structures, taking into account critical layer thickness as constraint, was proposed and optimized. The optimization was done by using the genetic algorithm, which leads to the maximization of target function in the form of second order susceptibility of the QW, for the light frequencies that are suited for the desired photon conversion. The second order susceptibility was derived from the density matrix formalism, while the relevant electron states were calculated using 8-band $\mathbf{k}\cdot\mathbf{p}$ Hamiltonian.

Ideally, QW up-converter should have three bound states where desired nonlinear effect would be more efficient. Unfortunately among zinc-blende III-V materials such QW structure cannot be identified. Therefore, in future work one should seek a material combination that can provide a sufficiently deep well. Possible candidates are wurtzite III-N compounds, which require different modeling. However, the choice of continuum states as the “third state” has proven that the optimization may also be done automatically for nearby continuum states, which would physically improve the nonlinear effect.

ACKNOWLEDGMENTS

The authors wish to thank Ned Ekins-Daukes for useful discussions and suggestions. S.T. is grateful to STFC Energy Strategy Initiative for financial support while J.R. and V.M. acknowledge the support by the Ministry of Science (Republic of Serbia) project No. III 45010.

- ¹M. Green, *Prog. Photovoltaics* **9**, 123 (2001).
- ²A. Nozik, *Physica E* **14**, 115 (2002).
- ³R. R. King, *Nat. Photonics* **2**, 284 (2008).
- ⁴A. Luque and A. Martí, *Phys. Rev. Lett.* **78**, 5014 (1997).
- ⁵A. Luque, A. Martí, and A. Nozik, *MRS Bull.* **32**, 236 (2007).
- ⁶A. Luque and A. Martí, *Adv. Mater.* **22**, 160 (2010).
- ⁷S. Tomić, T. S. Jones, and N. M. Harrison, *Appl. Phys. Lett.* **93**, 263105 (2008).
- ⁸T. Trupke, M. Green, and P. Würfel, *J. Appl. Phys.* **92**, 1668 (2002).
- ⁹T. Trupke, M. Green, and P. Würfel, *J. Appl. Phys.* **92**, 4117 (2002).
- ¹⁰B. S. Richards and A. Shalav, *IEEE Trans. Electron Devices* **54**, 2679 (2007).
- ¹¹Y. Yi, L. Zhu, and Z. Shuai, *Macromol. Theory Simul.* **17**, 12 (2008).
- ¹²S. Adachi, in *Properties of Semiconductor Alloys-Group-IV, III-V, and II-VI Semiconductors*. Wiley Series for Materials for Electronic and Optoelectronic Application (Wiley, New York, 2008), pp. 133–196.
- ¹³I. Vurgaftman, J. R. Meyer, and L. R. Ram-Mohan, *J. Appl. Phys.* **89**, 5815 (2001).
- ¹⁴I. M. Safonov, I. A. Sukhoivanov, O. V. Shulika, A. A. Dyomin, S. O. Yakushev, M. V. Klymenko, S. I. Petrov, and V. V. Lysak, in *Proceedings of ICTON, We.C2.2 IEEE*, New York, USA, (2006), pp. 193–198.
- ¹⁵S. Kirkpatrick, C. D. Gelatt, and M. P. Vecchi, *Science* **220**, 671 (1983).
- ¹⁶G. Goldoni and F. Rossi, *Opt. Lett.* **25**, 1025 (2000).
- ¹⁷A. Franceschetti and A. Zunger, *Nature* **402**, 60 (1999).
- ¹⁸J. Radovanović, V. Milanović, Z. Ikonić, and D. Indjin, *J. Phys. D* **40**, 5066 (2007).
- ¹⁹P. William, T. Saul, V. William, and F. Brian, *Numerical Recipes in Fortran 90: The Art of Parallel Scientific Computing* (University of Cambridge Press, Cambridge, UK, 1996).
- ²⁰J. Radovanović, V. Milanović, Z. Ikonić, and D. Indjin, *Solid State Commun.* **110**, 339 (1999).
- ²¹J. Radovanović, V. Milanović, Z. Ikonić, and D. Indjin, *Phys. Rev. B* **59**, 5637 (1999).
- ²²J. Radovanović, V. Milanović, Z. Ikonić, and D. Indjin, *J. Appl. Phys.* **91**, 525 (2002).
- ²³J. Radovanović, V. Milanović, Z. Ikonić, and D. Indjin, *Phys. Rev. B* **69**, 115311 (2004).
- ²⁴D. E. Goldberg, *Genetic Algorithms in Search, Optimization and Machine Learning* (Addison-Wesley, Reading, MA, 1989).
- ²⁵S. Tomić, A. G. Sunderland, and I. J. Bush, *J. Mater. Chem.* **16**, 1963 (2006).
- ²⁶S. Tomić, M. Tadić, V. Milanović, and Z. Ikonić, *J. Appl. Phys.* **87**, 7965 (2000).
- ²⁷C. Sirtori, F. Capasso, I. Faist and S. Scandolo, *Phys. Rev. B* **50**, 8663 (1994).
- ²⁸R. V. Boyd, *Nonlinear Optics* (Academic-Elsevier Science, New York, 2003), pp. 129–176.
- ²⁹V. Milanović, Z. Ikonić, and D. Tjapkin, *Phys. Low-Dimens.* **7**, 65 (1995).
- ³⁰M. F. Pereira, Jr., R. Binder, and S. W. Koch, *Appl. Phys. Lett.* **64**, 279 (1994).
- ³¹M. F. Pereira, Jr. and K. Hennerberger, *Phys. Stat. Sol. B* **202**, 751 (1997).
- ³²M. F. Pereira, Jr. and K. Hennerberger, *Phys. Stat. Sol. B* **206**, 477 (1998).
- ³³H. Haug and S. W. Koch, *Quantum Theory of the Optical and Electronic Properties of Semiconductors* (World Scientific Publishing, Singapore, 2004).
- ³⁴M. F. Pereira, Jr., *Phys. Rev. B* **78**, 245305 (2008).
- ³⁵S. Tomić and E. P. O'Reilly, *IEEE Photonic Technol. Lett.* **15**, 6 (2003).
- ³⁶A. Daničić, J. Radovanović, V. Milanović, D. Indjin, and Z. Ikonić, *J. Phys. D* **43**, 045101 (2010).

Photonic crystals with bound states in continuum and their realization by an advanced digital grading method

This article has been downloaded from IOPscience. Please scroll down to see the full text article.

2009 J. Phys. A: Math. Theor. 42 415304

(<http://iopscience.iop.org/1751-8121/42/41/415304>)

View [the table of contents for this issue](#), or go to the [journal homepage](#) for more

Download details:

IP Address: 129.11.21.2

The article was downloaded on 03/07/2013 at 16:38

Please note that [terms and conditions apply](#).

Photonic crystals with bound states in continuum and their realization by an advanced digital grading method

N Prodanović, V Milanović and J Radovanović

Faculty of Electrical Engineering, University of Belgrade, Bulevar Kralja Aleksandra 73,
11120 Belgrade, Serbia

E-mail: radovanovic@etf.bg.ac.yu

Received 20 April 2009, in final form 26 August 2009

Published 29 September 2009

Online at stacks.iop.org/JPhysA/42/415304

Abstract

The Helmholtz equation can be reshaped into a form analogous to the Schrödinger equation with the term labeled ‘the optical potential’. By following this analogy, we conclude that there exist certain profiles of optical potentials which possess bound states of electric field in the continuous part of the spectrum. One of the methods for generating these specific optical potentials is the application of supersymmetric formalism which transforms a real (initial) potential into a family of complex potentials, which all have one bound state in the continuum. We present general steps of this procedure and illustrate its use through the example of flat initial optical potential. In this particular case, conditions are found for the existence of the bound field in continuum, as well as the expression for the field and the corresponding complex optical potential in an analytic form. In addition, the approximation of digital grading is applied to the generated complex supersymmetric optical potential and the ‘bound’ state is calculated. The complex nature and the sharp variations of the supersymmetric optical potential impose the development of an original and sophisticated method of digital grading.

PACS numbers: 11.30.Pb, 03.65.Ge, 42.25.Bs

1. Introduction

Von Neumann and Wigner [1] were the first to find that the Schrödinger equation may have regular solutions which represent bound states in the continuous part of the spectrum. They have modulated the wavefunction in order to make it normalizable, and then used the modulating function to extract the potential which supports such states. Herrick and Stillinger [2–4] have shown that bound states in continuum may exist in atoms and molecules, and also

pointed to the possibility of an electron in the electric field becoming localized by addition of a suitable potential. Starting from a separable form of the Hamiltonian, Robnik has also derived normalizable wavefunctions [5]. While the existence of normalizable eigensolutions for non-local potentials is rather well explored [6], a systematic approach for local potentials is still missing. Various techniques have been employed for the wavefunction modulation [7]. In [8], the authors give an experimental demonstration of resonant states in continuum which are fairly similar in nature to bound states in continuum.

The physical phenomenon of bound states in continuum appears only for particular potential profiles, either in the quantum mechanical or optical case. In addition to above techniques for generating these specific potentials which support discrete states in continuous part of the spectrum, supersymmetric quantum mechanics (SUSYQM) represents a very efficient method which has primarily been used in quantum mechanical problems, and less often in optical problems. However, applying SUSYQM to a potential that is real leads to bound states only on the half-line $x \in (0, \infty)$ [9–11], but not the full line. In order to remove this constraint and generate bound states on the full line, complex potentials are introduced [12, 13]. This, on the other hand, leads to a specific problem with the practical realization of these generated complex potentials.

There is, indeed, a close analogy between quantum mechanical and electromagnetic phenomena. In [14], the existence of bound states in radiation continuum is illustrated in the example of two parallel gratings and two arrays of thin parallel cylinders, while [15, 16] show that photonic crystals with defects may have localized states in the continuous part of the spectrum.

In this paper, we start from the modified form of the Helmholtz equation for the electric field, which is analogous to the Schrödinger equation (and so are their general solutions), in order to construct complex optical potentials isospectral with the selected initial one. Each of the complex optical potentials supports one and only one localized normalizable function of the electric field in the continuum part of the spectrum. We first give a brief description of the SUSY procedure, details of which can be found in [12, 13], applied to a quantum mechanical problem, and then implement it to the case of a flat optical potential. Finally, we present the somewhat non-standard digital grading approximation of the generated complex potential and numerical solution for the electrical field function corresponding to it, with satisfactory similarity to the original solution.

2. Theoretical considerations

Consider a material that is linear and non-homogeneous in the x -direction, described by the following equations:

$$\begin{aligned}\vec{D} &= \varepsilon(x)\varepsilon_0\vec{E} \\ \vec{B} &= \mu(x)\mu_0\vec{H}.\end{aligned}\tag{1}$$

In addition, two practical restrictions are imposed: (1) the EM waves are propagating along the z -direction and (2) only the TE modes are considered, i.e. $\vec{E} = E\vec{e}_y$.

The propagation of monochromatic waves with frequency ω_0 is governed by the scalar wave equation which for the case of the TE modes may be written for the y component of the electric field:

$$-\frac{\partial^2 E(x, z)}{\partial z^2} - \frac{\partial^2 E(x, z)}{\partial x^2} + \frac{1}{\mu} \frac{d\mu}{dx} \frac{\partial E(x, z)}{\partial x} - \frac{\varepsilon(x)\mu(x)}{c^2} \omega_0^2 E(x, z) = 0.\tag{2}$$

This equation is solved by separation of variables, i.e. by taking $E(x, z) = E(x)E(z)$ and subsequently inserting

$$E(x) = \sqrt{\mu(x)}u(x), \tag{3}$$

into the Helmholtz equation, which thus becomes

$$-\frac{d^2u(x)}{dx^2} + \left[-k_0^2\varepsilon(x)\mu(x) - \frac{1}{2\mu} \frac{d^2\mu(x)}{dx^2} + \frac{3}{4} \frac{1}{\mu^2(x)} \left(\frac{d\mu(x)}{dx} \right)^2 \right] u(x) = -\beta^2u(x). \tag{4}$$

where $k_0 = \omega_0/c$ and β is the propagation constant. Furthermore, it is convenient to introduce a new function called ‘the optical potential’, which is defined as

$$\Theta(x) = -k_0^2\varepsilon(x)\mu(x) - \frac{1}{2\mu} \frac{d^2\mu(x)}{dx^2} + \frac{3}{4} \frac{1}{\mu^2(x)} \left(\frac{d\mu(x)}{dx} \right)^2. \tag{5}$$

In this manner equation (4) becomes analogous to the Schrödinger equation $-\frac{\hbar^2}{2m} \frac{d^2\psi(x)}{dx^2} + U(x)\psi(x) = E\psi(x)$, and takes the form

$$-\frac{d^2u(x)}{dx^2} + \Theta(x)u(x) = \nu u(x) \tag{6}$$

where $\nu = -\beta^2$. It can easily be shown that the functions $\frac{1}{\mu(x)} \frac{dE(x)}{dx}$ and $E(x)$ are continuous if $\varepsilon(x)$ and $\mu(x)$ have only finite discontinuities. Hence, the quantities $\sqrt{\mu(x)}u(x)$ and $\frac{1}{\sqrt{\mu(x)}} \frac{du(x)}{dx} + \frac{u(x)}{2\mu^{3/2}(x)} \frac{d\mu}{dx}$ must also be continuous. The last equation may be rewritten in the operator form as

$$\widehat{N}u = \nu u \tag{7a}$$

$$\widehat{N} = -\frac{d^2}{dx^2} + \widehat{\Theta}. \tag{7b}$$

The operator \widehat{N} is a Hermitian operator and can be written as

$$\widehat{N} = \widehat{A}_2\widehat{A}_1 + \nu \tag{8}$$

where ν is an arbitrary eigenvalue of the operator \widehat{N} , and the operators \widehat{A}_1 and \widehat{A}_2 are defined as

$$\widehat{A}_1 = \frac{d}{dx} + \widehat{W} \tag{9a}$$

$$\widehat{A}_2 = -\frac{d}{dx} + \widehat{W}. \tag{9b}$$

Here the term \widehat{W} denotes the ‘optical superpotential’:

$$\widehat{W}(x) = -\frac{1}{\overline{u}_\nu(x)} \frac{d\overline{u}_\nu(x)}{dx}. \tag{10}$$

In this equation,

$$\overline{u}_\nu(x) = u_\nu(x) \left[1 + C \int_{(x)} \frac{dx}{u_\nu^2(x)} \right] \tag{11}$$

is a general solution of the starting eigenproblem for the eigenvalue ν . The presence of the constant C is an indication of degeneracy of any solution of (4). In standard methods of solving of equation (4) it is usually assumed that the fields are finite and square integrable so in some cases the values of C become fixed. In the SUSY procedure applied here, the

nature of (11) is not significant because it is just an intermediate result which will be used for construction of some other solution of another optical potential with desired properties. Thus, it is not necessary to impose any restrictions on the complex constant C at this stage. The central property that is required of the end solution is its square integrability and localization in space, in spite of the fact that the corresponding eigenvalue belongs to the continuous part of the spectrum. Hence, the appropriate limitations to the values of C will be enforced once the final electric field function is obtained.

By following the conventional SUSY procedure we next consider the operator

$$\widehat{N}_2 = \widehat{A}_1 \widehat{A}_2 + \nu = -\frac{d^2}{dx^2} + \widehat{\Theta}_2. \tag{12}$$

As the constant C is a complex number here, so is the potential $\widehat{\Theta}_2$, and the new operator is thus non-Hermitian. Yet, it is isospectral to the initial Hamiltonian, with the exception of ν which is not its eigenvalue. We continue in an analogous manner, by constructing the operator \widehat{N}_3 :

$$\widehat{N}_3 = \widehat{A}_2 \widehat{A}_1 + \nu = -\frac{d^2}{dx^2} + \widehat{\Theta}_3, \tag{13}$$

which is defined via the new optical superpotential:

$$\overline{W}(x) = -\frac{1}{\overline{u}_{v2}(x)} \frac{d\overline{u}_{v2}(x)}{dx}. \tag{14}$$

Here $\overline{u}_{v2}(x)$ represents a general eigenvector of the operator \widehat{N}_2 :

$$\overline{u}_{v2}(x) = \frac{1}{\overline{u}_v(x)} \left[\rho + \int_{(x)} \overline{u}_v^2(x) dx \right] \tag{15}$$

corresponding to the eigenvalue ν , where ρ is an arbitrary constant. The operators \widehat{A}_1 and \widehat{A}_2 have the same form as \widehat{A}_1 and \widehat{A}_2 , but with the new superpotential $\overline{W}(x)$ instead of $W(x)$. The optical potential $\widehat{\Theta}_3$ is given by

$$\widehat{\Theta}_{SS}(x) = \widehat{\Theta}_3(x) = \widehat{\Theta}(x) - 2\frac{d^2}{dx^2} [\ln(\rho + I(x))] \tag{16}$$

where

$$I(x) = \int_{(x)} \overline{u}_v^2(x) dx. \tag{17}$$

The eigenfunction of the operator \widehat{N}_3 for the eigenvalue ν is given by

$$u_{v3}(x) = C_{v3} \frac{\overline{u}_v(x)}{\rho + I(x)} \tag{18}$$

and for any other eigenvalue ν_n the corresponding expression reads

$$u_{3n} = C_{3n} \left((\nu_n - \nu) u_n(x) + \frac{\overline{u}_v(x) \left[\overline{u}_v(x) \frac{du_n(x)}{dx} - u_n \frac{d\overline{u}_v(x)}{dx} \right]}{\rho + I(x)} \right). \tag{19}$$

Equation (18) can actually be included in this last formula by considering the limit $\nu_n \rightarrow \nu$. The term $(\nu_n - \nu) u_n(x)$ would thus vanish, while the limit of the second term in parentheses can be calculated as (see the appendix for details)

$$\frac{\overline{u}_v(x) \left[\overline{u}_v(x) \frac{du_n(x)}{dx} - u_n \frac{d\overline{u}_v(x)}{dx} \right]}{\rho + I(x)} \rightarrow \frac{\overline{u}_v(x)}{\rho + I(x)}. \tag{20}$$

All the eigenfunctions within the discrete part of the spectrum of \widehat{N} are localized in space, in contrast to any of those belonging to the continuum part of the spectrum. The situation is somewhat different for the operator \widehat{N}_3 because it may have a localized normalizable eigenvector even for an eigenvalue from the continuum of \widehat{N} . This will be illustrated through specific examples. Clearly, the values which are not the eigenvalues of \widehat{N} are not the eigenvalues of \widehat{N}_3 , either [4].

In this work we consider the following conditions which may have practical relevance: the initial optical potentials are taken to be purely real and variable within a given interval (x_{\min}, x_{\max}) but flat (having a constant value C_1) outside of this interval. As a result, within the SUSY treatment we have

$$\overline{u}_v(x \rightarrow \pm\infty) \rightarrow C_2 \cos(kx) + \sin(kx), \tag{21a}$$

$$I(x \rightarrow \pm\infty) \rightarrow \frac{x}{2}[C_2^2 + 1], \tag{21b}$$

$$u_{v3}(x \rightarrow \pm\infty) = \frac{C_2 \cos(kx) + \sin(kx)}{\rho + \frac{x}{2}[C_2^2 + 1]}, \tag{21c}$$

$$\Theta_3(x \rightarrow \pm\infty) = C_1. \tag{21d}$$

The last expression indicates that the outer ('flat') segments of the final structure $\Theta_3(x)$ consist of the same material selected for the construction of the initial profile $\Theta(x)$. If the parameters C and ρ are chosen so that the function $\rho + I(x)$ has no zeros on the whole domain, then $u_{v3}(x)$ can be normalized. This will result in certain restrictions imposed on the values of C and ρ . On the other hand, all the other eigenfunctions from the continuous part of the spectrum are not localized (except in the limit $v_n \rightarrow v$), so the final supersymmetric optical potential supports only one bound state in continuum.

In the case of supersymmetric transformation via the (initially) bound state (which is not of interest here), if the parameters C and ρ are both real, the final field can be normalized only for $C = 0$. This is the standard SUSY procedure which results in a real optical potential $\Theta_3(x)$. By observing equation (21c) we deduce that, if the constant $C = C_r + iC_i$ is real ($C_i = 0$ and C_r nonzero), then for any value of ρ one can find a coordinate x at which the denominator $\rho + I(x)$ becomes equal to zero; hence the field function becomes non-normalizable. If C is truly complex and ρ is real, the requirement for the normalizability of the field will determine the acceptable values of these parameters, as will be exemplified below. We will limit our considerations to $\rho \in R$, without any loss of generality, as the case of complex ρ can be analyzed in an analogous manner.

It can also be noted (within our model where the initial potential is real) that the reflection and transmission coefficients remain the same after employing the SUSY formalism. This is due to the fact that all the states wavefunction corresponding to eigenvalues $v_n \neq v$ have the asymptotic form for $x \rightarrow \pm\infty$ which is the same as the form of the wavefunction of the initial potential (for $x \rightarrow \pm\infty$). The state corresponding to the eigenvalue v , as already demonstrated, has one discrete solution (bound state in continuum) and one non-integrable solution which diverges as $x \rightarrow \pm\infty$. Therefore, it makes no sense to discuss the transmission and reflection for the state with the eigenvalue v of the final potential. Finally, if the initial potential is real, the absorption is clearly equal to zero; consequently, the absorption in all the complex final potentials remains zero, which can be expressed by the following equation:

$$\int_{-\infty}^{\infty} \text{Im}(\Theta_{ss}(x))|u_v(x)|^2 dx = 0. \tag{22}$$

At the end of this section, some comments need to be made about the normalization of the function $E_y(x)$. Contrary to the analogous quantum-mechanical problem, in the optical

domain there is no unique solution. One approach to normalization of $E_y(x)$ is by using the time-averaged incident power $P_{\text{in}} = \frac{\gamma_0 \varepsilon_0 c^2 S}{2\omega} |E_0|^2$, where $E_{\text{in}} = E_0 e^{i\gamma_0 x}$, S is the cross-section surface and c is the speed of light in vacuum. If P_{in} is known in advance, assuming that it remains unchanged in the supersymmetric procedure, it is possible to determine E_0 and thus perform the normalization. This is achievable only for continuous states. In the case of discrete states (such as the bound state in continuum), the normalization may be carried out using the method described in [17, 18]. Although it is evident from the above discussion that the normalization of $E_y(x)$ is not unambiguous, it has no considerable importance to the problems considered in this paper.

2.1. Construction of the supersymmetric optical potential via a flat initial optical potential

We examine the case of an optically homogeneous medium characterized by the electric and magnetic permeability ε , and μ , respectively. The selection of the initial potential is made based on its simplicity—the flat potential is clearly the simplest possible choice. Thus, all the terms containing derivatives of $\mu(x)$ in equation (4) vanish, and the product $\varepsilon(x)\mu(x)$ is constant. Certainly, there are many other options for the initial potential, but these would lead to quite complex (if at all obtainable in an analytic form) expressions for $u(x)$, without adding noticeably to the quality of the example. The general solution of (4) is then given by

$$\bar{u}_k(x) = \sin(kx) + C \cos(kx) \tag{23}$$

where

$$k = \sqrt{k_0^2 \varepsilon \mu - \beta^2}. \tag{24}$$

Clearly, the spectrum of the flat potential is completely continuous for $\beta^2 < k_0^2 \varepsilon \mu$. The aim is to employ the SUSY approach to find the complex potential that accommodates a bound state at the given eigenvalue. The final function can be express as

$$u_{ss}(x) \cong \frac{C \cos(kx) + \sin(kx)}{\rho + \frac{x}{2} - \frac{\sin(2kx)}{4k} - \frac{C \cos^2(kx)}{k} + C^2 \left[\frac{x}{2} + \frac{\sin(2kx)}{4k} \right]} \tag{25a}$$

while the superymmetric electric field reads

$$E_{ss}(x) = \sqrt{\mu} u_{ss}(x). \tag{25b}$$

The corresponding supersymmetric optical potential is given by

$$\Theta_{ss}(x) = -k_0^2 \varepsilon \mu - 2 \frac{d^2}{dx^2} \left[\ln \left[\rho + \frac{x}{2} - \frac{\sin(2kx)}{4k} - \frac{C \cos^2(kx)}{k} + C^2 \left(\frac{x}{2} + \frac{\sin(2kx)}{4k} \right) \right] \right]. \tag{26}$$

It is evident that the fulfillment of the normalizability conditions for the electric field depends on the denominator of equation (25), which may be separated into real and imaginary parts as

$$\text{Re}(\rho + I(x)) = \rho + \frac{x}{2} - \frac{\sin(2kx)}{4k} - \frac{C_r \cos^2(kx)}{k} + (C_r^2 - C_i^2) \left[\frac{x}{2} + \frac{\sin(2kx)}{4k} \right] \tag{27a}$$

$$\text{Im}(\rho + I(x)) = -\frac{C_i \cos^2(kx)}{k} + 2C_i C_r \left[\frac{x}{2} + \frac{\sin(2kx)}{4k} \right]. \tag{27b}$$

If $C_i = 0$, then $\text{Im}(\rho + I(x)) = 0$ for every x , and $\text{Re}(\rho + I(x))$ has at least one singularity for any ρ . Further, if $C_i \neq 0$, the equation $0 = -\frac{\cos^2(kx_0)}{k} + 2C_r \left[\frac{x}{2} + \frac{\sin(2kx_0)}{4k} \right]$ can be solved

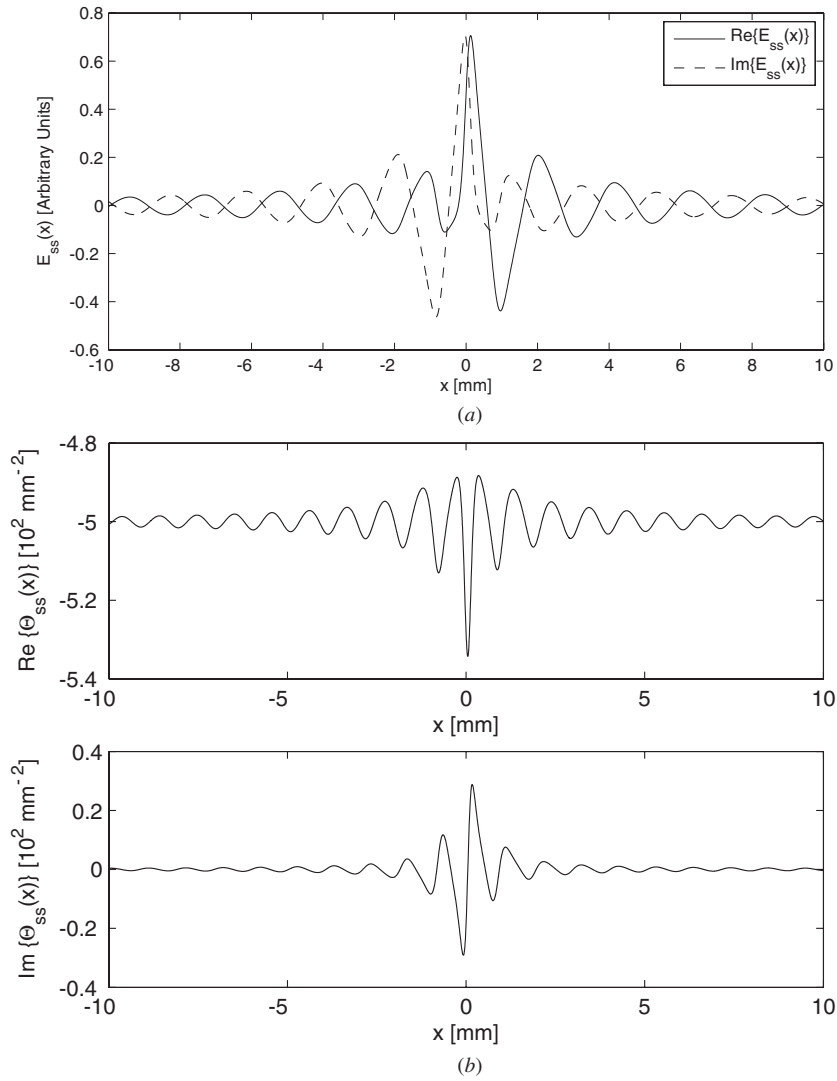


Figure 1. (a) An example of the supersymmetric localized electric field; (b) the corresponding supersymmetric optical potential, for $C = 3 + 3i$, $\rho = 6$ mm, $k = 3$ mm⁻¹, $k_0^2 \epsilon \mu = 500$ mm⁻².

for x_0 which cancels out the imaginary part of the system (27), leading to the condition $-\rho \neq \frac{x_0}{2} - \frac{\sin(2kx_0)}{4k} - \frac{C_r \cos^2(kx_0)}{k} + (C_r^2 - C_i^2) \left[\frac{x_0}{2} + \frac{\sin(2kx_0)}{4k} \right]$ for the real part.

The function $E_{ss}(x)$ will be square integrable if the coefficient in front of x in the system (27) is non-zero, which will be true if [12, 13]

$$(C_i C_r \neq 0 \quad \text{and/or} \quad C_r^2 - C_i^2 + 1 \neq 0).$$

After defining the acceptable values for C and ρ , it is straightforward to obtain the family of supersymmetric optical potentials $\Theta_{ss}(x, \rho, C)$ with corresponding bound supersymmetric electric fields $E_{ss}(x, \rho, C)$ at the eigenvalue ν . One particular case is shown in figure 1.

As expected from equation (21), the limit of the average value of the complex function $\Theta_{ss}(x \rightarrow \infty)$ amounts to $k_0^2 \epsilon \mu = 500$ mm⁻².

Numerical results indicate that for lower values of the parameter C and higher values of the parameter ρ , the optical potential and the electric field have lower surges, while these become stronger with the increase of C and the decrease of ρ .

The ultimate goal is to enable practical realization, i.e. to construct a photonic crystal with permittivity $\varepsilon_{SS}(x)$ and permeability $\mu_{SS}(x)$ which supports such a bound state in continuum. Obviously, the most direct approach is to devise a material with $\varepsilon_{SS}(x)$ and $\mu_{SS}(x)$ so that the resultant optical potential emulates the supersymmetric optical potential obtained previously. There are an infinite number of solutions to this problem. For example, one can apply the digital grading approximation directly to the supersymmetric optical potential and then compose very accurately the obtained digitally graded function.

Nevertheless, if we assume $\mu_{ss}(x) = \text{const} = \mu_{ss}$, then according to relation (5) we find

$$\varepsilon_{ss}(x) = -\frac{\lambda_0^2}{4\pi^2\mu_{ss}}\Theta_{ss}(x). \quad (28)$$

We have decided on a nonmagnetic material ($\mu_{SS} = 1$) for the following reason: in practical realizations, it is much easier to find a set of materials with prescribed real and imaginary parts of the dielectric permittivity, than a set of materials with both the required permittivity and magnetic permeability at given frequency. Regarding the theoretical design of a photonic crystal with the bound state in continuum, it is not significantly more complicated to consider materials with different magnetic permeabilities, as well.

The last expression describes the complex relative permittivity $\varepsilon_{ss}(x)$, which will be referred to as supersymmetric relative permittivity, proportional to the supersymmetric optical potential. Apparently, photonic crystal with the relative permittivity $\varepsilon(x) = \varepsilon_{ss}(x)$ and the relative permeability $\mu_{ss} = 1$ would provide $\Theta(x) = \Theta_{ss}$, together with the projected bound state in continuum. Thus, the problem is reduced to constructing the suitable photonic crystal with $\varepsilon(x) = \varepsilon_{ss}(x)$. The approximate solution to this problem may be found by realizing the calculated supersymmetric relative permittivity via digital grading. The advantage of this method is that it produces a complex relative permittivity function which is constant by parts and can therefore be realized by deposition of the layers of homogeneous materials.

2.2. The formalism of digital grading applied to complex supersymmetric relative permittivity

As explained in the previous section, it is necessary to process the complex supersymmetric relative permittivity by digital grading in order to obtain segments of the structure with homogeneous composition. The digital grading approximation of a complex function is somewhat uncommon; therefore, it will be explained here in detail, assuming that the reader is familiar with the standard digital grading approximation of real functions.

The first step is to define the segment of the structure that will undergo digital grading. Here we select a domain symmetric around zero, as both the real and the imaginary parts of the final function are almost symmetric or anti-symmetric. The area selected for digitalization should not be too wide, in order to ensure the quality of the approximation. The peripheral parts of the function are ‘flattened’ by taking the average values within particular areas. As shown in equation (21), the value of the initial (constant) relative permittivity may be taken as a satisfactory estimate of that flat outer part of the supersymmetric permittivity. Such averaging of the peripheral area implies that the corresponding field will not be exactly bound, but it will oscillate with sufficiently small amplitude and frequency.

The second step involves the application of digital grading formalism to both the real and the imaginary part of the relative permittivity in the previously defined central area, in the usual manner, as presented in [19–21], with a few modifications.

The conventional digital grading formalism approximates the potentials with only two values (e.g. the maximum and the minimum of the potential) across the whole domain, with the strict layout of those two values. In the procedure applied here, three values are used. This improves the accuracy of the approximation, but complicates the construction of the obtained structure by increasing the number of constituent materials. Supersymmetric relative permittivity is a strongly oscillating function around some average value that is almost equal to the value in bulk or outside of the digitally graded area, so grading with only two values gives poor results and cannot be utilized. Hence, an additional (medium) value is introduced as the average value of the function outside of the digitally graded area, namely as in the ‘flattened’ area. The higher and the lower value are defined as in [19–21], as the extrema of the function over the entire domain.

As described in [19–21], the complete domain is divided into intervals which are then individually approximated with two different value combinations: the medium and the high value or the medium and the low value. Those intervals will be from now on referred to as the common cells. Thus, the common cell represents a standard interval where the graded approximate function (both the real and the imaginary part) has only two values. The calculated average of $\varepsilon_{ss}(x)$ determines the pair of values which is selected for each common cell. In more detail, the medium and the high value are used to describe a particular cell if the average value of $\varepsilon_{ss}(x)$ within it is greater than the medium value, while the medium and the low value combination is used in the opposite case.

However, the smallest homogenous units intended for depositions are not the segments occupied by individual values in each common cell, but the subcells which will be introduced later.

The width filled with each value within a particular cell depends on the magnitude of the integral

$$S = \int_{\text{Cell}} |\varepsilon_{ss}(x) - \varepsilon_{\text{med}}| dx, \quad (29)$$

where ε_{med} represents one of the two values appearing in a particular cell used as a reference. In this work, by definition, it is always assumed that ε_{med} corresponds to the medium value as it is the only value present in each cell. The width of a non-medium value $w_{\text{high/low}}$, which is either high or low for a specific cell, is defined by the relation

$$w_{\text{high/low}} = \frac{S}{|\varepsilon_{\text{med}} - \varepsilon_{\text{high/low}}|}. \quad (30)$$

The width occupied by the medium value is thus

$$w_{\text{med}} = d - w_{\text{high/low}}, \quad (31)$$

where d represents the width of the cells.

Finally, in the third step previously obtained real and imaginary digitally graded functions are used to compose the complex digitally graded structure. The complex values are introduced as combinations of real and imaginary values. By combining three real and three imaginary values, nine different complex values are obtained. If the two-value digital grading approximation were used, then such combination would provide 2×2 complex values.

This procedure entails the division of each common cell into subcells so that exactly one complex value can be assigned to each subcell, as shown in figure 2.

The whole structure can thus be constructed in practice by the deposition of the layers of different materials corresponding to each subcell. This implies that each subcell consists of one specific layer of suitable material chosen from the set of nine different materials if three-value digital grading is considered, and from the set of four materials if conventional two-value

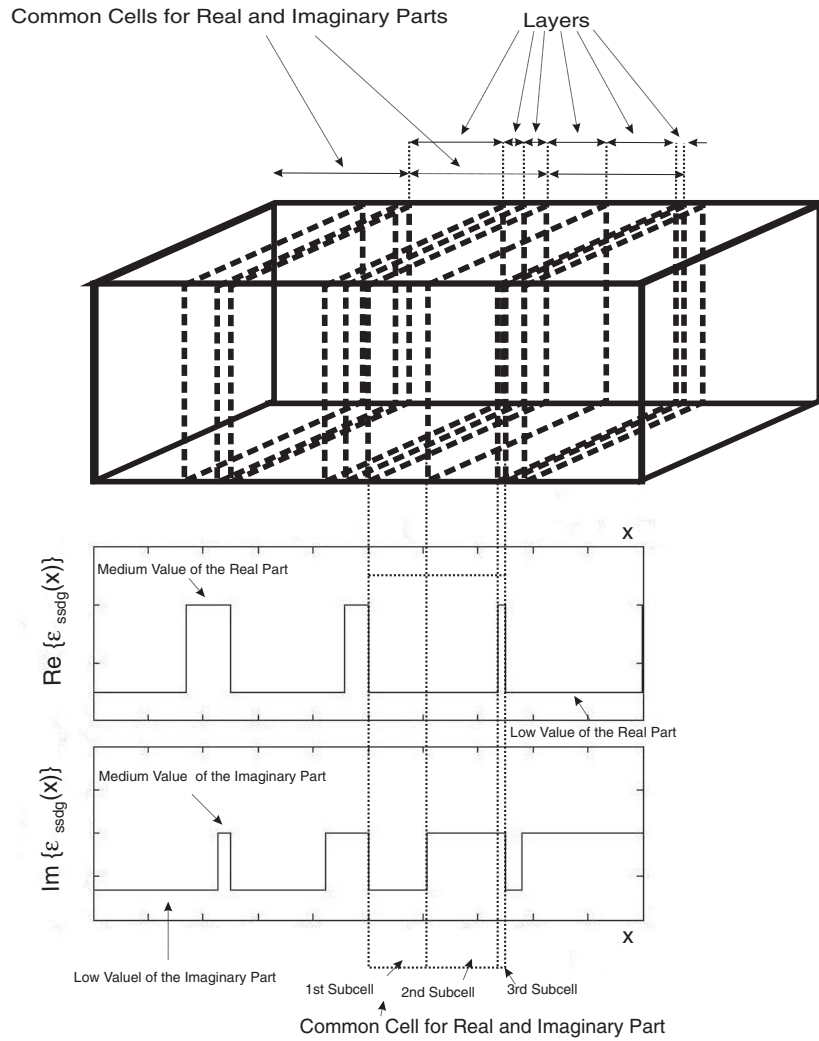


Figure 2. Realization of the complex digitally graded function ϵ_{ssdg} . Within one common cell interval of the digitally graded real and imaginary part, three subcells—subintervals are marked by dashed lines. The first subcell is characterized by a combination of the low value real part and low value imaginary part. The second subcell is characterized by a combination of the low value real part and medium value imaginary part. The third subcell is characterized by a combination of the medium value real part and the medium value imaginary part.

digital grading is in use. Because all the cells are shared by the real and the imaginary part of the function (i.e. they characterize both parts at the same time), and each of the cells comprises only two values of the real or the imaginary part, it is evident that the three subcells in each cell are sufficient to obtain the satisfactory complex digitally graded function.

3. Numerical examples and discussion

Depending on the selection of values of ν , ϵ , λ_0 and μ for the flat optical potential, various supersymmetric optical potentials are obtained. One can take for example $k = 3 \text{ mm}^{-1}$, $\epsilon = 5$, $\mu = 1$, $\lambda_0 \approx 630 \text{ }\mu\text{m}$, where $k_0 = \omega_0/c = 2\pi/\lambda_0$ denotes the wavenumber

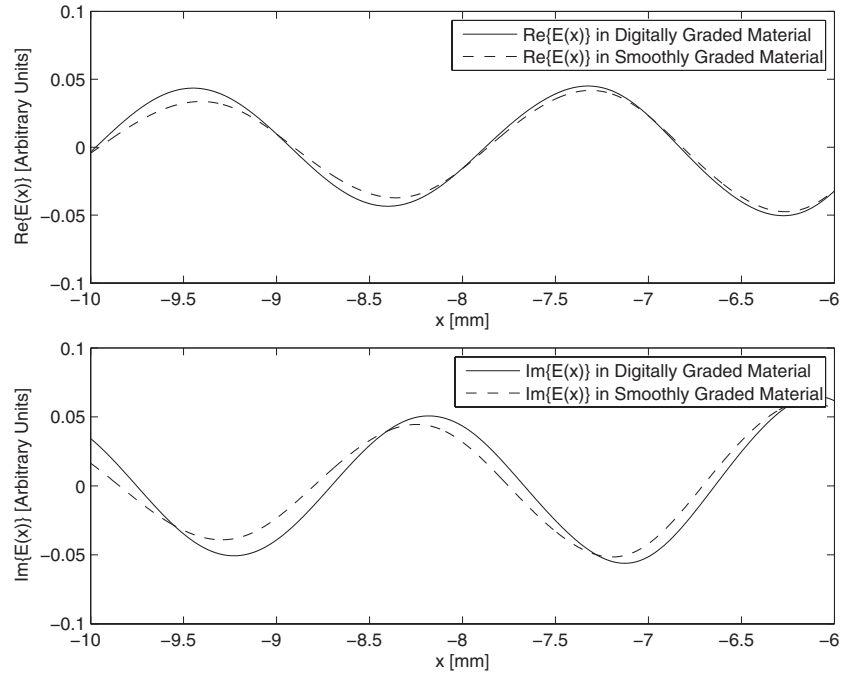


Figure 3. Comparison of the electric fields in the initial (smoothly graded) optical potential and the digitally graded optical potential. The initial conditions are the same within the central parts of the structures, so the differences between the approximated and the ‘accurate’ electric field functions are very small therein. The biggest difference appears at the end of the domain, which is here enlarged for clarity.

outside of the digitally graded area (in the homogenous part, which can be considered in the limit $x \rightarrow \pm\infty$), with the relative permittivity $\epsilon_{ss} = \epsilon$ and the permeability $\mu_{ss} = \mu$ as $\Theta_{ss}(x \rightarrow \pm\infty) = -k_0^2 \epsilon \mu$. The wavenumber k defines the eigenvalue ν for which the SUSY formalism is employed. The remaining parameters are then calculated as $k_0 = 10 \text{ mm}^{-1}$, $\nu = -\beta^2 = k^2 - k_0^2 \epsilon \mu = -491 \text{ mm}^{-2}$. In addition, C and ρ are defined so that the supersymmetric eigenfunction is normalizable:

$$C = 3 + 3i, \quad \rho = 9 \text{ mm}. \tag{32}$$

In the numerical example treated here, three real and three imaginary values of relative permittivity are calculated:

$$\begin{aligned} \text{Re}(\epsilon_{\text{high}}) &= 5.1513, & \text{Re}(\epsilon_{\text{med}}) &= 5, & \text{Re}(\epsilon_{\text{low}}) &= 4.9318, \\ \text{Im}(\epsilon_{\text{high}}) &= 0.15871, & \text{Im}(\epsilon_{\text{med}}) &= 0, & \text{Im}(\epsilon_{\text{low}}) &= -0.15565. \end{aligned} \tag{33}$$

The combinations of these values yield nine different homogenous materials whose relative permittivity values are

$$\begin{aligned} \epsilon_{\text{ssdg}1} &= 5.1513 + i \cdot 0.15871, & \epsilon_{\text{ssdg}2} &= 5.1513, & \epsilon_{\text{ssdg}3} &= 5.1513 - i \cdot 0.15565, \\ \epsilon_{\text{ssdg}4} &= 5 + i \cdot 0.15871, & \epsilon_{\text{ssdg}5} &= 5, & \epsilon_{\text{ssdg}6} &= 5 - i \cdot 0.15565, \\ \epsilon_{\text{ssdg}7} &= 4.9318 + i \cdot 0.15871, & \epsilon_{\text{ssdg}8} &= 4.9318, & \epsilon_{\text{ssdg}9} &= 4.9318 - i \cdot 0.15565. \end{aligned} \tag{34}$$

This combination of parameters is not exclusive. The set of parameters given by equation (34) is just an illustration, and this example is generated so that the values of the real and imaginary

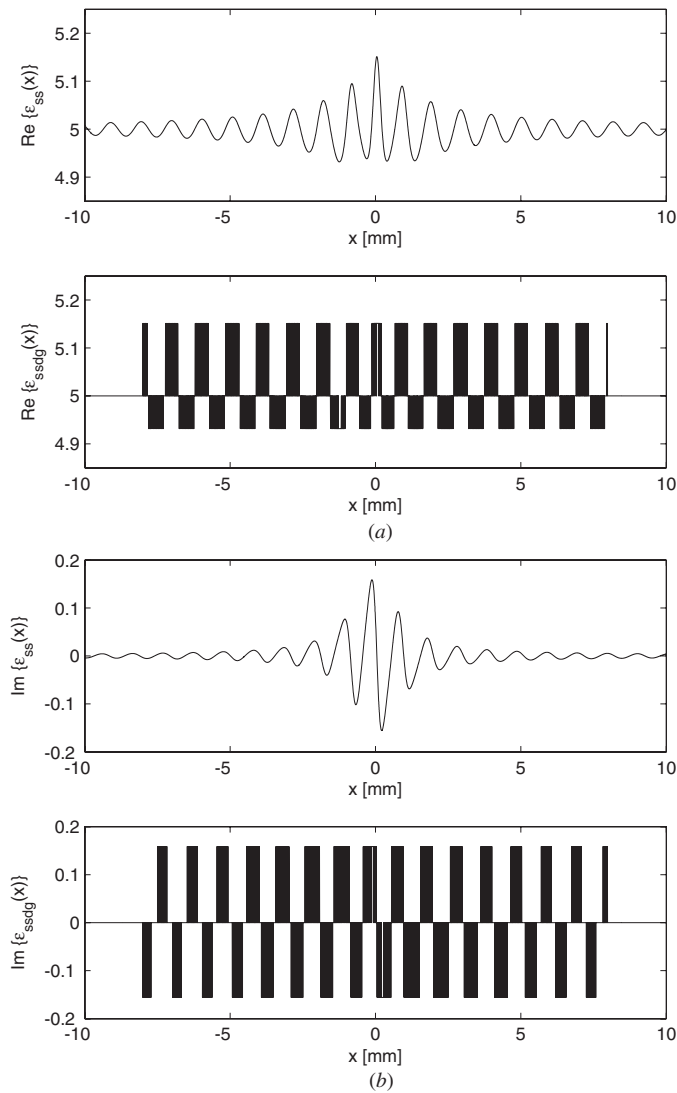


Figure 4. The results of the digital grading approximation with three values for both (a) the real and (b) the imaginary part.

parts of dielectric permittivities are within realizable limits, the condition that can obviously be satisfied by other parameter combinations. As already pointed out, some materials must have the negative imaginary part of the dielectric permittivity, which categorizes them as active dielectrics—materials which are nowadays extensively studied and their realization and characterization are well documented [22–24]. In our opinion, there is an additional approach to the realization of materials described by equation (34). It relies on (electrically or optically driven) quantum systems such as the quantum cascade laser, quantum amplifier or multiple quantum wells (dots), which exhibit different values of dielectric permittivity from the background permittivity [23, 24]. The sign and magnitude of the real and imaginary parts of this resultant permittivity depend on the design of the quantum structure in question (e.g.

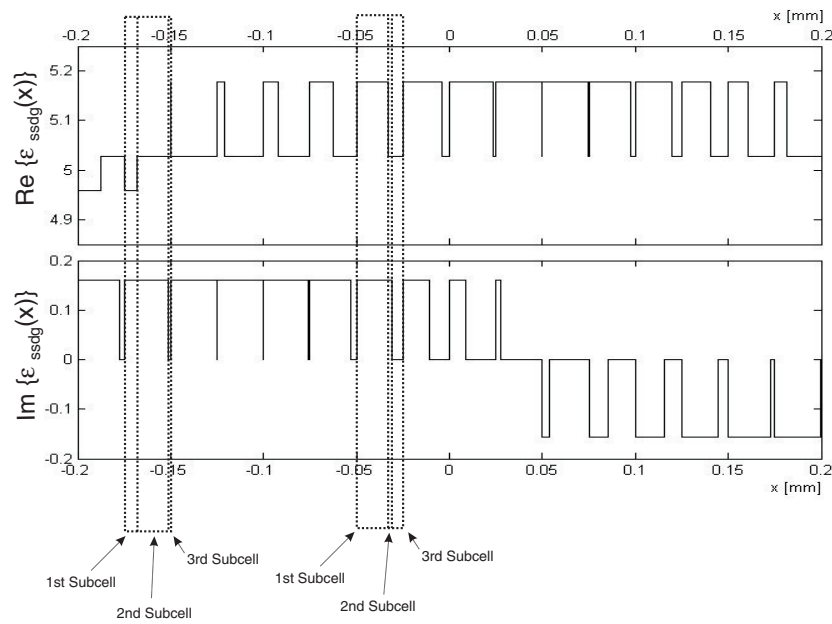


Figure 5. Magnified section of the digitally graded supersymmetric relative permittivity (the real and imaginary part). Two arbitrarily chosen common cells with their subcells are marked by the dotted lines: the first subcell of the left selected cell is described by the material with the high imaginary and low real value, namely $\epsilon_{ssdg7} = 4.9318 + i \cdot 0.15871$; the second subcell of the left selected cell is represented by the material with the high imaginary and medium real value, i.e. $\epsilon_{ssdg4} = 5 + i \cdot 0.15871$; the third subcell of the left selected cell corresponds to the material with $\epsilon_{ssdg5} = 5$. The first subcell of the right selected cell corresponds to the material with the high imaginary and high real value, that is $\epsilon_{ssdg1} = 5.1513 + i \cdot 0.15871$; the second subcell of the right selected cell is described by $\epsilon_{ssdg4} = 5 + i \cdot 0.15871$; and finally, the third subcell of the right selected cell is described by $\epsilon_{ssdg5} = 5$.

on widths of the well and the barrier layers, and on the material composition). For instance, materials with indices 3, 6 and 9 from equation (34) may be created so as to have predefined dielectric constants at a given frequency by varying e.g. only the layer widths, within relatively narrow limits, since these permittivities are quite similar. Apparently, the same applies for the group of materials with indices 1, 4, and 7, as well as 2, 5 and 8.

Depending on the wavelength of the electromagnetic mode, the dimension of the whole structure in the x -direction can be varied. The minimal thickness of an individual layer within the generated structure is limited by the numerical step used in calculations, which is here set to $d = 1 \mu\text{m}$. The obtained results are presented in figures 3–5.

4. Conclusion

The SUSY method was used to generate the complex optical potential with a localized electric field state in the continuum part of the spectrum. The bound state eigenvalue can be chosen arbitrarily from the continuous spectrum of an initial operator \widehat{N}_1 . The non-Hermitian operator \widehat{N}_3 , with a complex potential, is then generated as almost isospectral to \widehat{N}_1 , with an exception of one additional localized state with normalizable eigenfunction. The parameters of the complex optical potential have to be chosen so as to satisfy the condition of normalizability

for this electric field function. The obtained smooth structural profile is then processed by the digital grading technique, adapted to the case of a strongly oscillating complex function of the real argument. Thus, the values of the complex relative permittivity are approximated so that the structure may be realized by compiling the layers of homogeneous materials.

Acknowledgments

This work was supported by the Ministry of Science (Republic of Serbia), ev. no. 141006. VM and JR also acknowledge the financial support from NATO Collaborative Linkage Grant (reference CBP. EAP.CLG 983316).

Appendix

The new Wronskian function is defined as

$$W(x) = \overline{u}_v(x) \frac{du_n(x)}{dx} - u_n(x) \frac{d\overline{u}_v(x)}{dx} \quad (\text{A.1})$$

where $\overline{u}_v(x)$ consists of two linearly independent parts:

$$\overline{u}_v(x) = u_v(x) \left[1 + C \int_{(x)} \frac{dx}{u_v^2(x)} \right] = u_v(x) + C u_v(x) \int_{(x)} \frac{dx}{u_v^2(x)} = u_v(x) + C \tilde{u}_v(x). \quad (\text{A.2})$$

Thus we obtain

$$W(x) = u_v(x) \frac{du_n(x)}{dx} - u_n(x) \frac{du_v(x)}{dx} + C \left[\tilde{u}_v(x) \frac{du_n(x)}{dx} - u_n(x) \frac{d\tilde{u}_v(x)}{dx} \right]. \quad (\text{A.3})$$

Further, the function $u_n(x)$ also comprises two linearly independent parts:

$$u_n(x) = u_{n1}(x) + u_{n2}(x) \quad (\text{A.4})$$

where $\lim_{v_n \rightarrow v} u_{n1}(x) = u_v(x)$ and $\lim_{v_n \rightarrow v} u_{n2}(x) = \tilde{u}_v(x)$. Therefore, in the case of $v_n \rightarrow v$ and $u_n(x) = u_{n1}(x)$, equation (A.3) amounts to

$$W(x) = C \left[\tilde{u}_v(x) \frac{du_v(x)}{dx} - u_v(x) \frac{d\tilde{u}_v(x)}{dx} \right] = \text{const} \quad \text{q.e.d.} \quad (\text{A.5})$$

while in the other case $u_n(x) = u_{n2}(x)$, it reads

$$W(x) = u_v(x) \frac{d\tilde{u}_v(x)}{dx} - \tilde{u}_v(x) \frac{du_v(x)}{dx} = \text{const} \quad \text{q.e.d.} \quad (\text{A.6})$$

The conclusion is that all the eigenfunctions for $v_n \neq v$ which are double-degenerate become merged into one eigenfunction $\overline{u}_v(x)$ in the limit $v_n \rightarrow v$.

References

- [1] von Neumann J and Wigner E 1929 *Phys. Z.* **30** 465–70
- [2] Stillinger F H and Herrick D R 1975 *Phys. Rev. A* **11** 446–54
- [3] Stillinger F H 1976 *Physica B&C* **85** 270–6
- [4] Herrick D R 1976 *Physica B* **85** 44–50
- [5] Robnik M 1979 *J. Phys. A: Math. Gen.* **12** 1175–80
Robnik M 1986 *J. Phys. A: Math. Gen.* **19** 3845–8
- [6] Weber T A 1999 *J. Math. Phys.* **40** 140–9
- [7] Pursey D L and Weber T A 1995 *Phys. Rev. A* **52** 4255–8
- [8] Capasso F, Sirtori C, Faist J, Sivco D L, Chu S-N G and Cho A Y 1992 *Nature* **358** 565–7
- [9] Pappademos J, Sukhatme U and Pagnamenta A 1993 *Phys. Rev. A* **48** 3525–31
- [10] Sree Ranjani S, Panigrahi P K and Kapoor A K 2008 arXiv: cond-mat/0806.1799

- [11] Sree Ranjani S, Kapoor A K and Panigrahi P K 2008 *J. Phys. A: Math. Theor.* **41** 285302
- [12] Petrovic J S, Milanovic V and Ikonc Z 2002 *Phys. Lett. A* **300** 595–602
- [13] Milanovic V and Ikonc Z 2002 *Phys. Lett. A* **293** 29–35
- [14] Bulgakov E N and Sadreev A F 2008 *Phys. Rev. B* **78** 075105
- [15] Marinica D C, Borisov A G and Shabanov S V 2008 *Phys. Rev. Lett.* **100** 183902
- [16] Joannopoulos J D, Meade R D and Winn J N 1995 *Photonic Crystals: Molding the Flow of Light* (Princeton, NJ: Princeton University Press)
- [17] Bhat N A R and Sipe J E 2006 *Phys. Rev. A* **73** 063808
- [18] Bhat N A R and Sipe J E 2001 *Phys. Rev. E* **64** 056604
- [19] Vlaev S, Garcia-Moliner F and Velasco V R 1995 *Phys. Rev. B* **52** 13784–7
- [20] Lee J H, Li S S, Tidrow M Z, Liu W K and Bacher K 1999 *Appl. Phys. Lett.* **75** 3207–9
- [21] Mathine D L, Maracas G N, Gerber D S, Dropad R, Graham R J and McCartney M R 1994 *J. Appl. Phys.* **75** 4551–6
- [22] Shalaev V M 2007 *Nat. Photonics* **1** 41–8
- [23] Ginzburg P and Orenstein M 2008 *J. Appl. Phys.* **103** 083105
- [24] Ginzburg P and Orenstein M 2008 *J. Appl. Phys.* **104** 063513

Engineering and Advanced Digitalization of Photonic Structures with Bound Field in the Continuum

N. PRODANOVIĆ, V. MILANOVIĆ AND J. RADOVANOVIĆ*

School of Electrical Engineering, University of Belgrade, Belgrade, Serbia

We describe a method for generation of complex optical potentials which support a bound state of the electric field in continuous part of the spectrum. It is based on deep analogy between quantum mechanical and electromagnetic phenomena and relies on the application of supersymmetric quantum mechanics to generate a smoothly varying complex optical potential, together with the corresponding electric field function for the (single) localized state. However, the obtained potential profile is generally a strongly oscillating function which requires additional processing to make it suitable for practical realization. With this goal in mind, i.e. the construction of a realizable photonic crystal with complex permittivity which supports one bound state in continuum, we have developed an original scheme of digital grading. It approximates the values of the complex relative permittivity in such manner that the final structure may be realized by assembling layers of homogeneous materials.

PACS numbers: 11.30.Pb, 03.65.Ge, 42.25.Bs

1. Introduction

Supersymmetric quantum mechanics (SUSYQM) is a method that can be used to obtain operators which are almost isospectral, except that one of them has an additional bound state in continuum. Von Neumann and Wigner [1] found that the Schrödinger equation may have regular solutions which represent bound states in the continuum part of the spectrum, and Herick and Stillinger [2–4] have shown that bound states in continuum may exist in atoms and molecules. However, while the existence of normalizable eigensolutions for non-local potentials is rather well explored [5], a systematic approach for local potentials is still missing.

In addition, there is a close analogy between quantum mechanical and electromagnetic phenomena. In Ref. [6], the existence of bound states in radiation continuum is illustrated on the example of two parallel gratings and two arrays of thin parallel cylinders. Also, in Ref. [7], it is shown that photonic crystals with defects may have localized states in the continuum part of the spectrum.

In this paper, we start from the modified form of the Helmholtz equation for the electric field, which is analogous to the Schrödinger equation (and so are their general solutions), in order to construct complex permittivity functions which correspond to the selected initial one in terms of electric field spectrum. Each of the newly obtained complex permittivity profiles supports one and only one localized normalizable function of the electric field in the continuum part of the spectrum. We first give a short description of the SUSY procedure, details of which can be found in [8, 9] applied to a quantum mechanical problem, and then implement it to the

case of flat permittivity. Finally, we present somewhat non-standard digital grading approximation of generated complex permittivity and numerical solution for the electrical field function corresponding to it, with satisfactory similarity to the original solution.

2. Theoretical framework

Consider electromagnetic (EM) waves propagating along the x -direction, through a material which is linear and non-homogeneous in this direction and with constant magnetic permeability $\mu = 1$. Only linearly polarized TE modes are considered, i.e. $\mathbf{E} = E\mathbf{e}_y$ which are also monochromatic, i.e. $E(t) = Ee^{i\omega_0 t}$. Starting from the usual form of the Helmholtz equation and solving it by separation of variables $E(x, y, z, t) = E(x)E(y)E(z)e^{i\omega_0 t}$ one can show that $E(z) = Ee^{i\beta z}$, $E(y) = \text{const}$, and most importantly

$$\frac{d^2 E(x)}{dx^2} + k_0^2 \varepsilon(x) E(x) = \beta^2 E(x), \quad (1)$$

where $k_0 = \omega_0/c$.

Equation (1) is analogous to the Schrödinger equation $-\frac{\hbar^2}{2m} \frac{d^2 \psi(x)}{dx^2} + U(x)\psi(x) = E\psi(x)$. As described in Ref. [9], the idea is to construct isospectral operator $-\frac{d^2}{dx^2} - k_0^2 \varepsilon_{ss}(x, \rho, C)$, with complex constants ρ and C , by using standard SUSY procedure. The derived formula, as given in [9], reads

$$\varepsilon_{ss}(x) = \varepsilon(x) + \frac{2}{k_0^2} \frac{d^2}{dx^2} \left[\ln \left(\rho + \int_{(x)} E_{\beta}^2(x) \left[1 + C \int_{(x)} \frac{dx}{E_{\beta}^2(x)} \right]^2 dx \right) \right], \quad (2)$$

where $E_{\beta}(x)$ is the eigenstate corresponding to a chosen eigenvalue β^2 . Thus, the permittivity given by expression (2) is isospectral to $\varepsilon(x)$, and the additional (so-called

* corresponding author; e-mail: radovanovic@etf.bg.ac.rs

supersymmetric) eigenstate for a chosen eigenvalue, which was used for the SUSY procedure [9], is given by

$$E_{\beta_{\text{ss}}}(x) = C_{\beta_{\text{ss}}} \frac{E_{\beta}(x) \left[1 + C \int_{(x)} \frac{dx}{E_{\beta}^2(x)} \right]}{\rho + \int_{(x)} E_{\beta}^2(x) \left[1 + C \int_{(x)} \frac{dx}{E_{\beta}^2(x)} \right]^2 dx}. \quad (3)$$

It can be proven that if the initial eigenvalue β^2 corresponds to the continuous part of the spectrum, then its supersymmetric eigenstate is strictly a bound state in continuum, provided that the appropriate choice of parameters ρ and C is made [10].

First, we need to choose an initial permittivity with continuous spectra for generating a new (required) one with bound state in continuum. The simplest approach is to choose a “flat” initial permittivity ε . The general solution of (1) is then given by $E_k(x) = \sin(kx) + C \cos(kx)$ where $k = \sqrt{k_0^2 \varepsilon - \beta^2}$. Clearly, the spectrum of the flat permittivity is completely continuous for $\beta^2 < k_0^2 \varepsilon$. The aim is to employ the SUSY transform to find a complex permittivity that accommodates a bound state at the selected eigenvalue. The final electric field function can be expressed as

$$E_{\text{ss}}(x) \sim \frac{C \cos(kx) + \sin(kx)}{\rho + \frac{x}{2} - \frac{\sin(2kx)}{4k} - \frac{C \cos^2(kx)}{k} + C^2 \left[\frac{x}{2} + \frac{\sin(2kx)}{4k} \right]}, \quad (4)$$

while the corresponding supersymmetric permittivity is given by

$$\varepsilon_{\text{ss}}(x) = \varepsilon(x) + \frac{2}{k_0^2} \frac{d^2}{dx^2} \left[\ln \left(\rho + \frac{x}{2} - \frac{\sin(2kx)}{4k} - \frac{C \cos^2(kx)}{k} + C^2 \left(\frac{x}{2} + \frac{\sin(2kx)}{4k} \right) \right) \right]. \quad (5)$$

The discussion on selecting the appropriate values of parameters ρ and C is given in Ref. [9], and in the following numerical example one such choice is illustrated.

The ultimate goal is to enable practical realization, i.e. to construct a photonic crystal with permittivity $\varepsilon(x)$, given by expression (5), which supports the bound state in continuum. This can be accomplished by applying the digital grading approximation directly to the supersymmetric permittivity and then composing very accurately the obtained digitally graded function.

3. Digital grading of the complex relative permittivity

The digital grading approximation of a complex function is uncommon, therefore it will be explained here in detail, assuming that the reader is familiar with the standard digital grading approximation of real profiles.

The *first step* is to define the segment of the structure that will undergo digital grading. Here we select a domain symmetric around zero, as both the real and the imaginary part of the final function are almost symmetric

or antisymmetric. The peripheral parts of the function are “flattened” by taking the average values within particular areas. It can be shown that the value of the initial (constant) relative permittivity may be taken as a satisfactory estimate of that flat outer part of the supersymmetric permittivity. Such averaging of the peripheral area implies that the corresponding field will not be exactly bound, but it will oscillate with sufficiently small amplitude and frequency.

The *second step* involves the application of digital grading formalism to both the real and the imaginary part of relative permittivity in previously defined central area, in the usual manner, as presented in [11], with a few modifications.

In the procedure applied here, three levels (values) are used to approximate the final function, instead of only two values as in Ref. [11]. This improves the accuracy of the approximation, but complicates the construction of the obtained structure by increasing the number of constituent materials. Supersymmetric relative permittivity is a strongly oscillating function around some average value that is almost equal to the value in bulk or outside of the digitally graded area, so grading with only two levels gives poor results and cannot be utilized. Hence, an additional (medium level) is introduced as the average value of the function outside of the digitally graded area, namely as in the “flattened” area. The higher and the lower level are defined as in [11], as the extrema of the function over the entire domain.

As described in [11], the complete domain is divided into intervals which are then individually approximated with two different level combinations: the medium and the high level or the medium and the low level as shown in Fig. 1. Those intervals will be from now on referred to as “common cells”. Thus, the common cell represent a standard interval where the graded approximate function (both, the real and the imaginary part) has only two values or levels. The average value of $\varepsilon_{\text{ss}}(x)$ determines the pair of levels which is selected for each common cell. In more detail, the medium and the high level are used to describe a particular cell if the average value of $\varepsilon_{\text{ss}}(x)$ within it is greater than the medium level, while the medium and the low level combination is used in the opposite case.

However, the smallest homogeneous units intended for deposition are not the segments occupied by individual levels in each common cell, but the subcells which will be introduced later.

The width of each level within a particular cell depends on the value of the integral $S = \int_{\text{Cell}} |\varepsilon_{\text{ss}}(x) - \varepsilon_{\text{med}}| dx$ where ε_{med} is the value of one of the two levels appearing in a particular cell used as reference. In this work, by definition, it is always assumed that ε_{med} is the value corresponding to the medium level as it is the only level present in each cell. The width of a non medium level $w_{\text{high/low}}$, which is either high or low for a specific cell, is defined by the next relation $w_{\text{high/low}} = \frac{S}{|\varepsilon_{\text{med}} - \varepsilon_{\text{high/low}}|}$. The width of the medium level is then

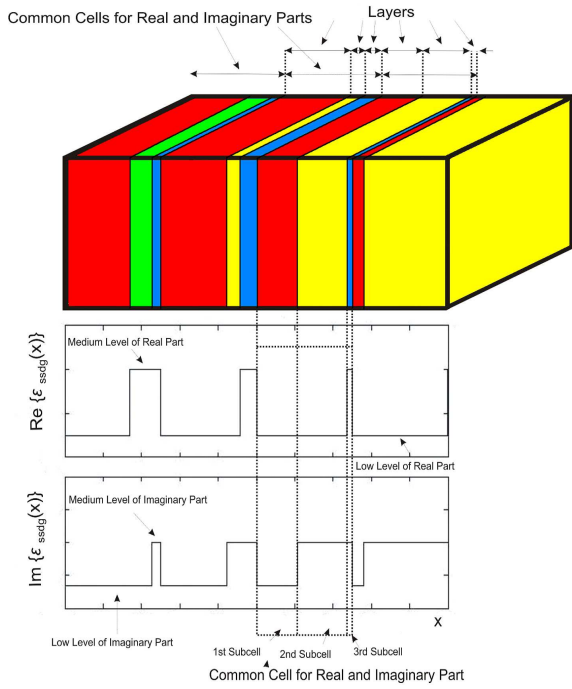


Fig. 1. Realization of the complex digitally graded function $\varepsilon_{\text{ssdg}}$. Within one common cell interval of digitally graded real and imaginary part, three subcells-subintervals are marked by dashed lines. 1st subcell (red) is characterized by a combination of low level real part and low level imaginary part. 2nd subcell (yellow) is characterized by a combination of low level real part and medium level imaginary part. 3rd subcell (blue) is characterized by a combination of medium level real part and medium level imaginary part.

$w_{\text{med}} = d - w_{\text{high/low}}$, where d represents the width of the cells.

Finally, in the third step previously obtained real and imaginary digitally graded functions are used to compose the complex digitally graded structure. The complex levels are introduced as combinations of real and imaginary levels. By combining three real and three imaginary levels, nine different complex levels are obtained. If two-level digital grading approximation was used then such combining would provide 2×2 complex levels.

This procedure entails the division of each common cell into subcells so that exactly one complex level can be assigned to each subcell, as shown in Fig. 1. The whole structure can thus be constructed in practice by deposition of layers of different materials corresponding to each subcell. This implies that each subcell consists of one specific layer of suitable material chosen from the set of nine different materials if three-level digital grading is considered, or from the set of four materials if conventional two-level digital grading is in use.

4. Numerical examples and discussion

Depending on the selection of values of β , ε and λ_0 for the flat optical potential, various supersymmetric optical

potentials are obtained. One can take for example: $k = 3 \text{ mm}^{-1}$, $\varepsilon = 5$, $\lambda_0 = 630 \text{ } \mu\text{m}$, where $k_0 = \omega_0/c = 2\pi/\lambda_0$ denotes the wave number outside of the digitally graded area (in the homogenous part, which can be considered in the limit $x \rightarrow \pm\infty$), with relative permittivity $\varepsilon_{\text{ss}} = \varepsilon$ as $\Theta_{\text{ss}}(x \rightarrow \pm\infty) = -k_0^2\varepsilon$. The wave number k defines the eigenvalue β for which the SUSY formalism is employed. The remaining parameters are then calculated as: $k_0 = 10 \text{ mm}^{-1}$, $\beta^2 = k_0^2\varepsilon - k^2 = 491 \text{ mm}^{-2}$. In addition, C and ρ are defined so that the supersymmetric eigenfunction is normalizable: $C = 3 + 3i$, $\rho = 9 \text{ mm}$. In the numerical example treated here, three real and three imaginary levels of relative permittivity are calculated:

$$\text{Re}(\varepsilon_{\text{high}}) = 5.1513, \quad \text{Im}(\varepsilon_{\text{high}}) = 0.15871,$$

$$\text{Re}(\varepsilon_{\text{med}}) = 5, \quad \text{Im}(\varepsilon_{\text{med}}) = 0,$$

$$\text{Re}(\varepsilon_{\text{low}}) = 4.9318, \quad \text{Im}(\varepsilon_{\text{low}}) = -0.15565. \quad (6)$$

The combinations of these levels yield nine different homogeneous materials whose relative permittivity values are

$$\varepsilon_{\text{ssdg}1} = 5.1513 + i*0.15871, \quad \varepsilon_{\text{ssdg}2} = 5.1513,$$

$$\varepsilon_{\text{ssdg}3} = 5.1513 - i*0.15565, \quad \varepsilon_{\text{ssdg}4} = 5 + i*0.15871,$$

$$\varepsilon_{\text{ssdg}5} = 5, \quad \varepsilon_{\text{ssdg}6} = 5 - i*0.15565,$$

$$\varepsilon_{\text{ssdg}7} = 4.9318 + i*0.15871, \quad \varepsilon_{\text{ssdg}8} = 4.9318,$$

$$\varepsilon_{\text{ssdg}9} = 4.9318 - i*0.15565. \quad (7)$$

This combination of parameters is not exclusive. The set of parameters given by Eq. (7) is just an illustration, and this example is generated so that the values of real and imaginary parts of dielectric permittivities are within realizable limits, the condition that can obviously be satisfied by other parameters combinations. As already pointed out, some materials must have negative imaginary part of the dielectric permittivity, which categorizes them as active dielectrics [12, 13]. In our opinion, there is an additional approach to realization of materials described by Eq. (7). It relies on (electrically or optically driven) quantum systems such as quantum cascade laser, quantum amplifier or multiple quantum wells (dots), which exhibit different values of dielectric permittivity from the background permittivity [12, 13]. The sign and magnitude of real and imaginary part of this resultant permittivity depend on the design of the quantum structure in question (e.g. on widths of the well and the barrier layers, and on the material composition). For instance, materials with indices 3, 6 and 9 from Eq. (7) may be created so to have predefined dielectric constants at a given frequency by varying e.g. only the layer widths, within relatively narrow limits, since these permittivities are quite similar. Apparently, the same applies for group of materials with indices 1, 4, and 7, as well as 2, 5 and 8.

Depending on the wavelength of the electromagnetic mode, the dimension of the whole structure in the x -direction can be varied. The minimal thickness of an

individual layer within the generated structure is limited by the numerical step used in calculations, which is here set to $d = 1\mu\text{m}$. The obtained electric field in the digitally graded structure is compared in Fig. 2 with the field of the smoothly graded structure, corresponding to the same eigenvalue. Evidently, the differences are quite small which confirms the validity of the applied approximation.

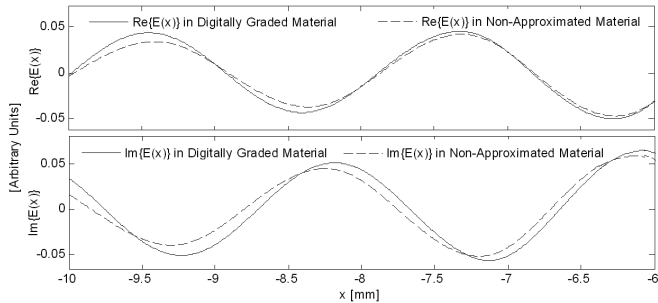


Fig. 2. Comparison of the electric fields for the initial (smoothly graded) permittivity and its digitally graded equivalent. The initial conditions are the same within the central parts of the structures, so the differences between the approximated and the “accurate” electric field functions are very small therein. The biggest difference appears at the end of the domain, which is here enlarged for improved readability.

Undoubtedly, the nature of the problem is such that it is very difficult to perform an accurate realization of the obtained results, because domain of the profile is conceptually infinite. In addition, the flattening of the peripheral areas of the potential converts the truly bound state into an oscillating one, as already pointed out. Nevertheless, the described procedure allows us to construct a digitalized structure which is experimentally realizable, and provides a satisfactory approximation to the theoretical prediction.

5. Conclusion

The SUSY method was used to generate complex optical potential with a localized electric field state in the

continuum part of the spectrum. The obtained smooth structural profile is then processed by the digital grading technique, adapted to the case of strongly oscillating complex function of the real argument so that the structure may be realized by compiling the layers of homogeneous materials.

Acknowledgments

This work was supported by the Ministry of Science (Republic of Serbia), ev. no. 141006. V. M and J. R. also acknowledge the financial support from NATO Collaborative Linkage Grant (reference CBP.EAP.CLG 983316).

References

- [1] J. von Neumann, E. Wigner, *Phys. Z.* **30**, 465 (1929).
- [2] F.H. Stillinger, D.R. Herrick, *Phys. Rev. A* **11**, 446 (1975).
- [3] F.H. Stillinger, *Physica B* **85**, 270 (1977).
- [4] D.R. Herrick, *Physica B* **85**, 44 (1977).
- [5] T.A. Weber, *J. Math. Phys.* **40**, 140 (1999).
- [6] E.N. Bulgakov, A.F. Sadreev, *Phys. Rev. B* **78**, 075105 (2008).
- [7] D.C. Marinica, A.G. Borisov, S.V. Shabanov, *Phys. Rev. Lett.* **100**, 183902 (2008).
- [8] J. Pappademos, U. Sukhatme, A. Pagnamenta, *Phys. Rev. A* **48**, 352535 (1993).
- [9] J.S. Petrović, V. Milanović, Z. Ikonić, *Phys. Lett. A* **300**, 595 (2002).
- [10] N. Prodanović, V. Milanović, J. Radovanović, *J. Phys. A, Math. Theor* **42**, 415304 (2009).
- [11] S. Vlaev, F. Garcia-Moliner, V.R. Velasco, *Phys. Rev. B* **52**, 13784 (1995).
- [12] P. Ginzburg, M. Orenstein, *J. Appl. Phys.* **103**, 083105 (2008).
- [13] P. Ginzburg, M. Orenstein, *J. Appl. Phys.* **104**, 063513 (2008).

Research Student Administration

University of Leeds
Leeds LS2 9JT

T +44 (0) 113 243 1751 (Switchboard)
F +44 (0) 113 343 3941 (Research Student Admin)
W www.leeds.ac.uk/rsa
T (Direct Line) +44 (0) 113 343 6534



UNIVERSITY OF LEEDS

21 September 2012

TO WHOM IT MAY CONCERN

This is to certify that

Nikola Prodanovic

Date of Birth 28/07/1986

is registered as a full-time student of this University for the period 01/10/2012 to 30/09/2013 whilst undertaking postgraduate research and study in the School of Electronic and Electrical Engineering leading to the degree of Doctor of Philosophy.

The candidate commenced studies on 01/10/2010 and is expected to complete them by no earlier than 30/09/2013 and is required to complete them by no later than 30/09/2014.



Leanne Carr
Student Records Officer
Research Student Administration

RSA/Student Records/B1

200508779



УНИВЕРЗИТЕТ У БЕОГРАДУ
Електротехнички факултет



ДОДАТАК ДИПЛОМИ
диплома број 17604

1. Информације које идентификују имаоца квалификације

- | | |
|--|--|
| 1.1 Презиме: Продановић | 1.6 Држава рођења: Република Словенија |
| 1.2 Име: Никола | 1.7 Идентификациони број (ЈМБГ): 2807986500101 |
| 1.3 Име једног од родитеља: Ненад | 1.8 Шифра (Број индекса): 2005/0158 |
| 1.4 Датум рођења (дд.мм.ггг.): 28.07.1986. | 1.9 На овај факултет је први пут уписан школске 2005/06, на прву годину студија. |
| 1.5 Место рођења: Постојна | |

2. Информације које идентификују квалификацију

- 2.1 Стечени стручни назив квалификације: **Дипломирани инжењер електротехнике**
- 2.2 Главне области студирања за квалификацију: **Техничко-технолошке науке**
- 2.3 Назив установе која даје квалификацију: **Универзитет у Београду**
- 2.4 Врста установе која даје квалификацију: **Универзитет**
- 2.5 Оснивач установе која даје квалификацију: **Република Србија**
- 2.6 Назив институције која управља студијама: **Електротехнички факултет Универзитета у Београду**
- 2.7 Оснивач установе која управља студијама: **Република Србија**
- 2.8 Језик студија: **српски**

3. Информације о нивоу квалификације

- 3.1 Ниво квалификације: **Основне студије - VII/1 степен**
- 3.2 Званична дужина трајања студија: **4 године**
- 3.3 **Услови уписа:** У 1. годину основних студија на Електротехничком факултету може се уписати лице које има средње образовање у четворогодишњем трајању
 - А: Упис после завршене средње школе**
 - 3.3.1а Назив и седиште школе: **Гимназија "Вељко Петровић", Сомбор**
Завршио 2005. године.
 - Б: Прелаз са другог факултета**
 - 3.3.1б Назив и седиште факултета: --
 - В: Упис после завршене више школе**
 - 3.3.1в Назив и седиште више школе: --
Завршио -- године.

4. Информације о садржајима и постигнутим резултатима

4.1 Начин студирања: редован студент (са пуним обимом ангажовања)

4.2 Захтев програма: Студент који положи све испите утврђене наставним планом основних студија и одбрани дипломски рад стиче високо образовање и стручни назив дипломирани инжењер електротехнике одговарајућег усмерења (Одсек за физичку електронику - смер Наноелектроника, оптоелектроника и ласерска техника).

4.3 Појединости оствареног програма:

Шифра	Предмет	Укупан фонд часова			Испит Оцена	Наставник
		Предавања	Вежбе	Остало		
001EJ1	Енглески језик 1	30	0	0	10 (десет)	Ђурић Милош
001EJ2	Енглески језик 2	30	0	0	9 (девет)	Ђурић Милош
001LOE	Лабораторијске вежбе из Основа електротехнике	0	0	30	10 (десет)	Ђорђевић Антоније
001LF	Лабораторијске вежбе из Физике	0	0	30	10 (десет)	Осмокровић Предраг
001MM1	Математика 1	45	45	0	9 (девет)	Радосављевић Зоран
001MM2	Математика 2	45	45	0	10 (десет)	Радосављевић Зоран
001OE1	Основи електротехнике 1	45	45	0	10 (десет)	Илић Милан
001OE2	Основи електротехнике 2	45	45	0	10 (десет)	Илић Милан
001P1	Програмирање 1	45	30	0	10 (десет)	Томашевић Мило
001P2	Програмирање 2	45	30	0	10 (десет)	Протић Јелица
001PE1	Практикум из Основа електротехнике 1	15	15	0	10 (десет)	Илић Милан
001UM	Увод у менаџмент	30	0	0	10 (десет)	Надић Дарко
001F1	Физика 1	45	30	0	10 (десет)	Тодић Милан
001F2	Физика 2	45	30	0	10 (десет)	Џвезић Јован
0F2E	Електромагнетика	45	30	0	10 (десет)	Петровић Владимир
0F2EJ3	Енглески језик 3	30	0	0	10 (десет)	Ђурић Милош
0F2EJ4	Енглески језик 4	30	0	0	10 (десет)	Ђурић Милош
0F2EE	Елементи електронике	45	30	15	10 (десет)	Дрндаревић Вујо
0F2KM	Квантна механика	45	30	0	10 (десет)	Радовановић Јелена
0F2M3	Математика 3	45	30	0	10 (десет)	Џакић Ненад
0F2M4	Математика 4	30	30	15	10 (десет)	Џакић Ненад
0F2OFE	Основи физичке електронике	45	30	0	10 (десет)	Гвоздић Дејан
0F2PRM	Практикум из рачунарских алата у математици	15	0	22,5	10 (десет)	Лациновић Иван
0F2PSA	Практикум из софтверских алата	15	0	22,5	10 (десет)	Граовац Стевица
0F2SIS	Сигнали и системи	45	15	15	10 (десет)	Ђуровић Жељко
0F2TEK	Теорија електричних кола	45	30	0	9 (девет)	Резин Бранимир
0F3DOS	Дигитална обрада сигнала	45	15	15	10 (десет)	Станковић Срђан
0F3EEU	Елементи електронских уређаја	45	15	15	10 (десет)	Милановић Витомир
0F3KE	Квантна електроника	45	30	0	10 (десет)	Гвоздић Дејан
0F3MIN	Микроелектроника и наноелектроника	45	30	0	10 (десет)	Тодић Милан
0F3O	Оптоелектроника	45	15	15	10 (десет)	Матавуљ Петар
0F3POT	Простирање оптичких таласа	45	30	0	10 (десет)	Џвезић Јован
0F3SF	Статистичка физика	45	30	0	10 (десет)	Радуновић Јован
0F3FEЧ	Физичка електроника чврстог тела	45	30	0	10 (десет)	Радовановић Јелена
0F3FTM	Физичко техничка мерења	45	0	30	8 (осам)	Станковић Драган
0F4OT	Оптичке телекомуникације	45	30	0	9 (девет)	Гвоздић Дејан
0T3M5	Математика 5	45	15	15	10 (десет)	Џакић Ненад
0F3EIM	Економија и менаџмент	45	30	0	10 (десет)	Поповић - Аврић Снежана
0F4AMP	Анализа и моделовање полупроводничких направа	45	30	0	10 (десет)	Милановић Витомир
0F4LT	Ласерска техника	45	30	0	10 (десет)	Елазар Јован
0F4MES	Микроелектромеханички системи	45	30	0	10 (десет)	Тодић Милан
0F4NIN	Нанотехнологије и нанокомпоненте	45	30	0	10 (десет)	Тодић Милан
0F4PKN	Полупроводничке квантне наноструктуре	45	30	0	10 (десет)	Радовановић Јелена
0F4FEG	Физичка електроника гасова и плазме	45	30	0	10 (десет)	Џвезић Јован
0F4PKN	Дипломски испит (Дипломски рад)	225	225	-	10 (десет)	Милановић Витомир

Тема дипломског рада:

Фотонски кристали са везаним стањем у континуалном делу спектра

Наставник - ментор дипломског рада: Милановић Витомир, редовни професор

Датум одбране дипломског рада (дд.мм.ггг.): 13.10.2009.

4.4 Шема оцењивања:

Оцена	Значење оцене	Процент од укупног броја поена (%)
10	Изузетан	91 - 100
9	Одличан	81 - 90
8	Врло добар	71 - 80
7	Добар	61 - 70
6	Довољан	51 - 60
5	Недовољан	≤ 50

4.5 Укупна оцена квалификације:

Просечна оцена: изузетан: 9.87 (девет, 87/100)

5. Информације о функцији квалификације

5.1 Приступ даљем студирању:

Ималац дипломе има право да настави даље образовање и усавршавање у складу са Законом о високом образовању

6. Додатне информације

6.1а Положио следеће предмете који нису предвиђени наставним планом и програмом за стицање дипломе: --

6.1б Похађао следеће ваннаставне курсеве: --

6.1в Постигао успех на студентским такмичењима у знању: --

6.1г Остале активности: --

6.2 Извори о додатним информацијама:

О институцији: www.etf.bg.ac.yu; www.mps.sr.gov.yu

О програму: Студентски одсек ЕТФ-а

7. Оверавање додатка:

7.1 Овај додатак дипломи односи се на следећа оригинална документа:

Диплома факултета број: 17604 издата дана (дд.мм.ггг.): 13.10.2009.



Декан:

Проф. др Миодраг Поповић

3a Ректор:

Проф. др Бранко Ковачевић



Универзитет у Београду
Електротехнички факултет
Број: 225
Датум: 02.07.2010.

На основу члана 161 Закона о општем управном поступку и службене евиденције,
Универзитет у Београду - Електротехнички факултет, издаје

У В Е Р Е Њ Е

Никола (Ненад) Продановић, ЈМБГ: 2807986500101, рођен 28.07.1986. године, Постојна, Република Словенија, уписан школеке 2009/10. године на 1. годину студија, дана 01.07.2010. године завршио је дипломске академске студије другог степена на студијском програму **Дипломске академске студије Електротехника и рачунарство - модул Наноелектроника, оптоелектроника и ласерска техника** обима 60.0 (шездесет) бодова ЕСПБ са просечном оценом 10.00 (десет и 00/100).

На основу тога издаје му се ово уверење о стеченом високом образовању и академском називу **дипломирани инжењер електротехнике и рачунарства - мастер.**

Уверење важи до издавања дипломе. Диплома ће носити број овог уверења.



Декан

Проф. др Миодраг Поповић